

Alma Mater Studiorum – Università di Bologna

DOTTORATO DI RICERCA IN

CHIMICA

Ciclo XXIX

Settore Concorsuale di afferenza: 03/C2- CHIMICA INDUSTRIALE

Settore Scientifico disciplinare: CHIM/04 - CHIMICA INDUSTRIALE

**MINERALIZATION OF RECOMBINANT COLLAGEN-
LIKE PEPTIDE TO DESIGN HYBRID SCAFFOLDS FOR
BONE TISSUE REGENERATION**

Presentata da: Gloria Belén Ramírez Rodríguez

Coordinatore Dottorato

Prof. Aldo Roda

Relatore

Dtt.ssa Maria Letizia Focarete

Co-relatori

Dtt.ssa Monica Sandri

Esame finale anno 2017

Abstract

The use of synthetic peptides has aroused great interest in tissue engineering field since they present several advantages respect to natural source materials such as controlled and reproduced chemical composition and molecular weight, the lack of the risk of associated infectious diseases, the large-scale production and the possibility to be engineered with special functionalities.

The present PhD Thesis is focused on the fabrication of hybrid scaffolds for bone regeneration through biomimetic mineralization of recombinant collagen peptide (RCP) in the presence of magnesium ions (Mg) to closely mimic ionic composition of bone apatite. RCP sequence is based on human collagen type I and it is enriched in arginine-glycine-aspartic acid sequence (RGD), that act as a cell binding site.

The biomimetic mineralization of RCP has been adapted from the bioinspired mineralization protocol of natural collagen carried out previously by our group to obtain bone-like scaffolds. Inspired in nanocomposite nature of bone, hybrid scaffolds were developed through a bottom-up approach that started on the evaluation of apatite mineralization mechanism in the presence of RCP and Mg and how they could affect the nanocrystal morphology and composition. Then, three-dimensional prototype scaffolds were developed through freeze-drying of mineralized RCP slurry to determine optimum mineral content. Furthermore, the interfacial properties of mineralized matrices in the presence and in the absence of Mg were evaluated at nanoscopic level.

Since RCP is water-soluble, different crosslinking methodologies (chemical and physical) were evaluated to ensure the stability under physiological conditions as well as the resistance to enzymatic degradation. The crosslinking of mineralized scaffolds by chemical treatment was carried out with a natural crosslinking agent (genipin) by three different techniques, named as: pre-crosslinking, post-crosslinking and scaffold crosslinking. On the other hand, the physical crosslinking was performed by dehydrothermal treatment (DHT). The most suitable crosslinking methodology was selected and applied for the following tests.

The subsequent step was the design of 3D isotropic scaffolds with suitable pore size, porosity and permeability by modifying several freezing parameters during freeze-drying of mineralized RCP slurry. Finally, *in vitro* tests were carried out to evaluate how biochemical signals (i.e., surface chemistry and ion release from scaffold) together with biophysical signals (e.g., surface nano-topography) conferred *via* biomimetic

mineralization can persuade and guide Mesenchymal Stem Cells (MSCs) interaction and fate. The *in vitro* study in static conditions revealed a more prominent cell migration into inner areas of scaffolds and higher gene expression of osteogenic markers for scaffolds mineralized in the presence of magnesium (MgAp/RCP).

Considering the shortcomings of static cell culture triggering to low extent of cell migration towards interior of the scaffold, designed hybrid scaffolds were tested by seeding and culturing human mesenchymal stem cells on 3D scaffolds in a bioreactor of direct perfusion (developed by Fraunhofer Institute). The results indicated the improvement of cell seeding under dynamic conditions, the enhancement of osteogenic differentiation for cells cultured on MgAp/RCP scaffolds and the role of mechanical stimulus on accelerating the osteogenic differentiation of mesenchymal stem cells.

Acknowledgments

I would like to thank to Dr. Monica Sandri, Dr. Simone Sprio and Dr. Anna Tampieri for the opportunity to carry out my PhD in the context of the EU project BIO-INSPIRE. I would like to thank all my colleagues from Laboratory of Bioceramics and Bio-hybrid Composites of the Institute for Science and Technology for Ceramics (ISTEC-CNR, It). In special, I thank to Dr. Monica Montesi and Dr. Silvia Panseri for teaching me and supporting my activity in the biological lab and Dr. Michele Iafisco for the collaboration in other projects.

I would also like to thank all the BIO-INSPIRE partners, for their collaboration and the high quality work carried out during the project. It was a great experience to work with researchers from different fields and learn about other areas of tissue engineering. A special thanks to Dr. Suzan Van Dongen and Dr. Bas Kluijtmans from Fujifilm Europe BV and Prof. Heike Walles of University Hospital of Wurzburg for accepting me in their research groups during the stage abroad during my PhD.

I would like to express my gratitude to my academic advisor, Dr. Maria Letizia Focarete, for her encouragement and suggestion during my doctoral research period.

I would like to thank to the person that introduce me in the exciting and passionate world of research, especially in the area of biomineralization. JMDL has been my academic advisor and at the same time a good friend. Thank you for all your help and for having a “coffee” with me when I really needed it, giving me your advices and telling me everything will be all right.

I want to thank to Tatiana Patricio, colleague, flatmate and a great friend that support me in the bad moments. She has been as a sister during these 3 years abroad. I could not be here without your help. I also want to thank all the friends from Faenza for the sharing their time with me and for all the good memories.

I would like to thank to my parents, my brothers and sisters and my partner to support me in all my decisions. They always believe on me and make me feel strong enough to face all the problems and difficulties in order to reach my goals. They are always there, when I need them.

Table of contents

Abstract.....	i
Acknowledgments	iii
Table of Contents.....	iv
List of Figures.....	viii
List of Tables.....	xiv
List of Abbreviations	xvi

Chapter 1: Introduction

1.1. Introduction: Overview of Bone tissue Engineering	1
1.2. Bone.....	2
1.2.1. Bone composition and biology	2
1.2.2. Hierarchical structure of bone.....	4
1.2.3. Bone biomineralization.....	6
1.3. Biomaterials for bone regeneration inspired in bone biomineralization	8
1.3.1. Design of biomaterials via biomimetic mineralization of natural polymers	8
1.3.2. Biomimetic mineralization of synthetic polymers.....	9
1.3.3. Self-assembly and mineralization of synthetic peptides.....	10
1.3.4. Bio-inspired mineralization of recombinant proteins	10
1.4. Scaffold design for bone tissue engineering.....	12
1.4.1. Biocompatibility	12
1.4.2. Degradation kinetics	12
1.4.3. Mechanical Properties.....	13
1.4.4. Surfaces Properties	13
1.4.5. Scaffold microstructure.....	15
1.4.6. Osteoconduction, osteoinduction and osseointegration.....	16
References	17

Chapter 2: General Experimental Methods and Techniques

2.1 Materials	25
2.2. Characterization techniques.....	25
2.3. Characterization of the physic-chemical properties of designed scaffolds	27
2.3.1. Porosity	27
2.3.2. Permeability	27
2.3.3. Interfacial properties: Surface roughness and wettability.....	28
2.3.4. Swelling capacity	28
2.3.4. Determination of extent of crosslinking	29
2.3.5. <i>In vitro</i> scaffold degradation.....	29
2.3.6. Enzymatic degradation	29
2.4. <i>In vitro</i> tests	30
2.4.1. Cell viability and proliferation.....	30
2.4.2. Cell morphology	30
2.4.3. Cell migration	31
2.4.4. Quantitative real-time polymerase chain reaction (qPCR).....	31
2.4.5. Western Blot Analysis	32
2.4.6. Immunofluorescence.....	32
2.5. Statistical analysis.....	33
References	33

Chapter 3: Understanding the biomineralization of a recombinant collagen peptide in the presence of magnesium

3.1. Introduction	34
3.2. Methods	36
3.3. Results	36
3.4. Discussion.....	43
3.5. Conclusions	45
References	45

Chapter 4: Biomimetic mineralization of recombinant collagen peptide to obtain hybrid matrices for bone regeneration

4.1. Introduction	49
4.2. Methods	51
4.2.1. Prototype 3D scaffolds: Evaluation of maximum mineral content	51
4.2.2. Preparation of hybrid matrices of different compositions	51
4.3. Results	52
4.3.1. Amount of mineral suitable to obtain homogeneous 3D structure	52
4.3.2. How modification of mineralization protocol can alter macroscopic properties?	54
4.4. Discussion.....	57
4.5. Conclusions	58
References	59

Chapter 5: Investigations of different crosslinking approaches of recombinant collagen peptide

5.1. Introduction	62
5.2. Methods	64
5.3. Results	66
5.3.1. Chemical crosslinking with genipin	66
5.3.2. Investigations of different crosslinking of RCP hybrid scaffolds	69
5.4. Discussion.....	71
5.5. Conclusions	73
References	74

Chapter 6: Fabrication of 3D isotropic hybrid scaffolds through freeze-drying and evaluation of their osteoinductive potential

6.1. Introduction	77
6.2. Methods	79
6.2.1. Scaffold preparation.....	79
6.2.2. Cell culture and cell seeding on scaffolds	80
6.3. Results	81

6.3.1. Design of 3D structures through freeze-drying	81
6.3.2. Characterization of physic-chemical properties of designed 3D scaffold	83
6.3.3. Evaluation of <i>in vitro</i> degradation of the scaffolds.....	86
6.3.4. Cell viability and proliferation.....	87
6.3.5. Cell-material interaction	88
6.3.6. Effect of the scaffold on the osteogenic marker expression	90
6.4. Discussion.....	92
6.5. Conclusions	95
References	95

Chapter 7: Expansion and differentiation of hMSCs on nanocomposite scaffolds in a bioreactor with mechanical stimulus

7.1. Introduction	99
7.2. Methods	101
7.2.1. Flow perfusion bioreactor	101
7.2.2. Cell seeding of 3D scaffolds	102
7.2.3. Dynamic cell culture	103
7.2.4. Mechanical stimulus	103
7.3. Results	103
7.3.1. Cell seeding of 3D scaffolds	103
7.3.2. Dynamic cell culture of hybrid recombinant collagen peptide scaffolds	105
7.3.3. Dynamic cell culture of hMSCs in MgAp/RCP with mechanical stimulus ...	106
7.4. Discussion.....	108
7.5. Conclusions	110
References	110

Chapter 8: Concluding Remarks 115 |

Work in progress based on this thesis	118
Peer-reviewed publication based on this thesis	118
Conference presentation based on this thesis	118
Other peer-reviewed publication	118

List of figures

Chapter 1: Introduction

- Figure 1.** Scheme of bone remodelling. Reprinted from Weilbaecher *et al.*, Copyright (2011) with permission of Nature Publishing Group: Nature Reviews Cancer4
- Figure 2.** Hierarchical structure of bone. Reprinted from Wang *et al.*, Copyright (2016) with permission of Elsevier: Biomaterials.....5
- Figure 3.** Nanoscopic view of mineralized collagen fibres structure and organization. (a) Model of mineralized collagen fibrils showing the arrays of the plate-like Ap nanocrystals in the gap zones formed in staggered arranged collagen fibrils. (b) Face-on and edge-on projections of the crystals in the mineralized fibril. (c) TEM micrograph of an array of the mineralized fibrils from human dentin. Reprinted from Beniash *et al.*, Copyright (2011) with permission from John Wiley & Sons, Inc: Wiley Interdisciplinary Reviews, Nanomedicine and Nanobiotechnology7
- Figure 4.** Schematic illustration of the mechanism by which nanomaterial surface properties may be superior to conventional materials for bone regeneration. Reprinted from Zhang *et al.*, Copyright (2009) with permission of Elsevier: Nanotoday.....14

Chapter 2: General Experimental Methods and Techniques

- Figure 1.** Recombinant collagen peptide (RCP) amino acid sequence is based on human collagen type I25

Chapter 3: Crystallization studies to understand the mineralization mechanism of recombinant collagen peptide

- Figure 1.** Sketch of RCP mineralization protocol. The graph displays the variation of the conductivity of the reaction mixture *versus* the reaction time. Inset displays the rate of variation of conductivity (dC/dt) respect to the time37
- Figure 2.** XRD (a) and FTIR (b) spectra of synthesized samples: i) Ap; ii) MgAp5; iii) MgAp10; iv) MgAp15; v) RCPAp; vi) RCPMgAp5; vii) RCPMgAp10 and viii) RCPMgAp1538
- Figure 3.** Raman spectra from 400-1150 cm^{-1} (a) and in the ν_1 PO_4 mode region (b) collected for synthesized samples: i) Ap; ii) MgAp5; iii) MgAp10; iv) MgAp15; v) RCPAp; vi) RCPMgAp5; vii) RCPMgAp10 and viii) RCPMgAp15. (c) Curve fittings

of the peak at *ca* 961 cm⁻¹ related to symmetric stretching mode (ν_1) of the tetrahedral PO₄ group in Raman spectra for 4 representative samples Ap (i), MgAp15 (iv), RCPAp(v) and RCPMgAp15 (viii). The vertical graph bar (d) represents the area ratio of ν_1 peaks from ACP (952 cm⁻¹) and Ap (961 cm⁻¹) for all the samples. Data are expressed as mean \pm SD (n=3)40

Figure 4. TEM micrographs of powdered samples synthesized in different conditions: (a) Ap, where inset shows corresponding SAED pattern; (b) MgAp15; (c) RCPAp and (d) RCPMgAp15, where inset shows High-Resolution TEM images of a nanocrystal ..41

Figure 5. (a) TGA/DSC curve of RCP where the thermal degradation temperature of RCP was determined close to 273 °C and (b) TGA curves of Ap, MgAp15, RCPAp and RCPMgAp15 samples42

Chapter 4: Biomimetic mineralization of recombinant collagen peptide to obtain hybrid matrices for bone regeneration

Figure 1. XRD (a) and TGA curves (b) of top (discontinuous line) and base (continuous line) of mineralized scaffolds developed with three different theoretical min/org weight ratio: 40/60, 50/50 and 60/40.....52

Figure 2. SEM micrographs of the top and base of scaffold prototypes designed with increasing initial mineral/organic weight ratio: 40/60, 50/50 and 60/40. Scale bar: 250 μ m. Higher magnification SEM images of the scaffold surface at the base53

Figure 3. FTIR spectra (a) of non-mineralized (RCP) and mineralized matrices in absence (Ap/RCP) and in presence of Mg (MgAp/RCP). b) FTIR spectra of the matrices in the region of OCO stretching vibration mode54

Figure 4. SEM micrographs of RCP (a, d), Ap/RCP (b, e) and MgAp/RCP (c, f) matrices at low (a-c) and higher (d-f) magnification.....55

Figure 5. 3D AFM images of the surface of RCP (a), Ap/RCP (b) and MgAp/RCP (c) matrices. d) Mean surface roughness values for each sample measured from two scan areas: 2.5x2.5 μ m² and 5x5 μ m². Data are expressed as mean \pm SD (n=5). *p<0.05; ****p<0.0001. e) Surface roughness of titania/PLGA composites and natural bone reprinted from Liu H. *et al.*,¹⁸ Copyright (2006) with permission of John Wiley & Sons, Inc: Journal of Biomedical Materials Research Part A56

Figure 6. Macroscopic properties of non-mineralized (RCP) and Ap/RCP and MgAp/RCP mineralized matrices: (a) contact angle and (b) swelling capacity (%). Data

are expressed as mean \pm SD (n=3). *p<0.0556

Chapter 5: Investigations of different crosslinking approaches of mineralized recombinant collagen peptide

Figure 1. Proposed crosslinking reactions involving genipin and amine groups of collagen-based biomaterials. Reprinted from Butler *et al.*,²¹ Copyright (2003), with permission from Wiley Periodicals, Inc., A Wiley Company: Journal of Polymer Science Part A: Polymer Chemistry63

Figure 2. Scheme of reaction during DHT treatment. Reprinted from Haugh *et al.*, Copyright (2011), with permission from Mary Ann Liebert, Inc.: Tissue Engineering Part A64

Figure 3. Different techniques to chemically crosslink scaffold with genipin65

Figure 4. Image of pre (a) and post-crosslinked (b) RCP mineralized slurry before freeze-drying and SEM images of the surface of scaffolds obtained after the freeze-drying protocol. (c) TGA curves of the top (T) and base (B) of non-crosslinked (NC), pre-crosslinked (Pre) and post-crosslinked (Post) hybrid scaffolds66

Figure 5. Optical microscopy images of crosslinked structures after 48 hours immersed in genipin (0.125 wt.%) aqueous solution with increasing ethanol content (% v/v). Scale bar: 500 μ m. SEM images of RCP scaffolds before and after crosslinking by immersion in genipin (0.125 wt.%) solution in aqueous/ethanol volume ratio 10/9067

Figure 6. Images of scaffolds after 24 hours (a) and 48 hours (b) during crosslinking in increasing genipin concentrations in aqueous ethanol solution (90 % v/v ethanol); (c) Swelling capacity of crosslinked scaffolds at increasing genipin concentrations and (d) crosslinking degree of RCP scaffolds after crosslinking with increasing genipin concentrations. Data are expressed as mean \pm SD (n=3)68

Figure 7. Crosslinking degree of three scaffold compositions (RCP, Ap/RCP and MgAp/RCP) crosslinked by two different techniques: genipin and DHT. Data are expressed as mean \pm SD (n=3). ****p<0.000169

Figure 8. Weight loss of crosslinked scaffolds (RCP, Ap/RCP and MgAp/RCP) after 28 days of immersion in PBS medium at 37 °C. Data are expressed as mean \pm SD (n=3) .70

Figure 9. Enzymatic degradation of crosslinked scaffolds after 24 hours in Tris-HCl solution containing collagenase: (a) weight loss and (b) protein release. Data are expressed as mean \pm SD (n=3). *** p<0.001 and ****p<0.000171

Chapter 6: Fabrication of 3D isotropic hybrid scaffolds through freeze-drying and evaluation of their osteoinductive potential

Figure 1. A flow chart summarizing the key points for the design of scaffold structure and the variables of the process that allow tailoring the scaffold porosity. Reprinted from Pawelec *et al.*,⁹ Copyright (2014) with permission from AIP Publishing LLC: Applied Physics Reviews78

Figure 2. XRD (a), FTIR spectra (b) and SEM micrographs (c) of longitudinal and transversal section of RCP, Ap/RCP and MgAp/RCP scaffolds. Scale bar=250 μm 84

Figure 3. (a) Degradation profile of scaffolds after soaking in PBS displayed as weight loss respect to immersion time and (b) cumulative ion released from Ap/RCP (pink line) and MgAp/RCP (blue line) scaffolds in PBS medium determined by ICP-OES as a function of time. Ca^{2+} ion concentration (wt.% respect to the total Ca content in Ap/RCP and MgAp/RCP scaffold) is represented in continuous line (y left axis) whereas Mg^{2+} concentration (wt.% respect to total Mg content in MgAp/RCP scaffold) is displayed in dashed line (y right axis). Data are expressed as mean \pm SD (n=3)86

Figure 4. Cytocompatibility. (a) Live/dead assay to evaluate cell viability after 1 day of cell culture. Live cells in green, dead cells in red on RCP, Ap/RCP and MgAp/RCP scaffolds, respectively (Scale bar: 100 μm). (b) Cell viability evaluated by MTT assay after 1, 3, 7, 14, 21 and 28 days. Data are expressed as mean \pm SEM (n=3). ** $p < 0.01$, and **** $p < 0.0001$ 87

Figure 5. SEM images of MSC cells (white arrows) adhered on the top of the scaffold surfaces after 1 and 7 days of cell culture. Scale bar: 150 μm 88

Figure 6. Cell distribution in the scaffolds after 14 days of cell culture. (a) Microscopic images of the top external surface of scaffolds. (b) Microscopic images of three areas from inner part of scaffolds (top, middle and bottom). Blue: cell nuclei. Scale bar: 200 μm . Graphs display the quantification of the number of cells at the top surface of the scaffolds (c) and in 3 different inner areas of each scaffold. Data are expressed as mean \pm SEM obtained from three different images (n=3). ** $p < 0.01$ and **** $p < 0.0001$ 89

Figure 7. Relative quantification ($2^{-\Delta\Delta\text{Ct}}$) of gene expression profiling of ALP (a), OPN (b) and COL 1 (c) with respect to the expression of the cells grown on RCP (control), using as housekeeping gene GADPH, after 14 and 28 days. (d) Western blot analysis of β -catenin expression in comparison with β -actin (loaded as a control) after 14 and 28

days of cell culture. Data are expressed as mean \pm SEM (n=3). *p< 0.05; ** p< 0.01, ***p<0.001 and ****p<0.000190

Figure 8. Representative immunofluorescence images of MSCs cells after 14 days on the three different scaffold composition. RUNX-2 in red and cell nuclei in blue. Scale bar: 50 μ m.....91

Chapter 7: Expansion and differentiation of hMSCs on biodegradable nanocomposite scaffolds in an bioreactor with mechanical stimulus

Figure 1. Representative scheme of the tissue-engineering concept. Reprinted from Dvir *et al.*, Copyright (2011), with permission from Nature Publishing Group: Nature Nanotechnology.....99

Figure 2. Bioreactor set-up and computational modelling of shear stress due to flow of cell medium through a P[LLA-co-CL] scaffold. (A) Bioreactor set-up composed of: bioreactor cartridge (1), computer-controlled pump (2), a reservoir flask including air filters (3), a septum for cell seeding (4), an adapter to attach a pressure sensor (5) and a rack system that allows easy handling (6). B) A cross section shows the concept of the bioreactor cartridge. From an inlet (7), cell culture medium is guided through the cylindrical scaffold (8) to an outlet (9). The bioreactor housing (10) pressed a silicone tube (11) to the cylinder jacket surface of the scaffold to ensure homogeneous flow conditions in the scaffold. Computational modelling depicts the fluid mechanical conditions in the bioreactor for sealed (C) and unsealed (D) scaffolds. Reprinted from Kleinhans *et al.*, Copyright (2015) with permission of Wiley-VCH Verlag GmbH & Co.....101

Figure 3. Cell viability evaluated by MTT assay after 1 day of cell culture on RCP and MgAp/RCP scaffolds seeded by three different methodologies: 2×10^6 hMSCs seeded in static conditions (St), 2×10^6 hMSCs seeded in dynamic conditions (D2) and 5×10^6 hMSCs seeded in dynamic conditions (D5). Graph displays absorbance at 570 nm that is proportional to metabolic cell activity. Data are expressed as mean \pm SEM (n=3, technical replicates). **p<0.01 and ***p<0.001104

Figure 4. Cell viability evaluated by MTT analysis after 15 days cell culture under dynamic conditions. Images of a piece of RCP (a) and MgAp/RCP (b) scaffolds after 2 hours of addition of MTT reagent. The graph (c) displays the absorbance value at 570 nm after treatment of both cell/scaffold constructions in DMSO. Data are expressed as

mean \pm SEM (n=2 cell patient donors). Microscopic images of the inner areas of RCP (d) and MgAp/RCP (e) scaffolds after 15 days of cell culture under dynamic conditions. Blue: Cell nuclei. Scale bar 50 μ m105

Figure 5. Relative quantification of gene expression of ALP, Col1, OSX, RUNX2 and BSP respect to housekeeping gene (GAPDH) after 15 days of cell culture under dynamic conditions. Data are expressed as mean \pm SEM (n=2 cell patient donors). ***p<0.001106

Figure 6. Scaffold mineralization after 7 days of cell culture under dynamic conditions without (Control) and with mechanical stimulus analysed by Alizarin red staining. Graph displays the calcium content measured quantitatively by dissolving alizarin red. NC represents calcium content of MgAp/RCP scaffolds after 7 days under dynamic flux of cell medium but without cells. Data are expressed as mean \pm SEM (n=3 technical replicates). ** p<0.01 and ***p < 0.001107

Figure 7. Relative quantification of gene expression respect to housekeeping gene (GAPDH) of hMSCs cultured on MgAp/RCP scaffolds after 7 days of dynamic cell culture without (Control) and with mechanical stimulus (Mechanical). Data are expressed as mean \pm SEM (n=3 technical replicates)108

List of tables

Chapter 1: Introduction

Table 1. Classification of bone grafts and graft substitutes together with their clinical evidences. Reprinted from Nandi <i>et al.</i> , Copyright (2010), with permission from Indian Journal of Medical Research	2
Table 2. Elemental composition of the inorganic phases of bone, enamel and dentine of adult human. Reprinted from Pina <i>et al.</i> , Copyright (2015), with permission from WILEY-VCH Verlag GmbH & Co: Advanced Materials.....	3
Table 3. Common markers of osteogenic differentiation. Reprinted from Samavedi <i>et al.</i> , Copyright (2013), with permission from Elsevier: Acta Biomaterialia	16

Chapter 3: Crystallization studies to understand the mineralization mechanism of recombinant collagen peptide

Table 1. Molar concentrations of reactants used for mineralization of Ap nanocrystals in presence of Mg and/or RCP	36
Table 2. Position of (002) peak and average crystalline domain size along the [002] and [310] directions estimated through Scherrer's approximation for apatite nanocrystals synthesized under different conditions. (b) SF, crystallinity index (splitting factor) evaluated from ν_4 PO ₄ vibrational mode in FTIR spectra.	39
Table 3. Chemical composition of Ap, MgAp15, RCPAp and RCPMgAp15 samples. (a) Elemental composition calculated from ICP-OES analysis; (b) RCP and water content (wt.%) determined from TGA curves and (c) specific surface area calculated from BET adsorption. Data are expressed as mean \pm SD (n=3).....	42

Chapter 4: Biomimetic mineralization of recombinant collagen peptide to obtain hybrid matrices for bone regeneration

Table 1. Concentrations of the reagents for the preparation of hybrid matrices with increasing min/org weight ratio	51
Table 2. Macroscopic structure of prototype scaffolds and mineral/organic weight ratio at the top and base of scaffolds calculated by TGA	52

Chapter 5: Investigations of different crosslinking approaches of mineralized recombinant collagen peptide

Table 1. Divisions of the conditions of crosslinking of RCP by scaffold immersion into genipin solution	65
--	----

Chapter 6: Fabrication of 3D isotropic hybrid scaffolds through freeze-drying and evaluation of their osteoinductive potential

Table 1. Variables and parameters tested for the design of isotropic porous scaffolds through freeze-drying of mineralized slurry.....	80
---	----

Table 2. SEM images of longitudinal and transversal section of 3D scaffolds designed by freeze-drying mineralized slurry in Teflon mold at -80 °C and -20 °C in freezer (A) and -40 °C inside freeze-dryer (B)	82
---	----

Table 3. SEM images of longitudinal and transversal section of 3D scaffolds designed by freeze-drying mineralized slurry in well plate at -40 °C in freeze-drier (B) and -20 °C in freezer (A)	83
---	----

Table 4. Chemical composition of mineralized scaffolds analysed by ICP-OES (a). Splitting factor calculated from FTIR spectra of mineralized scaffolds (b). Data are expressed as mean \pm SD of three samples (n=3).....	85
--	----

Table 5. Macroscopic scaffolds properties: mean pore size of dried scaffolds calculated from SEM images (n=60), porosity calculated by gravimetry method (n=5), permeability determined by head falling method (n=5) and young modulus analyzed by DMA (n=5). Data are expressed as mean \pm SD	85
--	----

List of Abbreviations

3D	Three-dimensional
ACP	Amorphous calcium phosphate
AFM	Atomic Force Microscopy
ALP	Alkaline phosphatase
Ap	Apatites
BET	Brunauer-Emmett-Teller
BGLAP	Bone gamma-carboxyglutamic acid-containing protein (Osteocalcin)
BMP-2	Bone morphogenetic protein
BSP	Bone sialoprotein
CaP	Calcium phosphate
CDU	Collagen digestion units
ColI	Collagen type I
DAPI	4',6-diamidino-2-phenylindole
DHT	Dehydrothermal treatment
DMEM	Dulbecco Modified Eagle's Medium
DMSO	Dimethyl sulfoxide
DNA	Deoxyribonucleic acid
DSC	Differential scanning calorimetry
e.g.	<i>Exempli gratia</i> (for example)
ECM	Extracellular Matrix
et al.	<i>Et alii</i> (and others)
FBS	Fetal bovine serum
FTIR	Fourier Transform infrared spectroscopy
GAPDH	Glyceraldehydes-3-phosphate dehydrogenase
h	Hours
HA	Hydroxyapatite
hMSCs	Human mesenchymal stem cells
Hz	Hertz
i.e.	<i>Id est</i> (that is)
ICP-OES	Inductively coupled plasma optical emission spectrometry
MgAp	Magnesium-doped apatites
min	Minutes

mL	Millilitres
MSCs	Mesenchymal stem cells
MTT	3-(4,5-dimethylthiazol-2-yl)-2,5diphenyltetrazolium bromide
OPN	Osteopontin
OSX	Osterix
PBS	Polyphosphate buffered saline
qPCR	Quantitative real-time polymerase chain reaction
RCP	Recombinant collagen type I derived peptide
RGD	Arginine-Glycine-aspartic acid sequence
RNA	Ribonucleic acid
RUNX2	Runt-related transcription factor 2
s	Seconds
SD	Standard deviation
SEM	Scanning Electron Microscopy
SEM	Standard error of the mean
SF	Splitting factor
SPARC	Secreted protein acidic and rich in cysteine (Osteonectin)
SSA	Specific surface area
TE	Tissue Engineering
TEM	Transmission Electron Microscopy
TGA	Thermogravimetry analysis
TGF-β	Transforming growth factor
TNBS	2,4,6-trinitrobenzenesulfonic acid
VEGF	Vascular endothelial growth factor
XRD	X-Ray Diffraction

Chapter 1: Introduction

1.1. Introduction: Overview of Bone tissue Engineering Demand

Bone is a dynamic tissue in continuous process of remodelling consisting in bone resorption by osteoclast followed by the bone formation by osteoblast.¹ Bone tissue is capable to regenerate and heal fracture and defects below a critical size. Nevertheless, some pathological conditions such as large traumatic injury, degenerative diseases, tumour or bone fragility due to the aging population are still a major challenge in common clinical practice which require the use of bone graft for augmenting or stimulating the formation of new bone in the defective areas.^{2,3} The number of procedures requiring bone substitutes is increasing worldwide and will continue to do so as the population ages is increasing.⁴ The high importance of this area of tissue engineering is evidenced by the 2.2 million bone grafting operations worldwide annually, making bone the second most transplanted organs following blood.⁵

Autografts, allografts, xenografts and synthetic bone grafts have been used for bone augmentation (Table 1). Autografts are taken from another part of the same patient's body, usually trabecular bone from the iliac crest of the pelvis. It is considered as the gold standard due to their superior osteogenic potential promoting the proliferation of stem cells and their differentiation and holding viable cells that can form new bone tissue.⁵ While immunogenic responses are minimized, their use is limited due to elevated fracture rates, donor site morbidity, higher care cost and shortage of supply. As alternative, allografts from another donor can allow larger grafts⁶ but have less efficient incorporation and greater potential for immune rejection or pathogen transmission.^{7,8} Xenografts (from other specie) carry even greater risk and are not typically considered for human bone regeneration.⁹ To overcome the limited supply of tissue, a variety of different materials have been explored to restore bone function and regenerate tissue. Artificial bone implants made of metals, ceramics, polymers or composites are synthesized and widely used for bone reconstruction and regeneration.¹⁰⁻¹⁵ These synthesized scaffolds can exhibit satisfactory mechanical properties and biocompatibility, as well as other unique properties. However, as compared with bone autografts and allografts, there are still some congenital deficiencies, such as ion release from metallic scaffolds or low integration of the implant on host tissue, poor strength of

Chapter 1: Introduction

polymeric scaffolds,¹⁶ friability and brittleness of ceramic scaffolds¹⁷ and uncontrollable degradability of composites.¹⁸

Table 1. Classification of bone grafts and graft substitutes together with their clinical evidences. Reprinted from Nandi *et al.*,¹⁹ Copyright (2010), with permission from Indian Journal of Medical Research.

Class	Description	Examples	Properties of action
Autograft based	Used alone		<ul style="list-style-type: none"> • Osteoconductive • Osteoinductive • Osteogenic
Allograft based	Allograft bone used alone or in combination with other materials	Allegro, Orthoblast, Grafton	<ul style="list-style-type: none"> • Osteoconductive, • Osteoinductive
Factor based	Natural and recombinant growth factors used alone or in combination with other materials	TGF- β , PDGF, FGF, BMP	<ul style="list-style-type: none"> • Osteoinductive • Both osteoconductive and osteoinductive with carrier materials
Cell based	Cell used to generate new tissue alone or seeded onto a support matrix	Mesenchymal Stem Cells	<ul style="list-style-type: none"> • Osteogenic. • Both osteogenic and osteoconductive with carriers materials
Ceramic based	Includes CaP, calcium sulfate and bioactive glass used alone or in combination	Osteograft, Osteoset, Novabone	<ul style="list-style-type: none"> • Osteoconductive • Limited osteoinductive when mixed with bone marrow
Polymer based	Includes degradable and non-degradable polymers used alone and in combination with other materials	Cortoss, OPLA, Immix	<ul style="list-style-type: none"> • Osteoconductive • Bioresorbable in degradable polymer
Miscellaneous	Coral HA granules, blocks and composite	ProOsteon	<ul style="list-style-type: none"> • Osteoconductive • Bioresorbable

In 1993, the concept of tissue engineering was formally proposed by Langer and Vacanti²⁰ as an interdisciplinary field that applies the principles of engineering and the life sciences toward the development of biological substitutes that restore, maintain or improve tissue function. It consists in isolating cells from the patient, expanding and seeding them on synthetic scaffolds and later implant the cell/scaffold construction on the defect of the human. The design of a synthetic scaffold is still the core component in bone tissue engineering. The ideal synthetic bone graft should imitate the structure and properties of natural bone extracellular matrix (ECM), possess a similar macro structure to what is found in natural bone, adequate rate of degradation and lack of by-products from degradation of the material. On one hand, to enhance osteoinductive properties, synthetic scaffolds have been incorporated with bone marrow stem cells,^{21,22} drugs and gene delivery,²³ and different growth factors, such as TGF- β ,²⁴ BMP²⁵ and VEGF.^{25,26}

On the other hand, recent researches have revealed that the specific nanotopography, chemistry and nanostructure of biomaterials could not only enhance biocompatibility, but also regulate cell/tissue behaviours without the use of growth factors.²⁷⁻²⁹

1.2. Bone

1.2.1. Bone composition and biology

Bone is a complex cell composite material consisted of a mineralized organic matrix, osteogenic cells, extracellular matrix protein (ECM), growth factors and a complex vascular system. The main components of bone are the organic matrix (25 wt.%), the mineral phase (65 wt.%) and water (10 wt.%).³⁰ The organic phase is mainly constituted by collagen type I and non collagenous proteins such as osteonectin, osteocalcin, osteopontin, bone morphogenetic proteins, bone proteoglycan and bone sialoprotein (less than 10% of the total protein content).³¹ Bone mineral phase is described as hydroxyapatite (HA, $\text{Ca}_{10}(\text{PO}_4)_6(\text{OH})_2$) due to mainly elemental composition. Nonetheless, bone apatite (Ap) is a non-stoichiometric HA that incorporates foreign ions into its structure (i.e., Mg, Sr, Na, CO_3) being carbonate ($\text{CO}_3 \approx 7.4$ wt.%) the more prevalent anion substitute and magnesium ($\text{Mg} \approx 0.7$ wt.%) the main cation replacing calcium.³² Table 2 summarizes the composition of inorganic phases of adult human bone, enamel and dentine.³³

Table 2. Elemental composition of the inorganic phases of bone, enamel and dentine of adult human. Reprinted from Pina *et al.*,³³ Copyright (2015), with permission from WILEY-VCH Verlag GmbH & Co: Advanced Materials.

Composition (wt.%)	Bone	Enamel	Dentin
Calcium (Ca)	34.8	36.5	35.1
Phosphorous (P)	15.2	17.7	16.9
Sodium (Na)	0.9	0.50	0.60
Magnesium (Mg)	0.72	0.44	1.23
Potassium (K)	0.03	0.08	0.05
Zinc (Zn)	0.0126-0.0217	-	-
Fluoride	0.03	0.01	0.06
Chloride (Cl)	0.13	0.30	0.01
Carbonates	7.4	3.5	5.6

The main peculiarity of bone is that it is a dynamic hard tissue that undergoes a continuous remodelling to maintain skeletal strength and integrity, with 10% of the skeleton being replaced annually. Figure 1 illustrates bone-remodelling process in

which haematopoietic stem cell (HSC)-derived osteoclasts resorb bone releasing growth factors and calcium whereas mesenchymal stem cell (MSC)-derived osteoblasts replace the voids with new bone. The remodelling process is regulated by osteoblast commitment, proliferation and differentiation coupled with osteoblast production of type I collagen and its subsequent mineralization to form the calcified matrix of bone. It has been proposed that osteocytes, which are terminally differentiated osteoblasts that are embedded in bone, act as a biological “strain gauges” that respond to change in mechanical pressure and send chemical or electrochemical signals that activate osteoclasts and osteoblast.³⁴

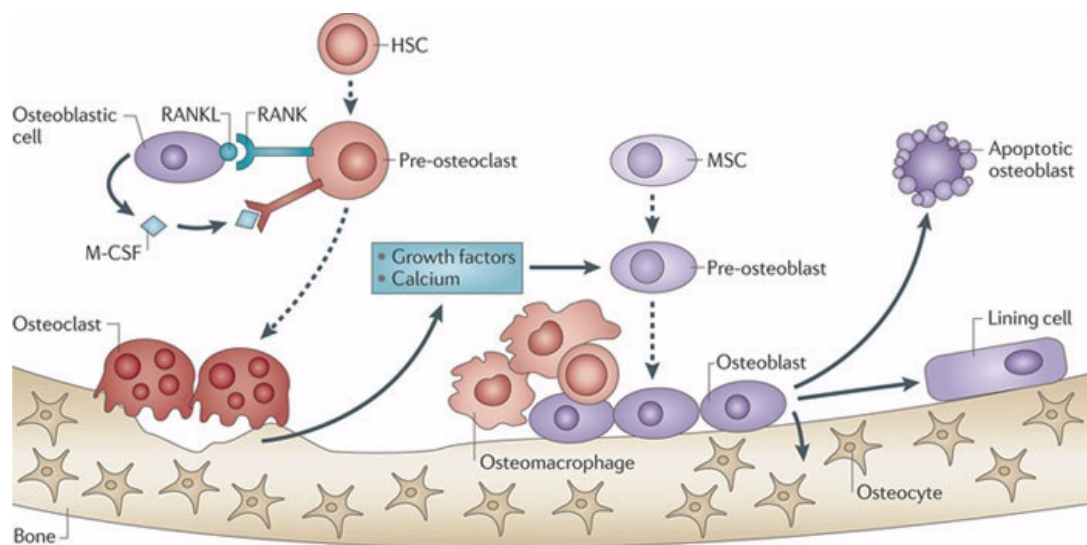


Figure 1. Scheme of bone remodelling. Reprinted from Weillbaecher *et al.*,³⁴ Copyright (2011) with permission of Nature Publishing Group: Nature Reviews Cancer.

1.2.2. Hierarchical structure of bone

Bone is a complex hierarchical structure composed of several levels (Figure 2).³¹ At the macroscopic level, a typical human long bone is generally composed of the cortical bone, the cancellous bone, the periosteum, the endosteum and the articular cartilage. The cortical bone, comprising 80% of the bone mass, is a compact layer surrounding the central marrow cavity exhibiting a high Young’s modulus value and therefore, providing the sufficient mechanical strength to bear weight. On the other hand, cancellous bone (around 20% of the total mass of the skeleton) has an open, honeycomb structure and it is able to dampen the sudden stress. The cartilage is a type of collagen-based connective tissue composed of very large protein–polysaccharide molecules that

provide a tough and flexible matrix. The periosteum, which is found on the surface of the medullary cavity, is a fibrous membrane of connective tissue rich in fibroblasts and progenitor cells that are critical for the formation of new bone. The endosteum is a thin layer of lining cells with relevance during the process of bone remodelling.⁴

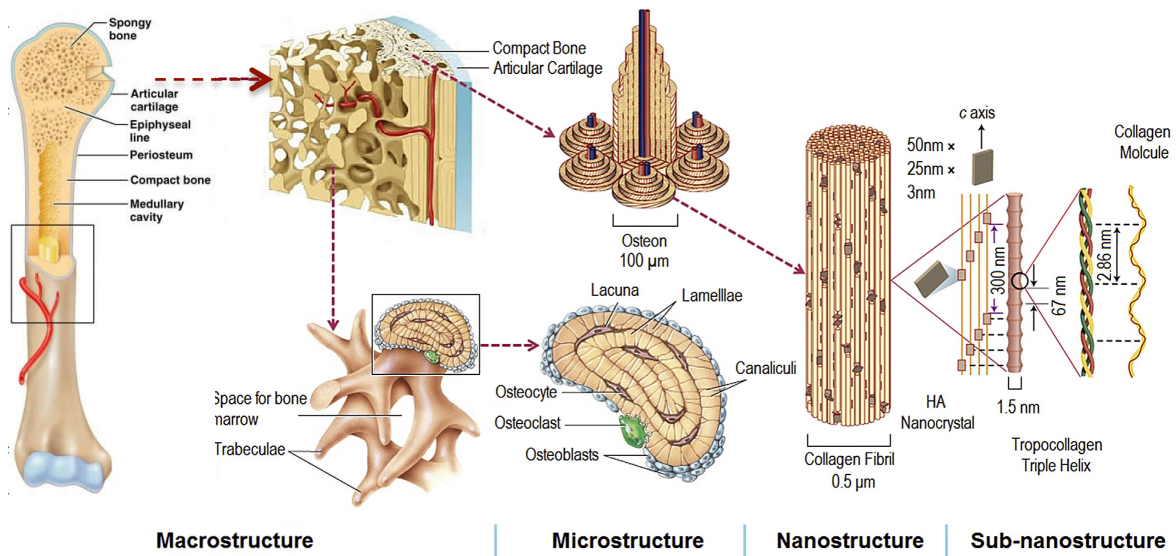


Figure 2. Hierarchical structure of bone. Reprinted from Wang *et al.*,³⁵ Copyright (2016) with permission of Elsevier: Biomaterials.

The nanoscopic level of bone belongs to collagen molecules. There are twenty-eight different types of collagen composed of at least 46 distinct polypeptides.³⁶ Among them, type I collagen is the main organic constituent of bone and consists in two α_1 and one α_2 peptide chains that comprise a repeating glycine (Gly)-X-Y triplet, in which X and Y can be a residue but are usually proline (Pro) and hydroxyproline (Hyp), respectively. The three polypeptide strands are held together in a helical conformation, the tropocollagen triple helix which is described as a long thin semi-rigid rod about 300 nm in length and 1.5 nm in diameter.³⁷ They join together with other tropocollagen molecules in a quasi-hexagonal unit cell containing five tropocollagen monomers (*i.e.*, collagen microfibril) exhibiting a typical D-banding pattern of 67 nm,³⁷⁻³⁹ consisted of two zones, the hole zone (40 nm) and the overlap zone (27 nm). Bone apatite crystallization takes place inside the hole zone (the process is described in the forthcoming section). The collagen microfibrils crosslink into collagen fibre with a diameter lower than 500 nm and a length lower than 1 cm.³⁷ Mineralized collagen fibrils mostly present in bundles or arrays aligned along their lengths. These bundles are,

however, not discrete. Fibres from one bundle may fuse with a neighbouring bundle prompting to fibril arrays that organized in a variety of patterns forming sheets. In the case of bone, the sheets are assembled with bone cells (osteocytes) that reside between adjacent layers, and together these are either stacked in parallel arrays (lamellar bone) or concentrically arranged into a cylindrical structure referred to as the osteon. Osteons are formed with significant cellular activity and remodelling; osteoclasts resorb bone and form a tunnel, and osteoblasts subsequently lay down lamellae in stacked layers until only a small channel (Haversian canal) is left behind. These channels serve as a conduit for nerves and blood supply whereas small channels (canaliculi), which are interconnected in the marrow cavity, provide microcirculation of blood and nutrients to the cells.³⁰

1.2.3. Bone biomineralization

In organism, biomineralization offers structural support and mechanical strength as well as a wide variety of important biological function such as protection, motion, cutting and grinding, buoyancy, optical, magnetic and gravity sensing or storage.⁴⁰ These properties rely on the complex structure of biominerals which results from biologically controlled mineralization that involves the specialized regulation of mineral deposition and results in functional materials with specific crystallochemical properties such as uniform particle sizes, well-defined structures and compositions, high levels of spatial organization, complex morphologies, controlled aggregation and texture, preferential crystallographic orientation and higher-order assembly into hierarchical structures.⁴⁰

Early studies on bone formation have been able to establish the spatial and crystallographic relationship between collagen and the bone apatite (Ap). Conventional transmission electron microscopy (TEM) studies, combined with X-ray and electron diffraction have shown that the Ap crystals nucleate and grow within the 40 nm gaps present in the collagen fibril, and have their *c*-axis aligned parallel to the long axis of collagen fibres (Figure 3).^{31,41-43} Bone apatites are plate-shaped with a length between 30-50 nm, a width of 20-25 nm and a thickness of 1.5-4 nm.^{44,45} It is still unclear how the final Ap crystallites form within the collagen fibrils with plate-shape morphology and what is the role of the collagen matrix and the non-collagenous proteins (NCPs) on this process.

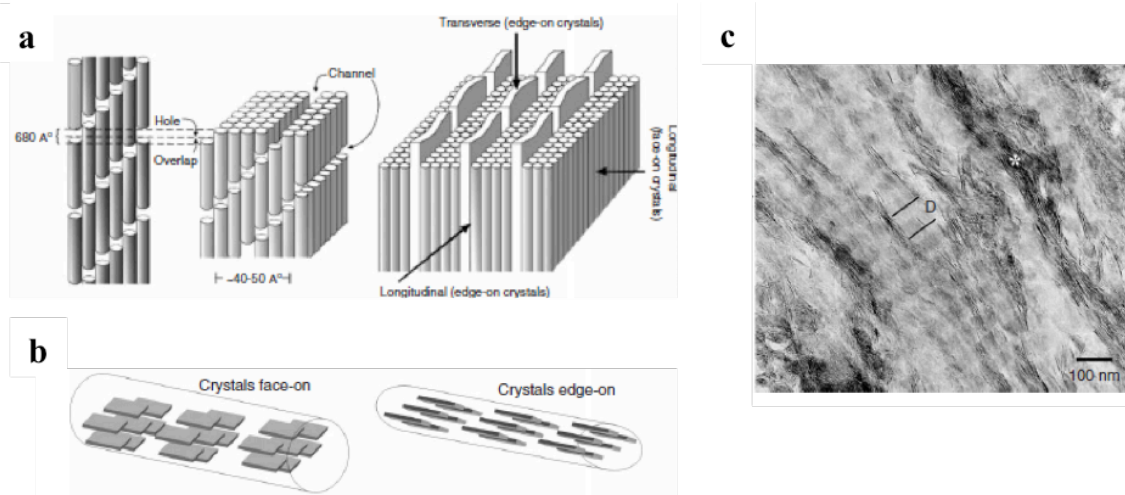


Figure 3. Nanoscopic view of mineralized collagen fibre structure and organization. (a) Model of mineralized collagen fibrils showing the arrays of the plate-like apatite nanocrystals in the gap zones formed in staggered arranged collagen fibrils. (b) Face-on and edge-on projections of the crystals in the mineralized fibril. (c) TEM micrograph of an array of the mineralized fibrils from human dentin. Reprinted from Beniash *et al.*,⁴⁶ Copyright (2011) with permission from John Wiley & Sons, Inc: Wiley Interdisciplinary Reviews, Nanomedicine and Nanobiotechnology.

Bone apatite nucleation and growth requires a local environment with sufficient supersaturation in the mineral precursors. Two main modes have been proposed: a) calcium phosphate (CaP) first nucleates within the matrix vesicle membrane during phase 1 of biologic mineralization and then the phase 2 of biologic mineralization begins with the breakdown of matrix vesicles membranes, exposing the CaP mineral to the extracellular fluid⁴⁷⁻⁴⁹ and b) the CaP crystals are actively nucleated from solution by the NCPs associated to the collagen gap zones, without intervention of cellular processes.^{41,50} A large area of biomineralization research is focused on the role of NCPs, including bone sialoprotein (BSP), osteonectin (ON), osteopontin (OPN) and osteocalcin (OCN).^{51,52} The primary amino acid sequence of these proteins often includes a high density of aspartic acid and glutamic acid residues, which have a high affinity for calcium ions.⁵³ Anionic polypeptides like polyaspartic acid (pAsp)^{30,54,55} and fetuin^{56,57} that mimic the polyanionic character of the NCPs have been used to achieve *in vitro* collagen mineralization by means of polymer-induced liquid precursor phase.³⁰ It has been proposed that the fluidic character of the amorphous precursor phase (ACP) allows the penetration of ACP into the 40 nm nanoscopic gaps in the collagen fibrils by capillary action, thereby facilitating the intrafibrillar mineralization of collagen fibres. Since the ACP-pAsp complex is negatively charged, the most favourable entry sites in

the collagen should be the ones with the highest positive charge and therefore the lowest electrostatic potential energy to interact with the complex, which was indeed observed experimentally.⁵⁴ On the other hand, a recent work demonstrated the clear role of the collagen matrix in directing the morphology and orientation of the Ap nanocrystals without the presence of additives. It was shown that collagen molecules also got infiltrated with Ap nanocrystals by simply using reaction solutions containing very high concentrations of calcium and phosphate ions⁵⁸ in the absence of any type of additive mimicking the working of NCPs. The *in vivo* bone mineralization mechanism still remains unclear though.

1.3. Biomaterials for bone regeneration inspired in bone biomineralization

In the last decades, scientists have tried to learn from nature how to design biomimetic biomaterials inspired by the hierarchical complex structure of bone and other natural mineralized tissues. The design of nanocomposites, that recapitulate the organization of natural bone ECM, has certainly constituted a major breakthrough in bone tissue engineering. Considering that in nature, macromolecular frameworks in the form of an organic matrix are commonly used to control biomineralization (crystal nucleation and growth) in extracellular sites, a wide range of biomaterials for bone regeneration have been developed by bioinspired mineralization of natural or synthetic polymers, proteins and/or peptides.

1.3.1. Design of biomaterials via biomimetic mineralization of natural polymers

The development of nanocomposite scaffolds has been inspired on natural biomineralization processes that drive the formation of new bone in mammals. Organic macromolecules such as natural polymers (i.e., collagen, cellulose, chitosan, gelatin, alginate and fibroin) have been used as template/matrix to develop nanocomposite scaffolds via biomimetic mineralization. The main advantage concerning the use of natural polymers is the possibility to be extracted in massive amounts from a number of sources (including waste products) representing a nearly unlimited, safe, cheap and environment-friendly source of raw materials. For instance, bio-inspired mineralization of natural collagen (e.g., collagen extracted from horse tendon) has been extensively applied for the development of advanced biomaterials for bone regeneration. The process enables the activation of various mechanisms driving the assembling, organization and mineralization of natural collagen thus generating hybrid fibrous

materials having compositional and morphological features similar to those of newly formed bone.^{22,59,60} Denatured collagen, gelatin, has been also used as organic matrix for bone tissue engineering.⁶¹⁻⁶³ Gelatin is free of immunogenic concerns and contains integrin binding sites which are important for cell adhesion.⁶⁴ Porous scaffolds made of gelatin-HA and obtained through biomimetic precipitation method have been also proposed for bone tissue regeneration.⁶¹ Other natural polymers such as chitosan and silk are especially known for their excellent mechanical properties.^{65,66} Hence, nanocomposite HA/chitosan scaffolds with compositional and structural features close to natural bone ECM, have been shown to support bone marrow-derived mesenchymal stromal cell (BMSC) adhesion, spreading and promotion as well as induce their osteogenic differentiation *in vitro* and *in vivo*.⁶⁵

Nevertheless, the use of natural polymers might present some limitations such as thermal instability, possible contamination with pathogenic substances and/or low possibility to introduce specific sequence modifications to enhance scaffold biofunctionality.

1.3.2. Biomimetic mineralization of synthetic polymers

To overcome the above-mentioned shortcomings, material scientists have explored the use of synthetic polymers for bone regeneration since they can be produced in large uniform quantities and have a long self-time. Moreover, synthetic polymers are highly useful in biomedical field since their properties (i.e., porosity, degradation time and mechanical characteristics) can be tailored for specific applications.⁶⁷ In bone regeneration field, the development of composite materials consisting of synthetic polymers and calcium phosphate minerals (CaP) has attracted a great attention owing to their wide range of unique properties, particularly in terms of their ability to emulate the soft/hard composite structure of bone. The synergistic role of polymers providing viscoelastic properties and CaP promoting osteoconductivity of designed scaffolds has yielded materials that surpassed the resistance to fracture, structural integrity and stiffness of the individual components, making up for the low compressive strength of the former and brittleness and the lack of malleability of the latter.⁶⁸ Synthetic polymers used on biomedical field can be divided in two main groups: biodegradable and non-biodegradable. Composites for bone regeneration have been developed by incorporation of CaP in non-biodegradable polymers such as polysiloxanes,⁶⁹ poly(methyl

methacrylate)⁷⁰ and other acrylics,⁷¹ polyethylene⁷² and polypropylene⁷³ among olefins and poly(vinyl alcohol)⁷⁴ among haloalkanes. Biodegradable polymers used in combination with CaP include poly(L-lactic acid, PLLA),⁷⁵ poly(lactic-co-glucolic acid, PLGA),⁷⁶ poly(ϵ -caprolactone)^{77,78} various polyanhydrides and some of the more rarely used polymers, counting poly-p-dioxanone,⁷⁹ poly(trimethylene carbonate)⁸⁰ and many others.

1.3.3. Self-assembly and mineralization of synthetic peptides

Last decades, there has been an increasing interest in the use of synthetic peptides as bioactive matrices for regenerative medicine promoting the interactions with cells and eliciting desired behaviours *in vivo*.⁸¹ The synthetic peptides can be designed at molecular level to self-assemble and create supramolecular nanostructures that mimics ECM. Among them, peptide amphiphiles (PA) have been extensively studied as matrix for regenerative medicine.⁸²⁻⁸⁶ The group of Stupp *et al.*⁸⁵ investigated the self-assembly and mineralization of PA nanofibers containing RGD sequences at controlled concentrations and phosphorylated serine residues to template hydroxyapatite. The mineralized PA nanofibers appeared to promote osteogenic differentiation of mesenchymal stem cells (MSCs), based on alkaline phosphatase and osteopontin expression of hMSCs cultured on PA gels.⁸⁶

1.3.4. Bio-inspired self-assembled and mineralization of recombinant proteins

Other alternative to the biopolymers is the recombinant protein expression system.⁸⁷ Recombinant proteins present several benefits such as controlled and reproduced chemical composition and molecular weight avoiding the risk of associated infectious diseases as in the case of biopolymers and the possibility to be produced at large-scale. There are several systems for protein expression. For instance, some works have described the production of recombinant gelatin-like proteins in *Escherichia coli*. Alike to the natural amino acid sequence of collagen triple-helix forming domain, synthetic genes are constructed from repeating (Gly-Xaa-Yaa)_n-encoding oligonucleotides, where Xaa and Ya are often proline.⁸⁷⁻⁸⁹ Conversely, expression levels usually obtained in *E.coli* were rather low and the purification of the intracellular produced protein can be difficult. Therefore, several authors focused on the expression of high levels of type I homotrimer and heterotrimer and type II and type III collagen by yeast. As example, recombinant gelatin has been expressed in yeast such as *Pichia pastoris*^{40,90,91} in both

non-hydroxylated and hydroxylated forms. On the other hand, other systems such as mammalian and insect cells, transgenic tobacco plants, transgenic mice, transgenic silkworm have been engineered to produce recombinant collagen molecules.⁹²

Fujifilm Europe B.V. has developed a technology to produce recombinant collagen peptide (RCP) through a yeast-based fermentation process. Like traditional collagen and gelatin, RCP consists of the characteristic collagen triplet amino acid base structure (Gly-X-Y). Moreover, the DNA technique allows adjustment of the amino acid sequence of the RCP. Special functionalities can easily be added, such as additional cell binding sites (arginine-glycine-aspartic acid sequences, RGD) or increased number of (electrical charging) amines. RGD sequence is found in cell adhesive proteins like vitronectin, laminin, and fibronectin and is recognized by the cell's transmembrane integrin receptors that tether the cell cytoskeleton to the fibre of ECM, forming local focal adhesion. RGD has demonstrated *in vitro* regulation of cell adhesion and differentiation, and more importantly, enhancements in *in vivo* responses, including bone formation and integration.⁹³ For instance, *in vivo* studies indicated that microspheres produced with human recombinant gelatin containing RGD sequences are faster infiltrated by cells, display a faster degradation profile and shows a rapidly stroma formation compare with microsphere developed with usual recombinant gelatin (without RGD sequences).⁹⁴ This material has been also explored as a vehicle to delivery cells (ADCs)⁹⁵ and as a promising controlled release system of BMP-2.⁹⁶

Few studies on the mineralization potential of recombinant human like collagen (RHLC) have been carried out until now.⁹⁷⁻⁹⁹ For instance, Wang *et al.* studied mineralization of RHLC as an initial stage on the use of mineralized RHLC for bone tissue engineering.⁹⁹ They indicated that RHLC prefers to chelate calcium ions in solution and so subsequently regulates the mineralization forces to obtain RHLC-HA composites. Furthermore, they have evaluated the osteoinductive potential of porous scaffolds made of poly-lactic acid and mineralized recombinant-human collagen non-loaded¹⁰⁰ and loaded with synthetic BMP-2-derived peptide.¹⁰¹

Despite the recent studies on the development of nanocomposite materials for bone regeneration through biomineralization of recombinant peptides, engineering of 3D scaffold structures to ensure cell integration and their differentiation to osteogenic lineage remains still in its infancy.

1.4. Scaffold design for bone tissue engineering

Scaffold design and fabrication for bone tissue engineering should accomplish several requirements: three-dimensional and highly porous structure with an interconnected pore network and surface properties which promote cell-biomaterial interactions, cell adhesion and ECM deposition; be biocompatible, not elicit an immune response; be biodegradable with a controllable degradation rate to compliment cell/tissue in-growth and maturation; its mechanical properties should match those of the tissue at the site of implantation; provoke a minimal degree of inflammation or toxicity *in vivo* and the scaffold structure should be easily and efficiently reproducible in various shapes and sizes.^{16,102} Furthermore, scaffolds should be osteoconductive, osteoinductive and promote osseointegration *in vivo*. To match all or majority of this function, a thorough understanding of the chemistry and physicochemical properties of the tissue to be engineered and the materials used in this process is required.

1.4.1. Biocompatibility

Biocompatibility represents the ability of a material to perform an appropriate response with respect to a specific medical application, without eliciting an immune response. One of the major concerns is the release of by-products that may be biocompatible without proof of elimination from the body (biodegradable scaffolds) or can be eliminated through natural pathways from the body, either by simple filtration of by-products or after their metabolization (bioresorbable scaffolds).¹⁶ The capacity of the surrounding tissue to eliminate the by-products may be low due to poor vascularization or low metabolic activity, leading to a build up of the by-products thereby causing local temporary disturbances. For instance, polylactide scaffolds promote a decrease of local pH leading to inflammatory reactions.¹⁰³

1.4.2. Degradation kinetics

The ideal scaffolds should be bioresorbable and degrade under physiological environments by the surrounding tissues in order to allow the ultimate replacement of scaffold material with newly formed bone without the need for surgical removal. In order to obtain a desired and controllable biodegradation rate for practical application, the scaffold design should consider the chemical composition and structure of bulk materials, as well as the properties of coatings and the specific biological environment.

For instance, hybrids/composites comprising different kinds of polymers or polymer/ceramic/bioglass can enhance mechanical properties, biological functions and simultaneously can modulate their biodegradation behaviour.^{15,104-106} Furthermore, ECM-derived biomolecules are accessible to surface erosion due to their high enzymatic sensitivity, which induces the rapid degradation of scaffolds made from these materials, like chitosan, collagen and gelatin.^{15,105,107,108} The incorporation of inorganic nanoparticles, the addition of dual organic components or the crosslinking of the organic components allow the control of their degradation rate.^{105,109,110}

In bone tissue engineering, the degradation and resorption kinetics of the scaffold have to be controlled in such a way that the bioresorbable scaffold retains its physical properties for at least 6 months to enable cell and tissue remodelling.¹⁶ Among difference anatomical and physiological variables, the type of tissue that is aimed to be engineered has a profound influence on the degree of remodelling since the remodelling in cancellous bone takes 3-6 months while it takes twice as long, approximately 6-12 months, in the case of cortical bone.¹¹¹

1.4.3. Mechanical properties

For bone regeneration, the mechanical properties of a biomaterial are critical to the success of the implant and depend on the tissue into which they are implanted. The scaffold is responsible for (temporal) mechanical support and stability at the tissue-engineering site until the new bone is fully matured. Therefore it is critical that the scaffold temporally withstands and conducts the loads and stresses that the new tissue will ultimately bear. The scaffold should resist changes in shape resulting from the introduction of cells into the scaffold (each of which should be capable of exerting tractional forces) and from wound contraction forces that would be evoked during tissue healing *in vivo*.¹¹¹ The mechanical properties of bulk biomaterials are altered by their processing into scaffolds of various pore sizes and pore orientations,⁵ the crosslinking methodology of the organic matrix^{112,113} or by combining several materials (polymers, ceramics and metals).

1.4.4. Surface properties

The ideal scaffolds should mimic the natural extracellular matrix (ECM) as much as possible, since the ECM found in natural tissues supports cell attachment, proliferation, and differentiation. The scaffolds should consist of appropriate biochemistry and

nano/micro-scale surface topographies, in order to formulate favourable binding sites to actively regulate and control cell and tissue behaviour, while interacting with host cells. Certain surface features can facilitate the adsorption of cell-adhesive proteins and thus provide conditions for the formation of stable focal adhesive complexes.¹⁰ The bioactive surfaces of nanomaterials (Figure 4) mimicking those of natural bones promote greater amounts of protein adsorption and efficiently stimulate more new bone formation than conventional materials.¹¹⁴

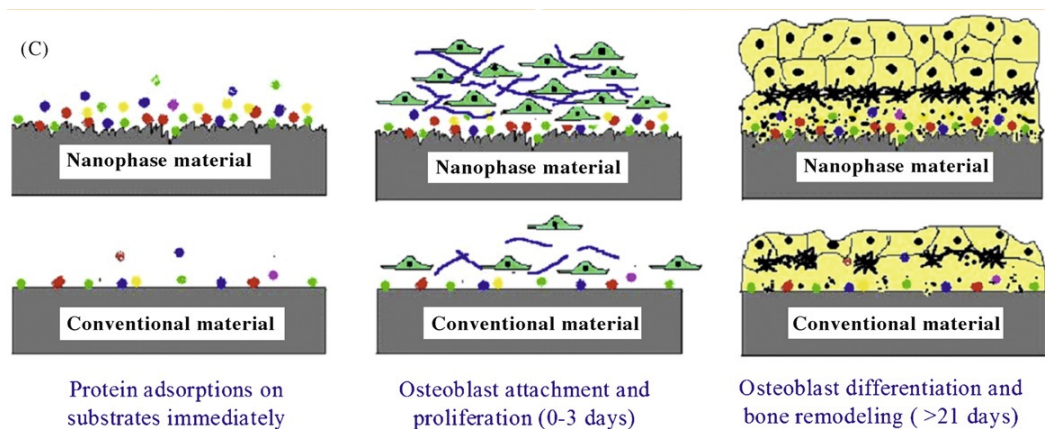


Figure 4. Schematic illustration of the mechanism by which nanomaterial surface properties may be superior to conventional materials for bone regeneration. Reprinted from Zhang *et al.*,¹¹⁴ Copyright (2009) with permission of Elsevier: Nanotoday.

A wide variety of techniques have been implemented in order to functionalize material surface with the aim of enhancing the biofunctionality and bioactivity of already used synthetic scaffolds such as metallic implants (titanium) or synthetic polymer scaffolds (i.e. PLLA, PCL, PLGA). They can be divided in two groups according to Wu *et al.*:⁴ surface functionalized chemistry and surface functionalized structure. The former is subdivided in several subgroups: coating with calcium phosphate mineral (bioactive component), ECM proteins or even hybrid coatings (comprised of biomolecules and calcium phosphate), inducing biomineralization by soaking in simulated body fluid (SBF) and surface polymerization (i.e., aminolysis, hydrolysis, electron beam radiation or plasma polymerization). On the other hand, surface structure (topographies, roughness and nano-architectures) can be modified via chemical (i.e., anodization, hydrolysis, chemical vapour diffusion, sol-gel or biomineralization) and physical treatment (i.e., plasma spraying, magnetron sputtering or inert-ion texturization) in order to cater especially to particular biological applications. Engineering surface by combining both, chemistry and structural functionalization will provide exceptional

scaffold interfacial properties. For instance, the calcium phosphate coating of scaffold will allow to tailor both, topography (depending on coating parameters) and chemistry by ions substitution on crystal lattice (Sr, Mg or CO₃) or functionalization of mineral surface (incorporation of proteins or drugs¹¹⁵).⁴

1.4.5. Scaffold microstructure

Scaffold microstructure (porosity, pore size, pore shape and interconnectivity) will dictate the surface area available for the adhesion and growth of cells both *in vitro* as well as *in vivo*. The porosity is associated to the free available space (void volume of a solid) for cell penetration and tissue ingrowth. The porosity of a biomaterial can be modulated through different techniques such as salt leaching, gas foaming, phase separation, freeze-drying and sintering. It can be measured by different techniques (e.g., mercury intrusion porosimetry, gravimetry method, liquid displacement and micro-CT). Scaffolds made of PLL and β -tricalcium phosphate with porosity gradient and controlled pore size showed a more tissue ingrowth and new bone formation in the areas of higher porosity after implantation in rabbit craniums.¹¹⁶ However, it is hard to directly link the scaffold porosity to cell performance. Although increased porosity and higher pore size facilitate bone ingrowth, it also compromises the structural integrity of the scaffold, and if the porosity becomes too high it may adversely affect the mechanical properties and the degradation kinetics of the scaffold at the same time.¹¹¹

The effect of pore size and pore interconnectivity on bone tissue regeneration has been explored by many researches along the last decades. Small pores favour hypoxic conditions and induce osteochondral formation before osteogenesis occurs.¹¹⁷ The optimum pore size for bone regeneration has been indicated between 200–350 μm .^{118,119} Pore interconnectivity is also critical to provide mass transfer of oxygen and nutrients.^{3,120} In fact, pore interconnections smaller than 100 μm were found to restrict vascular penetration.¹⁶

Pore interconnectivity and tortuosity will affect the scaffold permeability that simultaneously will influence the gas and liquid transport inside scaffolds. For bone regeneration, especially for the repair of large-scale defects, sufficient nutrients need to be delivered into the inner pores to support cell survival. Greater scaffold permeability has been shown to promote bone penetration and vascularization *in vivo*.¹²¹

1.4.6. Osteoconduction, osteoinduction and osseointegration

As we mentioned before, scaffolds should be osteoconductive, osteoinductive and imply osseointegration.¹²² Osteoinduction is the recruitment and stimulation of undifferentiated, pluripotent cells to differentiate in bone-forming cells (preosteoblasts, osteoblasts, and finally osteocytes). There are several genes and proteins involved in the osteogenic differentiation and they are commonly used as markers of the osteoblastic phenotype (Table 3). Osteoinductive potential of scaffolds has been tested by analysing the new bone formation after injection of the scaffold into an ectopic bed. Osteoconduction refers to the property of the material to support the growth of new bone on its surface or down into pores or channels. After a trauma, this growth can occur by existing preosteoblasts and osteoblasts or by differentiation into these cells (osteoinduction). The process of osteoconduction depends on the nature of the material as well as the presence of certain growth factors and the sufficient vascularization. Respect to osseointegration, it represents the direct, microscopic contact between living bone and an implant material. It has been histologically defined as the direct anchorage of an implant by the formation of bony tissue around the implant without the growth of fibrous tissue at the bone implant interface.

Table 3. Common markers of osteogenic differentiation. Reprinted from Samavedi *et al.*,¹⁰ Copyright (2013), with permission from Elsevier: Acta Biomaterialia.

Name	Type	Primary function during differentiation
Runx2	Transcription factor	• Helps in the differentiation of MSCs into immature osteoblasts
Osterix	Transcription factor	• Acts downstream of Runx2 and promotes osteogenesis
Alkaline Phosphatase (ALP)	Enzyme	• Increases local concentration of phosphate ions that in turn initiate mineral growth
Type I Collagen	ECM protein	• Mineral nucleation begins at the junction between two collagen fiber bundles
Osteopontin (OPN)	ECM protein	• Acts as an inhibitor towards irregular formation of mineral crystals
Bone sialoprotein (BSP)	ECM protein	• Binds to Ca ²⁺ via free hydroxyl groups and promotes nucleation of mineral
Osteocalcin (OCN)	ECM protein	• Regulates mineral growth, direction, size and quantity during late stages
Osteonectin (ONN)	ECM protein	• Similar role to that played by osteocalcin
Bone morphogenic protein 2 (BMP2)	Growth factor	• Secreted by immature osteoblasts
Bone morphogenic protein 7 (BMP7)	Growth factor	• Similar role to that played by BMP2

References

1. Sommerfeldt, D. and Rubin, C. Biology of bone and how it orchestrates the form and function of the skeleton. *Eur Spine J* **10**, S86, 2001.
2. Black, C.R., Goriainov, V., Gibbs, D., Kanczler, J., Tare, R.S. and Oreffo, R.O. Bone tissue engineering. *Current molecular biology reports* **1**, 132, 2015.
3. Salgado, A.J., Coutinho, O.P. and Reis, R.L. Bone tissue engineering: state of the art and future trends. *Macromol Biosci* **4**, 743, 2004.
4. Wu, S., Liu, X., Yeung, K.W., Liu, C. and Yang, X. Biomimetic porous scaffolds for bone tissue engineering. *Mater Sci Eng R* **80**, 1, 2014.
5. Henkel, J., Woodruff, M.A., Epari, D.R., Steck, R., Glatt, V., Dickinson, I.C., Choong, P.F., Schuetz, M.A. and Hutmacher, D.W. Bone regeneration based on tissue engineering conceptions—a 21st century perspective. *Bone research* **1**, 216, 2013.
6. Mankin, H.J., Gebhardt, M.C., Jennings, L.C., Springfield, D.S. and Tomford, W.W. Long-term results of allograft replacement in the management of bone tumors. *Clin Orthop* **324**, 86, 1996.
7. Buck, B., Malinin, T.I. and Brown, M.D. Bone Transplantation and Human Immunodeficiency Virus: An Estimate of Risk of Acquired Immunodeficiency Syndrome (AIDS). *Clin Orthop* **240**, 129, 1989.
8. Mankin, H.J., Hornicek, F.J. and Raskin, K.A. Infection in massive bone allografts. *Clin Orthop* **432**, 210, 2005.
9. Butler, D. Last chance to stop and think on risks of xenotransplants. 1998.
10. Samavedi, S., Whittington, A.R. and Goldstein, A.S. Calcium phosphate ceramics in bone tissue engineering: a review of properties and their influence on cell behavior. *Acta Biomater* **9**, 8037, 2013.
11. Anselme, K. Osteoblast adhesion on biomaterials. *Biomaterials* **21**, 667, 2000.
12. Rai, R., Keshavarz, T., Roether, J., Boccaccini, A.R. and Roy, I. Medium chain length polyhydroxyalkanoates, promising new biomedical materials for the future. *Mater Sci Eng R* **72**, 29, 2011.
13. Li, Z., Gu, X., Lou, S. and Zheng, Y. The development of binary Mg–Ca alloys for use as biodegradable materials within bone. *Biomaterials* **29**, 1329, 2008.
14. Alvarez, K. and Nakajima, H. Metallic scaffolds for bone regeneration. *Materials* **2**, 790, 2009.
15. Mahony, O., Tsigkou, O., Ionescu, C., Minelli, C., Ling, L., Hanly, R., Smith, M.E., Stevens, M.M. and Jones, J.R. Silica - Gelatin Hybrids with Tailorable Degradation and Mechanical Properties for Tissue Regeneration. *Adv Funct Mater* **20**, 3835, 2010.
16. Hutmacher, D.W. Scaffolds in tissue engineering bone and cartilage. *Biomaterials* **21**, 2529, 2000.
17. Liu, B., Lin, P., Shen, Y. and Dong, Y. Porous bioceramics reinforced by coating gelatin. *J Mater Sci Mater Med* **19**, 1203, 2008.
18. Ang, K., Leong, K., Chua, C. and Chandrasekaran, M. Compressive properties and degradability of poly (ϵ - caprolactone)/hydroxyapatite composites under accelerated hydrolytic degradation. *J Biomed Mater Res A* **80**, 655, 2007.
19. Nandi, S., Roy, S., Mukherjee, P., Kundu, B., De, D. and Basu, D. Orthopaedic applications of bone graft & graft substitutes: a review. 2010.
20. Langer, R. and Vacanti, J.P. Tissue engineering. *Science* **260**, 920, 1993.
21. Yoon, I.-S., Chung, C.W., Sung, J.-H., Cho, H.-J., Kim, J.S., Shim, W.-S., Shim, C.-K., Chung, S.-J. and Kim, D.-D. Proliferation and chondrogenic

- differentiation of human adipose-derived mesenchymal stem cells in porous hyaluronic acid scaffold. *J Biosci Bioeng* **112**, 402, 2011.
22. Kon, E., Delcogliano, M., Filardo, G., Fini, M., Giavaresi, G., Francioli, S., Martin, I., Pressato, D., Arcangeli, E., Quarto, R., Sandri, M. and Marcacci, M. Orderly osteochondral regeneration in a sheep model using a novel nanocomposite multilayered biomaterial. *J Orth Res* **28**, 116, 2010.
 23. Castaño, I.M., Curtin, C.M., Shaw, G., Murphy, J.M., Duffy, G.P. and O'Brien, F.J. A novel collagen-nanohydroxyapatite microRNA-activated scaffold for tissue engineering applications capable of efficient delivery of both miR-mimics and antagonists to human mesenchymal stem cells. *J Control Release* **200**, 42, 2015.
 24. DeFail, A.J., Chu, C.R., Izzo, N. and Marra, K.G. Controlled release of bioactive TGF- β 1 from microspheres embedded within biodegradable hydrogels. *Biomaterials* **27**, 1579, 2006.
 25. Hernández, A., Reyes, R., Sanchez, E., Rodríguez - Évora, M., Delgado, A. and Evora, C. In vivo osteogenic response to different ratios of BMP - 2 and VEGF released from a biodegradable porous system. *J Biomed Mater Res A* **100**, 2382, 2012.
 26. Kempen, D.H., Lu, L., Heijink, A., Hefferan, T.E., Creemers, L.B., Maran, A., Yaszemski, M.J. and Dhert, W.J. Effect of local sequential VEGF and BMP-2 delivery on ectopic and orthotopic bone regeneration. *Biomaterials* **30**, 2816, 2009.
 27. Boyan, B.D., Hummert, T.W., Dean, D.D. and Schwartz, Z. Role of material surfaces in regulating bone and cartilage cell response. *Biomaterials* **17**, 137, 1996.
 28. Chang, H.-I. and Wang, Y. Cell responses to surface and architecture of tissue engineering scaffolds: INTECH Open Access Publisher; 2011.
 29. Stevens, M.M. and George, J.H. Exploring and engineering the cell surface interface. *Science* **310**, 1135, 2005.
 30. Olszta, M.J., Cheng, X., Jee, S.S., Kumar, R., Kim, Y.-Y., Kaufman, M.J., Douglas, E.P. and Gower, L.B. Bone structure and formation: A new perspective. *Mater Sci Eng R* **58**, 77, 2007.
 31. Weiner, S. and Wagner, H.D. The Material Bone: Structure-Mechanical Function Relations. *Annu Rev Mater Sci* **28**, 271, 1998.
 32. Gómez-Morales, J., Iafisco, M., Delgado-López, J.M., Sarda, S. and Drouet, C. Progress on the preparation of nanocrystalline apatites and surface characterization: Overview of fundamental and applied aspects. *Prog Cryst Growth Ch* **59**, 1, 2013.
 33. Pina, S., Oliveira, J.M. and Reis, R.L. Natural - Based Nanocomposites for Bone Tissue Engineering and Regenerative Medicine: A Review. *Adv Mater* **27**, 1143, 2015.
 34. Weilbaecher, K.N., Guise, T.A. and McCauley, L.K. Cancer to bone: a fatal attraction. *Nat Rev Cancer* **11**, 411, 2011.
 35. Wang, X., Xu, S., Zhou, S., Xu, W., Leary, M., Choong, P., Qian, M., Brandt, M. and Xie, Y.M. Topological design and additive manufacturing of porous metals for bone scaffolds and orthopaedic implants: A review. *Biomaterials* **83**, 127, 2016.
 36. Brinckmann, J. Collagens at a glance. *Collagen: Springer*; 2005. pp. 1.
 37. Shoulders, M.D. and Raines, R.T. Collagen structure and stability. *Annu Rev Biochem* **78**, 929, 2009.

38. Orgel, J.P.R.O., Miller, A., Irving, T.C., Fischetti, R.F., Hammersley, A.P. and Wess, T.J. The In Situ Supermolecular Structure of Type I Collagen. *Structure* **9**, 1061, 2001.
39. Hulmes, D.J. Building collagen molecules, fibrils, and suprafibrillar structures. *J Struct Biol* **137**, 2, 2002.
40. Xu, A.-W., Ma, Y. and Cölfen, H. Biomimetic mineralization. *J Mater Chem* **17**, 415, 2007.
41. Glimcher, M.J. and Muir, H. Recent Studies of the Mineral Phase in Bone and Its Possible Linkage to the Organic Matrix by Protein-Bound Phosphate Bonds [and Discussion]. *Philos Trans R Soc Lond B Biol Sci* **304**, 479, 1984.
42. Fratzl, P., Fratzl-Zelman, N. and Klaushofer, K. Collagen packing and mineralization. An x-ray scattering investigation of turkey leg tendon. *Biophys J* **64**, 260, 1993.
43. Traub, W., Arad, T. and Weiner, S. Three-dimensional ordered distribution of crystals in turkey tendon collagen fibers. *Proc Natl Acad Sci USA* **86**, 9822, 1989.
44. Weiner, S. and Price, P.A. DISAGGREGATION OF BONE INTO CRYSTALS. *Calcif Tissue Int* **39**, 365, 1986.
45. Wachtel, E. and Weiner, S. Small - angle x - ray scattering study of dispersed crystals from bone and tendon. *J Bone Miner Res* **9**, 1651, 1994.
46. Beniash, E. Biominerals—hierarchical nanocomposites: the example of bone. *Wiley Interdisciplinary Reviews: Nanomedicine and Nanobiotechnology* **3**, 47, 2011.
47. Anderson, H.C. Molecular biology of matrix vesicles. *Clin Orthop* **314**, 266, 1995.
48. Anderson, H.C., Garimella, R. and Tague, S.E. The role of matrix vesicles in growth plate development and biomineralization. *Front Biosci* **10**, 822, 2005.
49. Ali, S.Y., Sajdera, S.W. and Anderson, H.C. Isolation and Characterization of Calcifying Matrix Vesicles from Epiphyseal Cartilage. *Proc Natl Acad Sci USA* **67**, 1513, 1970.
50. Miller, E.J. and Rhodes, R.K. [2] Preparation and characterization of the different types of collagen. *Methods Enzymol* **82**, 33, 1982.
51. Sodek, J., Ganss, B. and McKee, M. Osteopontin. *Crit Rev Oral Biol Med* **11**, 279, 2000.
52. Ganss, B., Kim, R.H. and Sodek, J. Bone sialoprotein. *Crit Rev Oral Biol Med* **10**, 79, 1999.
53. Hauschka, P.V., Lian, J.B., Cole, D.E. and Gundberg, C.M. Osteocalcin and matrix Gla protein: vitamin K-dependent proteins in bone. *Physiol Rev* **69**, 990, 1989.
54. Nudelman, F., Pieterse, K., George, A., Bomans, P.H.H., Friedrich, H., Brylka, L.J., Hilbers, P.A.J., de With, G. and Sommerdijk, N. The role of collagen in bone apatite formation in the presence of hydroxyapatite nucleation inhibitors. *Nat Mater* **9**, 1004, 2010.
55. Thula, T.T., Rodriguez, D.E., Lee, M.H., Pendi, L., Podschun, J. and Gower, L.B. In vitro mineralization of dense collagen substrates: A biomimetic approach toward the development of bone-graft materials. *Acta Biomater* **7**, 3158, 2011.
56. Nudelman, F., Bomans, P.H.H., George, A., De With, G. and Sommerdijk, N.A.J.M. The role of the amorphous phase on the biomimetic mineralization of collagen. *Faraday Discuss* **159**, 357, 2012.

57. Price, P.A., Toroian, D. and Lim, J.E. Mineralization by Inhibitor Exclusion: THE CALCIFICATION OF COLLAGEN WITH FETUIN. *J Biol Chem* **284**, 17092, 2009.
58. Wang, Y., Azaïs, T., Robin, M., Vallée, A., Catania, C., Legriel, P., Pehau-Arnaudet, G., Babonneau, F., Giraud-Guille, M.-M. and Nassif, N. The predominant role of collagen in the nucleation, growth, structure and orientation of bone apatite. *Nat Mater* **11**, 724, 2012.
59. Roveri, N., Falini, G., Sidoti, M.C., Tampieri, A., Landi, E., Sandri, M. and Parma, B. Biologically inspired growth of hydroxyapatite nanocrystals inside self-assembled collagen fibers. *Materials Science and Engineering C* **23**, 441, 2003.
60. Sprio, S., Sandri, M., Iafisco, M., Panseri, S., Adamiano, A., Montesi, M., Campodoni, E. and Tampieri, A. Bio-inspired assembling/mineralization process as a flexible approach to develop new smart scaffolds for the regeneration of complex anatomical regions. *J Eur Ceram Soc* **36**, 2857, 2016.
61. Kim, H.-W., Kim, H.-E. and Salih, V. Stimulation of osteoblast responses to biomimetic nanocomposites of gelatin–hydroxyapatite for tissue engineering scaffolds. *Biomaterials* **26**, 5221, 2005.
62. Leeuwenburgh, S.C.G., Jo, J., Wang, H., Yamamoto, M., Jansen, J.A. and Tabata, Y. Mineralization, Biodegradation, and Drug Release Behavior of Gelatin/Apatite Composite Microspheres for Bone Regeneration. *Biomacromolecules* **11**, 2653, 2010.
63. Landi, E., Valentini, F. and Tampieri, A. Porous hydroxyapatite/gelatine scaffolds with ice-designed channel-like porosity for biomedical applications. *Acta Biomater* **4**, 1620, 2008.
64. Wang, H., Bongio, M., Farbod, K., Nijhuis, A.W., van den Beucken, J., Boerman, O.C., van Hest, J.C., Li, Y., Jansen, J.A. and Leeuwenburgh, S.C. Development of injectable organic/inorganic colloidal composite gels made of self-assembling gelatin nanospheres and calcium phosphate nanocrystals. *Acta Biomater* **10**, 508, 2014.
65. Chesnutt, B.M., Viano, A.M., Yuan, Y., Yang, Y., Guda, T., Appleford, M.R., Ong, J.L., Haggard, W.O. and Bumgardner, J.D. Design and characterization of a novel chitosan/nanocrystalline calcium phosphate composite scaffold for bone regeneration. *J Biomed Mater Res A* **88**, 491, 2009.
66. Yan, L.-P., Silva-Correia, J., Correia, C., Caridade, S.G., Fernandes, E.M., Sousa, R.A., Mano, J.F., Oliveira, J.M., Oliveira, A.L. and Reis, R.L. Bioactive macro/micro porous silk fibroin/nano-sized calcium phosphate scaffolds with potential for bone-tissue-engineering applications. *Nanomedicine* **8**, 359, 2013.
67. Dhandayuthapani, B., Yoshida, Y., Maekawa, T. and Kumar, D.S. Polymeric scaffolds in tissue engineering application: a review. *International Journal of Polymer Science* **2011**2011.
68. Rezwani, K., Chen, Q., Blaker, J. and Boccaccini, A.R. Biodegradable and bioactive porous polymer/inorganic composite scaffolds for bone tissue engineering. *Biomaterials* **27**, 3413, 2006.
69. Bareiro, O. and Santos, L. Tetraethylorthosilicate (TEOS) applied in the surface modification of hydroxyapatite to develop polydimethylsiloxane/hydroxyapatite composites. *Colloids Surf B* **115**, 400, 2014.
70. Arabmotlagh, M., Bachmaier, S., Geiger, F. and Rauschmann, M. PMMA - hydroxyapatite composite material retards fatigue failure of augmented bone

- compared to augmentation with plain PMMA: In vivo study using a sheep model. *J Biomed Mater Res B* **102**, 1613, 2014.
71. Lukaszczyk, J., Janicki, B., López, A., Skolucka, K., Wojdyla, H., Persson, C., Piaskowski, S. and Smiga-Matuszowicz, M. Novel injectable biomaterials for bone augmentation based on isosorbide dimethacrylic monomers. *Mater Sci Eng C* **40**, 76, 2014.
 72. Hild, N., Fuhrer, R., Mohn, D., Bubenhofer, S.B., Grass, R.N., Luechinger, N.A., Feldman, K., Dora, C. and Stark, W.J. Nanocomposites of high-density polyethylene with amorphous calcium phosphate: in vitro biomineralization and cytocompatibility of human mesenchymal stem cells. *Biomedical Materials* **7**, 054103, 2012.
 73. Liao, C.Z., Wong, H.M., Yeung, K.W.K. and Tjong, S.C. The development, fabrication, and material characterization of polypropylene composites reinforced with carbon nanofiber and hydroxyapatite nanorod hybrid fillers. *Int J Nanomedicine* **9**, 1299, 2014.
 74. Nie, L., Chen, D., Suo, J., Zou, P., Feng, S., Yang, Q., Yang, S. and Ye, S. Physicochemical characterization and biocompatibility in vitro of biphasic calcium phosphate/polyvinyl alcohol scaffolds prepared by freeze-drying method for bone tissue engineering applications. *Colloids Surf B* **100**, 169, 2012.
 75. Zhang, R. and Ma, P.X. Porous poly (L-lactic acid)/apatite composites created by biomimetic process. *J Biomed Mater Res* **45**, 285, 1999.
 76. Murphy, W.L., Kohn, D.H. and Mooney, D.J. Growth of continuous bonelike mineral within porous poly (lactide-co-glycolide) scaffolds in vitro. *J Biomed Mater Res* **50**, 50, 2000.
 77. Kim, M.-J. and Koh, Y.-H. Synthesis of aligned porous poly (ϵ -caprolactone)(PCL)/hydroxyapatite (HA) composite microspheres. *Mater Sci Eng C* **33**, 2266, 2013.
 78. Fu, S., Yang, L., Fan, J., Wen, Q., Lin, S., Wang, B., Chen, L., Meng, X., Chen, Y. and Wu, J. In vitro mineralization of hydroxyapatite on electrospun poly (ϵ -caprolactone)-poly (ethylene glycol)-poly (ϵ -caprolactone) fibrous scaffolds for tissue engineering application. *Colloids Surf B* **107**, 167, 2013.
 79. Rodriguez, I.A., Madurantakam, P.A., McCool, J.M., Sell, S.A., Yang, H., Moon, P.C. and Bowlin, G.L. Mineralization potential of electrospun PDO-hydroxyapatite-fibrinogen blended scaffolds. *International journal of biomaterials* **2012**2012.
 80. van Leeuwen, A.C., Bos, R.R. and Grijpma, D.W. Composite materials based on poly (trimethylene carbonate) and β - tricalcium phosphate for orbital floor and wall reconstruction. *J Biomed Mater Res B* **100**, 1610, 2012.
 81. Pérez, C.M.R., Stephanopoulos, N., Sur, S., Lee, S.S., Newcomb, C. and Stupp, S.I. The Powerful Functions of Peptide-Based Bioactive Matrices for Regenerative Medicine. *Ann Biomed Eng* **43**, 501, 2015.
 82. Galler, K.M., Cavender, A., Yuwono, V., Dong, H., Shi, S., Schmalz, G., Hartgerink, J.D. and D'Souza, R.N. Self-assembling peptide amphiphile nanofibers as a scaffold for dental stem cells. *Tissue Engineering Part A* **14**, 2051, 2008.
 83. Rexeisen, E.L., Fan, W., Pangburn, T.O., Taribagil, R.R., Bates, F.S., Lodge, T.P., Tsapatsis, M. and Kokkoli, E. Self-assembly of fibronectin mimetic peptide-amphiphile nanofibers. *Langmuir* **26**, 1953, 2009.

84. Jin, H.-E., Jang, J., Chung, J., Lee, H.J., Wang, E., Lee, S.-W. and Chung, W.-J. Biomimetic Self-Templated Hierarchical Structures of Collagen-Like Peptide Amphiphiles. *Nano Lett* **15**, 7138, 2015.
85. Hartgerink, J.D., Beniash, E. and Stupp, S.I. Self-assembly and mineralization of peptide-amphiphile nanofibers. *Science* **294**, 1684, 2001.
86. Sargeant, T.D., Aparicio, C., Goldberger, J.E., Cui, H. and Stupp, S.I. Mineralization of peptide amphiphile nanofibers and its effect on the differentiation of human mesenchymal stem cells. *Acta Biomater* **8**, 2456, 2012.
87. Olsen, D., Yang, C., Bodo, M., Chang, R., Leigh, S., Baez, J., Carmichael, D., Perälä, M., Hämäläinen, E.-R., Jarvinen, M. and Polarek, J. Recombinant collagen and gelatin for drug delivery. *Adv Drug Delivery Rev* **55**, 1547, 2003.
88. Cappello, J., Ferrari, F. and Mobley, D. *Plastics from microbes*. Hanser/Gardner, Cincinnati, OH, 35, 1994.
89. Goldberg, I., Salerno, A.J., Patterson, T. and Williams, J.I. Cloning and expression of a collagen-analog-encoding synthetic gene in *Escherichia coli*. *Gene* **80**, 305, 1989.
90. Yu, H.S., Jang, J.H., Kim, T.I., Lee, H.H. and Kim, H.W. Apatite - mineralized polycaprolactone nanofibrous web as a bone tissue regeneration substrate. *J Biomed Mater Res A* **88**, 747, 2009.
91. Barrere, F., Snel, M.M.E., van Blitterswijk, C.A., de Groot, K. and Layrolle, P. Nano-scale study of the nucleation and growth of calcium phosphate coating on titanium implants. *Biomaterials* **25**, 2901, 2004.
92. Brown, A., Zaky, S., Ray Jr, H. and Sfeir, C. Porous magnesium/PLGA composite scaffolds for enhanced bone regeneration following tooth extraction. *Acta Biomater* **11**, 543, 2015.
93. Ruoslahti, E. RGD and other recognition sequences for integrins. *Annu Rev Cell Dev Biol* **12**, 697, 1996.
94. Tuin, A., Kluijtmans, S.G., Bouwstra, J.B., Harmsen, M.C. and Van Luyn, M.J. Recombinant gelatin microspheres: novel formulations for tissue repair? *Tissue Engineering Part A* **16**, 1811, 2010.
95. Parvizi, M., Plantinga, J.A., van Speuwel - Goossens, C.A., van Dongen, E.M., Kluijtmans, S.G. and Harmsen, M.C. Development of recombinant collagen - peptide - based vehicles for delivery of adipose - derived stromal cells. *J Biomed Mater Res A* **104**, 503, 2016.
96. Mumcuoglu, D., de Miguel, L., Nickel, J., Van Leeuwen, J.P., Van Osch, G.J. and Kluijtmans, S.G. BMP-2 release from synthetic collagen peptide particles. *Frontiers in Bioengineering and Biotechnology*.
97. Zhai, Y., Cui, F.Z. and Wang, Y. Formation of nano-hydroxyapatite on recombinant human-like collagen fibrils. *Curr Appl Phys* **5**, 429, 2005.
98. Zhai, Y. and Cui, F. Recombinant human-like collagen directed growth of hydroxyapatite nanocrystals. *J Cryst Growth* **291**, 202, 2006.
99. Wang, Y., Cui, F., Zhai, Y., Wang, X., Kong, X. and Fan, D. Investigations of the initial stage of recombinant human-like collagen mineralization. *Mater Sci Eng C* **26**, 635, 2006.
100. Wang, Y., Cui, F., Hu, K., Zhu, X. and Fan, D. Bone regeneration by using scaffold based on mineralized recombinant collagen. *J Biomed Mater Res B* **86**, 29, 2008.
101. Wu, B., Zheng, Q., Guo, X., Wu, Y., Wang, Y. and Cui, F. Preparation and ectopic osteogenesis in vivo of scaffold based on mineralized recombinant

- human-like collagen loaded with synthetic BMP-2-derived peptide. *Biomedical Materials* **3**, 044111, 2008.
102. Langer, R. and Tirrell, D.A. Designing materials for biology and medicine. *Nature* **428**, 487, 2004.
 103. Bergsma, E.J., Rozema, F.R., Bos, R.R. and De Bruijn, W.C. Foreign body reactions to resorbable poly (L-lactide) bone plates and screws used for the fixation of unstable zygomatic fractures. *J Oral Maxillofac Surg* **51**, 666, 1993.
 104. Srinivasan, S., Jayasree, R., Chennazhi, K., Nair, S. and Jayakumar, R. Biocompatible alginate/nano bioactive glass ceramic composite scaffolds for periodontal tissue regeneration. *Carbohydr Polym* **87**, 274, 2012.
 105. Peter, M., Binulal, N., Nair, S., Selvamurugan, N., Tamura, H. and Jayakumar, R. Novel biodegradable chitosan–gelatin/nano-bioactive glass ceramic composite scaffolds for alveolar bone tissue engineering. *Chem Eng J* **158**, 353, 2010.
 106. Shikinami, Y., Matsusue, Y. and Nakamura, T. The complete process of bioresorption and bone replacement using devices made of forged composites of raw hydroxyapatite particles/poly l-lactide (Fu-HA/PLLA). *Biomaterials* **26**, 5542, 2005.
 107. Panzavolta, S., Gioffrè, M., Focarete, M.L., Gualandi, C., Foroni, L. and Bigi, A. Electrospun gelatin nanofibers: optimization of genipin cross-linking to preserve fiber morphology after exposure to water. *Acta Biomater* **7**, 1702, 2011.
 108. Bigi, A., Cojazzi, G., Panzavolta, S., Roveri, N. and Rubini, K. Stabilization of gelatin films by crosslinking with genipin. *Biomaterials* **23**, 4827, 2002.
 109. Wang, Y., Yang, C., Chen, X. and Zhao, N. Development and Characterization of Novel Biomimetic Composite Scaffolds Based on Bioglass - Collagen - Hyaluronic Acid - Phosphatidylserine for Tissue Engineering Applications. *Macromol Mater Eng* **291**, 254, 2006.
 110. Kuijpers, A.J., Engbers, G.H., Krijgsveld, J., Zaat, S.A., Dankert, J. and Feijen, J. Cross-linking and characterisation of gelatin matrices for biomedical applications. *J Biomater Sci, Polym Ed* **11**, 225, 2000.
 111. Hutmacher, D.W., Schantz, J.T., Lam, C.X.F., Tan, K.C. and Lim, T.C. State of the art and future directions of scaffold - based bone engineering from a biomaterials perspective. *J Tissue Eng Regen Med* **1**, 245, 2007.
 112. Haugh, M.G., Murphy, C.M., McKiernan, R.C., Altenbuchner, C. and O'Brien, F.J. Crosslinking and mechanical properties significantly influence cell attachment, proliferation, and migration within collagen glycosaminoglycan scaffolds. *Tissue Engineering Part A* **17**, 1201, 2011.
 113. Haugh, M.G., Jaasma, M.J. and O'Brien, F.J. The effect of dehydrothermal treatment on the mechanical and structural properties of collagen-GAG scaffolds. *J Biomed Mater Res A* **89A**, 363, 2009.
 114. Zhang, L. and Webster, T.J. Nanotechnology and nanomaterials: Promises for improved tissue regeneration. *Nano Today* **4**, 66, 2009.
 115. Bosco, R., Iafisco, M., Tampieri, A., Jansen, J.A., Leeuwenburgh, S.C. and Van Den Beucken, J.J. Hydroxyapatite nanocrystals functionalized with alendronate as bioactive components for bone implant coatings to decrease osteoclastic activity. *Appl Surf Sci* **328**, 516, 2015.
 116. Roy, T.D., Simon, J.L., Ricci, J.L., Rekow, E.D., Thompson, V.P. and Parsons, J.R. Performance of degradable composite bone repair products made via

- three - dimensional fabrication techniques. *J Biomed Mater Res A* **66**, 283, 2003.
117. Hutmacher, D. and Cool, S. Concepts of scaffold - based tissue engineering—the rationale to use solid free - form fabrication techniques. *J Cell Mol Med* **11**, 654, 2007.
 118. Mikos, A.G., Sarakinos, G., Leite, S.M., Vacant, J.P. and Langer, R. Laminated three-dimensional biodegradable foams for use in tissue engineering. *Biomaterials* **14**, 323, 1993.
 119. Klawitter, J. and Hulbert, S. Application of porous ceramics for the attachment of load bearing internal orthopedic applications. *J Biomed Mater Res* **5**, 161, 1971.
 120. Yang, S., Leong, K.-F., Du, Z. and Chua, C.-K. The design of scaffolds for use in tissue engineering. Part I. Traditional factors. *Tissue Eng* **7**, 679, 2001.
 121. Mitsak, A.G., Kemppainen, J.M., Harris, M.T. and Hollister, S.J. Effect of polycaprolactone scaffold permeability on bone regeneration in vivo. *Tissue Engineering Part A* **17**, 1831, 2011.
 122. Albrektsson, T. and Johansson, C. Osteoinduction, osteoconduction and osseointegration. *Eur Spine J* **10**, S96, 2001.

Chapter 2: General Experimental Methods and Techniques

2.1. Materials

Recombinant collagen peptide (RCP) is commercialized by Fujifilm Manufacturing Europe B.V. under the tradename Cellnest™. It is defined as a recombinant peptide based on human type I collagen (α_1 chain). It has a molecular weight of approximately 51 kDa and an isoelectric point of 10.

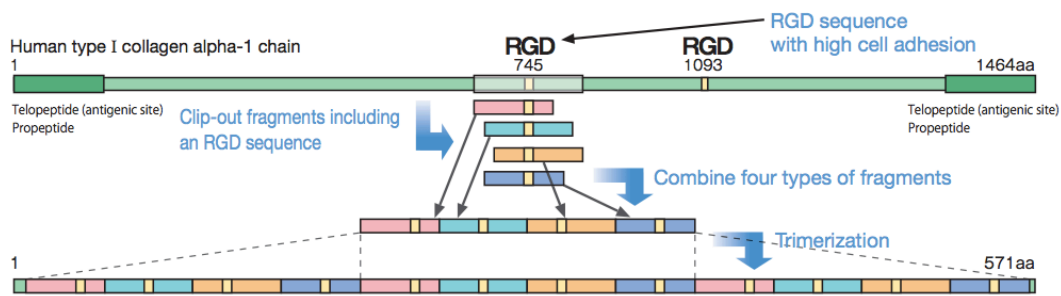


Figure 1. Recombinant collagen peptide (RCP) amino acid sequence is based on human collagen type I.

Phosphoric acid (H_3PO_4 , purity ≥ 85 wt.%), calcium hydroxide ($\text{Ca}(\text{OH})_2$, purity $\geq 95\%$) and magnesium chloride hexahydrate ($\text{MgCl}_2 \cdot 6\text{H}_2\text{O}$, $\geq 99\%$ purity) were purchased from Sigma Aldrich. The solutions were prepared with ultrapure water ($0.22 \mu\text{S}$, 25°C , MilliQ®, Millipore). Genipin was purchased from Wako Pure Chemical USA (purity 98% HPLC).

2.2. Characterization techniques

➤ **X-Ray Diffraction (XRD)** spectra were obtained by using a Cu $K\alpha$ radiation at a wavelength of 1.5418 \AA on a PANalytical X'Pert PRO diffractometer equipped with a PIXcel detector operating at 40 mA and 45 kV. The XRD spectra were acquired in the 2θ range 4° - 100° , with a step size of 0.013° and scan time of 1900 s. The average crystallite size along the apatite axis directions [002] and [310] was calculated by applying the Scherrer equation:

$$t = (K\lambda) / (\beta_{1/2} \cos \theta) \quad (1)$$

where t is the average of crystallite size in \AA , K is the shape factor (fixed at 0.9 for spherical crystallites), λ is the wavelength of Cu $K\alpha$ radiation (1.5418 \AA) and $\beta_{1/2}$ is the full width at half-maximum intensity.

Chapter 2: General Experimental Methods and Techniques

➤ **Fourier transform infrared (FTIR) spectra** of synthesized samples were collected by Nicolet 380 FTIR spectrometer (Thermo Fisher Scientific, Waltham, MA). 5 mg of sample was mixed with ~250 mg of anhydrous potassium bromide (KBr). The mixture was pressed at 10 tons pressure into 7 mm diameter disc. A pure KBr disk was used as background. The spectra were registered from 4000 cm^{-1} to 400 cm^{-1} with a resolution of 2 cm^{-1} .

➤ **Raman spectra** were collected with a LabRAM-HR spectrometer with backscattering geometry (Jobin-Yvon, Horiba, Japan). The excitation line was provided by a diode laser emitting at a wavelength of 532 nm and a Peltier cooled charge-couple device (CCD) (1064x256 pixels) was used as detector. Spectrometer resolution is higher than 3 cm^{-1} . The final spectrum resulted by the average of 3 acquisitions (acquisition time= 300 s). Curve fitting, using Lorentzian functions, and quantification of integral areas was done using MagicPlotPro (2.5.1) software.

➤ **Transmission Electron Microscopy (TEM)** evaluation was performed with FEI Tecnai F20 microscope operating at 120 kV. Samples were prepared directly from the solution after 2 hours of mineralization. 10 μL aliquot was diluted 1:1000 in ultrapure water and sonicated for 15 min. Diluted samples were deposited on 200 mesh copper TEM grids covered with thin amorphous carbon films and incubated for several minutes. After that, the grids were rinsed with ultrapure water, being then the water excess manually blotted.

➤ **Inductively-coupled plasma optical emission spectrometry (ICP-OES, Agilent Technologies 5100)** was employed to analyse the chemical composition of synthesized samples (Ca, P, Mg). For this analysis, 20 mg of sample were dissolved in 2 ml of ultrapure nitric acid and then diluted up to 100 mL. Diluted solutions were analysed for analytical emission wavelengths: Ca (422 nm), Mg (279 nm) and P (214 nm).

➤ **Thermogravimetry analysis (TGA)** of the designed matrices was carried out in a simultaneous thermal analyzer (STA 449 Jupiter Netzsch Geratebau). About 10 mg of sample were weighted in a platinum crucible and heated from room temperature to 1000 $^{\circ}\text{C}$ under airflow with a heating rate of 10 $^{\circ}\text{C}/\text{min}$.

➤ **Brunauer-Emmett-Teller (BET)** gas adsorption method (Sorpty 1750, Carlo Erba, Milan Italy) was used to measure the specific surface area (SSA) of powdered samples.

➤ **Scanning electron microscopy (ESEM FEI Quanta 200, Oregon, USA)** was used to analyse mineral distribution and the pore size of scaffold prototype, the hybrid matrices and 3D scaffolds. Samples were fixed on aluminium stubs using a carbon tape and sputter with a 20 nm thick gold layer. SEM images were acquired at 10 KeV at high vacuum.

2.3. Characterization of the physic-chemical properties of designed scaffolds

2.3.1. Porosity and pore size

Total porosity was measured by gravimetry according to the following equation:

$$Porosity (\%) = 100 \cdot \left(1 - \frac{\rho_{scaffold}}{\rho_{material}}\right) \quad (2)$$

,where $\rho_{material}$ is the density of the material of which the scaffold is fabricated and $\rho_{scaffold}$ is the apparent density of the scaffold measured by dividing the weight by the volume of the scaffold.¹ Density of RCP is consider 1.3 g/cm³ according to technical specification and apatite density is consider 3.16 g/cm³ according to the literature.²

The mean pore size of RCP, Ap/RCP and MgAp/RCP scaffolds was obtained by measuring 60 pores from SEM micrographs with Image J software (version 1.48v, NIH, Bethesda, Maryland).

2.3.2. Permeability

The scaffold permeability was evaluated by falling head method. It consists in measuring the time that a fluid column drop from the upper (H_1) to the lower level (H_2) of a standpipe while fluid flows through the scaffold, which is hosted to a permeability chamber that directly connects to the standpipe. Five scaffolds per condition were autoclaved in phosphate buffered saline (PBS) and maintained in PBS solution overnight (37 °C) before the measurements. The scaffold permeability constant was calculated according to Darcy's law:³

$$k = \frac{a L}{A t} \frac{\mu}{\rho g} \ln \frac{H_1}{H_2} \quad (3)$$

Where: k , scaffold permeability (m^2); a , cross-sectional area of standpipe (mm^2) $a = \pi r_p^2$; A , cross-sectional area of scaffold (mm^2) $A = \pi r_s^2$; L , scaffold thickness (m); t , time for PBS going from H_1 to H_2 (s); H_1 , H_2 , height of PBS column (cm); μ , dynamic viscosity of fluid (Nsm^{-2}); ρ , density of fluid (kg/m^3) and g gravity (m/s^2).

2.3.3. Interfacial properties: Surface roughness and wettability

Atomic Force Microscopy (AFM) images were acquired with a Multimode-Nanoscope 3D (Digital Instruments, Bruker Nanosurface division, USA), equipped with an E scanner, using SNL-10 probes (Bruker AFM Probes) with $250 \mu m$ of length and $40 \mu m$ of width (with 23 kHz nominal resonant frequency and 0.12 N/m nominal spring constant). Imaging was performed in air condition and contact mode. Surface roughness has been characterized in terms of root mean square (RMS) roughness (R_q) that belongs to the average between the height deviations (Z) and the mean/line surface, taken over the evaluation length/area:

$$R_q = \frac{1}{n} \sum_{i=1}^n (Z_i - \bar{Z})^2 \quad (4)$$

The scan length and the resolution of the measurement were kept constant in order to decrease the influence of the scanning parameters on roughness value. The roughness was calculated for two scan areas of $2.5 \times 2.5 \mu m^2$ and $5 \times 5 \mu m^2$ with a fixed resolution of 512×512 points.

Wettability of designed matrices was evaluated by measuring contact angle in an optical tensiometer equipped with a CCD camera (OCA 15 Plus, DataPhysic Instruments). Measurements were carried out in static condition with the sessile drop method (drop volume of $1 \mu l$ of water).

2.3.4. Swelling capacity

Swelling capacity of the scaffolds was evaluated by introduction of scaffolds into phosphate buffered solution (PBS, pH 7.4) at $37 \text{ }^\circ C$ with gentle shaking. After 24 hours, scaffolds were removed, wiped with filter paper to remove excess of liquid and weight (W_w). Swelling capacity was determined according to next equation:

$$Swelling (\%) = 100 \frac{W_w - W_d}{W_d} \quad (5)$$

, where W_d is the initial dry weight of scaffolds before immersion into PBS.

2.3.5. Determination of extent of crosslinking

TNBS assay was used to determine the primary amine content in recombinant collagen peptide and quantify the crosslinking degree of processed recombinant collagen scaffolds. Through this protocol, the content of amino groups can be identified by labelling with 2,4,6-trinitrobenzenesulfonic acid (TNBS). Both crosslinked (C) and non-crosslinked (NC) scaffolds were immersed in 2 mL of solution containing 1 ml of sodium bicarbonate solution (4% w/v) and 1 mL TNBS solution (0.5 %) and incubated at 37 °C for 3 hours in a water bath with shaking. After that, 3 mL of hydrochloric acid (pure) was added to mask the unreacted TNBS. The volume was raised to 10 mL and the solution was kept for 15 hours in a water bath at 37 °C. The absorbance of the diluted solutions was measured at 345 nm using UV-vis Spectrophotometer and crosslinking degree was calculated by the following equation:

$$\text{Crosslinking degree}(\%) = 100 \cdot \left(\frac{\text{Abs}_{NC} - \text{Abs}_C}{\text{Abs}_{NC}} \right) \quad (6)$$

2.3.6. *In vitro* scaffold degradation

The physiological stability and degradability of the scaffolds were evaluated by measuring the degradation rate as well as the ion release to the media. Briefly, three scaffolds (30 mg) per group and time point were immersed in 10 mL of PBS solution (pH 7.4) at 37 °C over the course of 4 weeks. At scheduled time points (7, 14, 21 and 28 days), scaffolds were removed from the liquid, rinsed with Milli-Q water and dried into oven at 40 °C overnight. The percentage of the weight loss was calculated as follows:

$$\text{Weight Loss} (\%) = 100 \cdot (W_i - W_f) / W_i \quad (7)$$

where W_i is the starting dry weight and W_f is the dry weight at time t .

At each time point, PBS was collected and refresh with new one. The media samples were filtered, treated with nitric acid and diluted in Milli-Q water for evaluation of element concentration (Ca and Mg) by ICP-OES.

2.3.7. Enzymatic degradation

Crosslinked scaffolds (RCP, Ap/RCP and MgAP/RCP) were weighted (~5mg), immersed in 1 mL of 0.1 M Tris-HCl (pH 7.4) containing 25 CDU/mL of collagenase (Collagenase from *Clostridium histolyticum*, ≥ 125 CDU/mg solid, Sigma Aldrich) and 5

mM CaCl₂ and incubated for 24 hours at 37 °C. After 24 hours, the reaction was stopped. The extent of scaffold degradation was determined by measuring the weight loss of the scaffolds (previously described) and the protein release to the supernatant was quantified by a colorimetric assay (Kit DC Protein Assay, Bio-Rad). Three scaffolds per condition were analysed.

2.4. *In vitro* test

2.4.1. Cell viability and proliferation

Cell viability was qualitatively assessed with live/dead assay kit (Invitrogen) according to manufacturer's instructions. This assay is based on the simultaneous determination of live and dead cells with two probes, Calcein acetoxymethyl (Calcein AM) and Ethidium homodimer-1 (EthD-1), measuring recognized parameters of cell viability, intracellular esterase activity and plasma membrane integrity respectively. One sample per group was analysed.

Cell viability and proliferation were also quantitatively assessed using MTT assay. Briefly, cell/scaffold constructs were incubated with 150 µL of MTT solution (3-(4,5-dimethylthiazol-2-yl)-2,5-diphenyltetrazolium bromide) for 2 h at 37 °C. In this assay, the metabolically active cells react with the tetrazolium salt in the MTT reagent to produce a formazan dye. Then, scaffolds were transferred to a tube containing 1 mL of dimethyl sulfoxide (DMSO) that dissolved formazan crystals. 200 µL of supernatant was transferred to 96-well plate and the absorbance was read at 570 nm using a Multiskan FC Microplate Photometer (Thermo Scientific). Three samples per group were analysed at each time point. This absorbance is directly proportional to the number of metabolically active cells.

2.4.2. Cell morphology

Cell adhesion and morphology was assessed by SEM observations. The samples were washed with 0.1 M sodium cacodylate buffer, fixed in 2.5% glutaraldehyde in 0.1 M sodium cacodylate buffer for 2 h at 4 °C, washed again in 0.1 M sodium cacodylate buffer and then freeze-dried. Samples were fixed on aluminium stubs using a carbon tape, sputtered with a 20 nm thick gold layer and analysed using SEM (ESEM FEI Quanta 200).

2.4.3. Cell migration

Two samples per condition were collected and fixed in 4% (w/v) paraformaldehyde (PFA). After cell permeabilization with 0.1 % (v/v) Triton X-100, samples were incubated with DAPI 300 nM (Invitrogen) for 7 min and washed with PBS. Scaffolds were cut longitudinally and cell migration from top to the bottom of the scaffold was analysed with an Inverted Ti-E fluorescence microscope (Nikon). The number of cells in the upper surface (external part) and in three different inner areas (top, middle and bottom) was quantified with ImageJ software for each scaffold composition.

2.4.4. Quantitative real-time polymerase chain reaction (qPCR)

The gene expression profile of mesenchymal stem cells (MSCs) cultured on the three different scaffold compositions was assessed using a real time-quantitative polymerase chain reaction (qPCR). The RCP scaffold was used as a calibrator in order to obtain a relative quantification. After scheduled times of cell culture, total RNA was harvested using Tri Reagent, followed by the Direct-zol RNA MiniPrep kit (Zymo Research) according to manufacturer's instructions. RNA integrity was analysed by native agarose gel electrophoresis and its quantification was performed by the Qubit® 2.0 Fluorimeter together with the Qubit® RNA BR assay kit, following manufacturer's instructions (Invitrogen). Total RNA (500 ng) was reverse transcribed to cDNA using the High-Capacity cDNA Reverse Transcription Kit, according to manufacturer's instructions (Applied Biosystems). Relative quantification of the gene expression was performed by StepOne™ Real-Time PCR System (Applied Biosystems). The genes under studied were: alkaline phosphatase (ALP), collagen I (ColI), osteopontin (OPN), osterix (OSX), runt-related transcription factor 2 (RUNX2), bone sialoprotein (BSP), secreted protein acidic and rich in cysteine (SPARC) known as osteonectin, bone gamma-carboxyglutamic acid-containing protein (BGLAP) known as osteocalcin, vascular endothelial growth factor (VEGF), transforming growth factor (TGF-β), bone morphogenetic protein (BMP-2) and glyceraldehydes-3-phosphate dehydrogenase (GAPDH), used as housekeeping gene,

Data were collected using the OneStep Software (v.2.2.2) and relative quantification was performed using the comparative threshold (C_T) method ($\Delta\Delta C_T$) where relative gene expression level equals $2^{-\Delta\Delta C_T}$. Three scaffolds per group were analysed in three

technical replicates; error bars reflect one standard error of the mean of 3 technical replicates as described elsewhere.^{4,5}

2.4.5. Western Blot Analysis

After 14 and 28 days the cells were lysed in a Radioimmunoprecipitation buffer (RIPA buffer) supplemented with a proteinase inhibitor cocktail (Cell Signaling). Protein concentration in each cell lysate supernatant was determined by a colorimetric assay (Kit DC Protein Assay, Bio-Rad). The protein samples were diluted in sample buffer (3:1), and loaded and separated in a 4–20% Mini-PROTEAN TGX stain-free protein gels (BioRad), using a Mini-PROTEAN electrophoresis cell kit (Bio-Rad).

The proteins were then transferred to nitrocellulose membranes by means of a Trans-Blot Turbo™ transfer system (BioRad), with the blots incubated thereafter for 30 min at room temperature in a blocking solution of 5% non-fat dry milk in PBS. The membranes were incubated overnight at 4 °C with primary rabbit antibody anti- β -catenin (Abcam) and anti- β -actin (Cell Signaling) as internal control, and then incubated with a horseradish goat peroxidase-linked secondary antibody anti-rabbit (Bio-Rad) for 30 min. An enhanced chemiluminescence kit (ECL, BioRad) was used to visualize the protein bands with ChemiDoc XRS+ (Bio-Rad). In order to evaluate the relative protein expression, the β -catenin band intensities were quantified by densitometry using ImageLab Software and were then normalized over the signal of the corresponding bands of β -actin (loading control).

2.4.6. Immunofluorescence

Osteogenic related markers were also analysed by immunofluorescence through the staining of runt-related transcription factor 2 (RUNX2). After 14 days of cell culture, cells seeded on the samples were fixed in 4% (w/v) PFA. Blocking was performed with bovine serum albumin (1% BSA) and 10 % normal goat serum (NGS). Then, cells were permeabilized with 0.1% Tryton X-100 for 20 min with slow agitation. Samples were incubated overnight at 4 °C, with antibodies anti-RUNX2 (Abcam). Primary antibodies were probed with the secondary antibodies Cy3 sheep anti-mouse (Molecular Probes), for 45 min at room temperature. Cell nuclei were stained with DAPI 300 nM for 10 min. Images of one sample per group were acquired by an Inverted Ti-E fluorescence microscope (Nikon).

2.5. Statistical analysis

Results are expressed as the mean \pm standard error of the mean (SEM). Data analysis was made by two-way analysis of variance (ANOVA), followed by Bonferroni's post hoc test. Statistical analyses were performed by the GraphPad Prism software (version 6.0), with statistical significance set at $p < 0.05$.

References

1. Karageorgiou, V. and Kaplan, D. Porosity of 3D biomaterial scaffolds and osteogenesis. *Biomaterials* **26**, 5474, 2005.
2. Porter, A., Patel, N., Brooks, R., Best, S., Rushton, N. and Bonfield, W. Effect of carbonate substitution on the ultrastructural characteristics of hydroxyapatite implants. *J Mater Sci Mater Med* **16**, 899, 2005.
3. Pennella, F., Cerino, G., Massai, D., Gallo, D., Labate, G.F.D.U., Schiavi, A., Deriu, M.A., Audenino, A. and Morbiducci, U. A survey of methods for the evaluation of tissue engineering scaffold permeability. *Ann Biomed Eng* **41**, 2027, 2013.
4. Ivey, K.N., Muth, A., Arnold, J., King, F.W., Yeh, R.-F., Fish, J.E., Hsiao, E.C., Schwartz, R.J., Conklin, B.R., Bernstein, H.S. and Srivastava, D. MicroRNA Regulation of Cell Lineages in Mouse and Human Embryonic Stem Cells. *Cell Stem Cell* **2**, 219, 2008.
5. Liu, H., Peng, H., Wu, Y., Zhang, C., Cai, Y., Xu, G., Li, Q., Chen, X., Ji, J., Zhang, Y. and OuYang, H.W. The promotion of bone regeneration by nanofibrous hydroxyapatite/chitosan scaffolds by effects on integrin-BMP/Smad signaling pathway in BMSCs. *Biomaterials* **34**, 4404, 2013.

Chapter 3: Understanding biomineralization of recombinant collagen peptide in the presence of magnesium

3.1. Introduction

Biomineralization is the process by which living organisms create composite materials of amazing complexity for a variety of purposes, including mechanical support, navigation, and protection against predation.¹ The study of biomineralization process has attracted the attention of scientists as a source of inspiration to achieve advanced materials with complex shape, hierarchical organization and well-defined size, morphology and structure.

Bone is a highly complex mineralized tissue whose building blocks are made of a collagen matrix reinforced by the intra- and interfibrillar mineralization of apatite (Ap) nanocrystals.² The biomineralization process through which organic macromolecules control the formation mechanisms and the crystallization pathways of Ap is still far from being fully comprehended. In the last years, it was unequivocally demonstrated that Ap formation in biological tissue does not occur directly by the association of ions from solution according to the classical nucleation theory, but proceeds through a “non-classical” crystallization pathway via an amorphous calcium phosphate (ACP, $\text{Ca}_3(\text{PO}_4)_2 \cdot \text{H}_2\text{O}$) precursor phase.³⁻⁵ It has been suggested that non-collagenous proteins (NCPs) act as a process-directing agent in bone mineralization.² Many of NCPs (i.e., osteonectin and various phosphoproteins such as osteopontin, osteocalcin, phosphophoryn and bone sialoprotein) are rich in carboxylate groups coming from aspartic and glutamic acid residues which can bind calcium ions present in solutions controlling the Ap crystallization mechanism.² Inspired by this biologically controlled mineral formation, syntheses of bone-like Ap have been carried out in the presence of several amino acids,⁶⁻⁸ biological macromolecules such as carboxylate-rich proteins⁹ and small organic molecules containing carboxylate groups such as citrate.¹⁰⁻¹² Concretely, citrate has been proposed to play a dual role in controlling apatite formation mechanism: driving a growth pathway via an amorphous precursor^{10,11} and controlling the size of nanocrystals by the non-classical oriented aggregation mechanism.¹² Furthermore, *in vitro* collagen mineralization in presence of polyaspartic acid (pAsp)

has shown that pAsp inhibits Ap nucleation in soluble form while promotes nucleation when attached to a substrate as collagen fibres.^{2,13}

Bio-inspired natural collagen mineralization approaches mimicking *in vivo* biomineralization have been explored for the development of advanced materials for bone regeneration,¹⁴ exhibiting complex shape, hierarchical organization and controlled size, under body-like conditions in aqueous environments. The process enabled the activation of the various control mechanisms that drive the assembling, 3D organization and mineralization of collagen fibrils thus generating hybrid fibrous scaffolds with high mimicry of the compositional and morphological features of those of newly formed bone tissue.^{15,16} Nevertheless, the use of natural collagen derived from animal tissues may present some limitations such as: the quality and the purity that influence collagen performance, the possibility of immunological reactions in susceptible patients due to their non-human protein composition or even the possible contamination with pathogenic substances.¹⁷ Therefore, many approaches such as mammalian and insect cells or biotechnological yeast process have been engineered to express high level of recombinant collagen type I derived proteins with high reproducible quality, leading to a reliable performance. Several authors have studied the biomimetic mineralization of recombinant human like collagen as potential biomaterial for bone regeneration.¹⁸⁻²⁰ Previous works have carried out the mineralization of recombinant collagen by adding a CaCl₂ solution to previously prepared collagen solution and mixing them for a period of 20 min. Then, NaHPO₄ solution was added slowly. The pH was regulated with NaOH solution at the end of the process.^{18,19} Wang *et al.* carried out mineralization of recombinant collagen by a similar protocol.²⁰

Herein, we proposed the bioinspired mineralization of recombinant collagen type I derived peptide (RCP) containing tri-amino acid sequence arginine-glycine-aspartic acid (RGD) that is the cell attachment site of a large number of adhesive extracellular matrix, blood and cell surface proteins. In fact, nearly half of the over 20 known integrins recognize this sequence in their adhesion protein ligands.²¹ The mineralization process has been adapted from the protocol developed by A. Tampieri *et al.*²² in order to synthesize biohybrid composite material with similar properties to biological bone using as source material animal-based collagen fibres. Magnesium (Mg) ions were introduced during the biomineralization process to closer mimic bone Ap ionic composition (Mg \approx 0.5-1 wt.%).²³ The role of both RCP and Mg ions in controlling the precipitation of the mineral phase was in depth evaluated.

3.2. Methods

The synthesis of Ap nanocrystals was carried out by the neutralization reaction in aqueous environment through dropping 5 mL of H₃PO₄ aqueous solution (0.71 M) into 5 mL of a basic aqueous suspension of Ca(OH)₂ (1.18M) (Ca/P molar ratio of 1.67). Mg-doped Ap (MgAp) as well as Ap synthesized in the presence of RCP (RCPAp) and both RCP and Mg (RCPMgAp) were prepared in the same conditions of Ap with slightly modifications. Namely MgAp was obtained by adding MgCl₂·6H₂O (at different Mg/Ca molar ratios, Table 1) to Ca(OH)₂ suspension whereas RCPAp was synthesized by dissolving RCP (1.5 mM) into H₃PO₄ aqueous solution at 40 °C (Figure 1). RCPMgAp was synthesized by dissolving RCP (1.5 mM) into H₃PO₄ aqueous solution at 40 °C and dropping this acid solution to Ca(OH)₂ suspension containing MgCl₂·6H₂O (at different initial Mg/Ca molar ratios, Table 1).

After neutralization reaction, the mixture was kept under stirring for 2 hours at room temperature. Then, mineralized suspension was washed three times by centrifugation and freeze-dried at -40 °C under vacuum (0.0858 mbar) overnight.

Table 1. Molar concentrations of reactants used for mineralization of Ap nanocrystals in the presence of Mg and/or RCP.

Sample	Ca(OH) ₂ , M	H ₃ PO ₄ , M	MgCl ₂ ·6H ₂ O, M	RCP, mM
Ap	1.18	0.71	----	----
MgAp5	1.18	0.71	0.06	----
MgAp10	1.18	0.71	0.12	----
MgAp15	1.18	0.71	0.18	----
RCPAp	1.18	0.71	----	1.5
RCPMgAp5	1.18	0.71	0.06	1.5
RCPMgAp10	1.18	0.71	0.12	1.5
RCPMgAp15	1.18	0.71	0.18	1.5

3.3. Results

The mineralization was carried out by neutralization reaction as we described previously.²⁴ We monitored the variation of the conductivity (k) of the reaction mixture with the time as an *in situ* measure of precipitation and phase evolution of calcium phosphate compounds during the mineralization process (Figure 1). Since the phase transformation leads to a change in composition in both the solution and the precipitate, *in situ* measurements on the variation of ionic concentration in solution during the reaction may give an insight into the reaction mechanism. Three regions can be

identified in the conductivity graph according to the rate of variation of conductivity (dC/dt) respect to the time (the inset graph Figure 1): i) conductivity decreased slowly ($dC/dt \approx -0.1$); ii) conductivity decreased abruptly with a rate of -1 mS/cm per min and iii) the conductivity remained stable ($dC/dt \approx 0$).

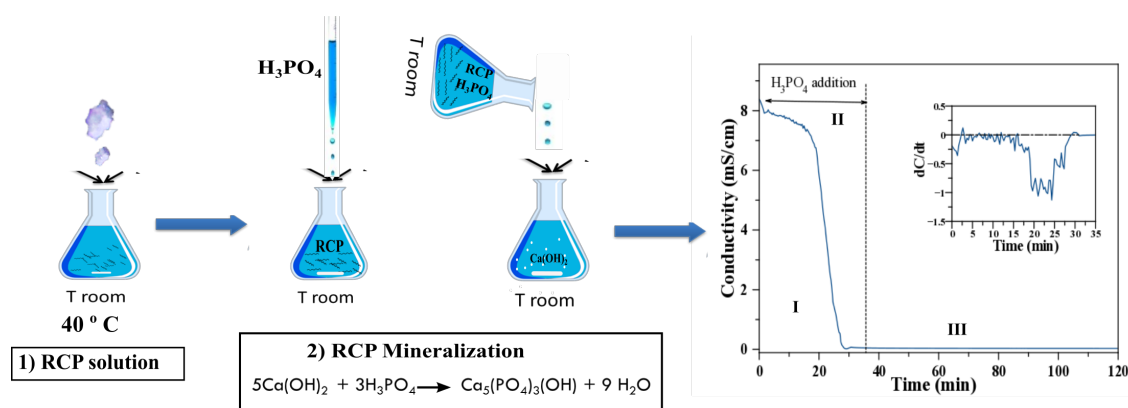


Figure 1. Sketch of RCP mineralization protocol. The graph displays the variation of the conductivity of the reaction mixture *versus* the reaction time. Inset displays the rate of variation of conductivity (dC/dt) respect to the time.

Figure 2a displays the XRD patterns of apatites synthesized with different Mg/Ca ratio in the absence (Ap, MgAp5, MgAp10 and MgAp15) and in the presence of RCP (RCPAp, RCPMgAp5, RCPMgAp10 and RCPMgAp15). All XRD patterns exhibit reflections ascribed to HA (ASTM card file No 9-432). Irrespectively of the mineralization conditions, the peaks are rather broad indicating low crystallinity and nano-sized dimensions of the diffracting crystal domains. The XRD patterns of the samples precipitated in the presence of the highest Mg concentrations (MgAp15 and RCPMgAp15) display the reflection at 29.40° (2θ) corresponding to the (104) plane of calcite (ASTM card file No. 5-586). The presence of a small quantity of calcite could be due to the spontaneous diffusion of atmospheric CO_2 during neutralization reaction or to the presence of CaCO_3 impurities in the reactants. CO_3^{2-} ions may affect calcium phosphate precipitation by blocking phosphate (resulting in a B-type carbonate substitution) or hydroxyl nucleation sites (resulting in a A-type carbonate substitution) or inducing CaCO_3 precipitation.²⁵ The average size of crystal domains along c -axis ($D_{[002]}$) and a - b plane (orthogonal to the c -axis, $D_{[310]}$), roughly estimated by using the Scherrer's equation, are reported in Table 2. Apatites synthesized in the presence of Mg exhibit a considerable reduction of the crystallite size along the c -axis providing more isometric crystals, in comparison to that of the samples synthesized without Mg (Ap and

RCPAp). This effect could be attributed to the inhibitory role of Mg on Ap crystal growth.²⁶ Individual effect of RCP on Ap crystallization also causes a decrease on crystal size along the *c*-axis but less prominent than in the case of the synergistic effect with Mg (Table 2). Moreover, the diffraction peaks of samples synthesized in the presence of magnesium (MgAp5, MgAp10 and MgAp15) are slightly shifted to higher 2θ values (Table 2) likely revealing a decrease in lattice parameters. This reduction could be associated to the partial Ca^{2+} (ionic radius: 0.99 Å) substitution by Mg^{2+} ions (ionic radius: 0.72 Å), as previously reported.²⁷

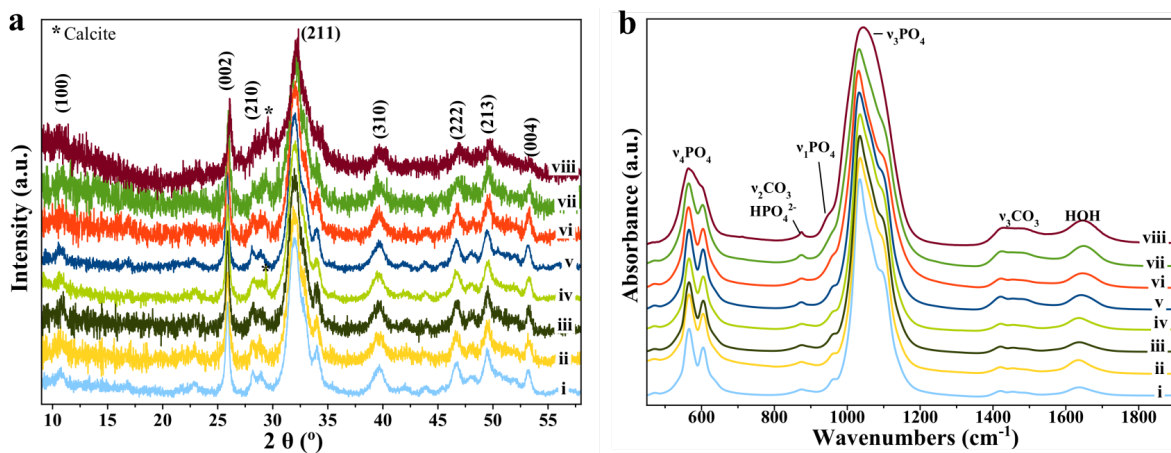


Figure 2. XRD (a) and FTIR (b) spectra of synthesized samples: i) Ap; ii) MgAp5; iii) MgAp10; iv) MgAp15; v) RCPAp; vi) RCPMgAp5; vii) RCPMgAp10 and viii) RCPMgAp15.

FTIR spectrum (Figure 2b) of synthesized samples exhibits phosphate vibrational peaks corresponding to HA: the main band of phosphate group appears at $\sim 1032 \text{ cm}^{-1}$ with shoulders at 1046 cm^{-1} and 1087 cm^{-1} due to the triply degenerated asymmetric stretching mode ($\nu_3\text{PO}_4$) and less intense peaks associated to triply degenerated bending mode (ν_4 of the O-P-O bond) appear at 602, 574 (shoulder) and 561 cm^{-1} .²⁸ FTIR spectrum of RCPMgAp15 exhibits broad and relatively featureless phosphate bands characteristic of ACP.²⁹ Sample crystallinity is calculated by evaluating the extent of splitting of the ν_4 absorption peak at $560\text{-}600 \text{ cm}^{-1}$ (Table 2).³⁰ Splitting factor (SF) values decreased for increasing concentrations of Mg in the absence and in the presence of RCP ranging from 2.40 up to 3.76, which are in the range of SF values determined for young and mature zebrafish bone.³ SF of RCPMgAp15 spectrum was not possible to calculate due to the broadening and overlap of the peaks under study. FTIR spectra show the ν_2 vibration mode of CO_3^{2-} group at 873 cm^{-1} and ν_3 vibration mode of CO_3 at

1424, 1454 and 1484 cm^{-1} , both of them corresponding with B-type carbonation (substitution of PO_4 by CO_3).³¹

Table 2. Position of (002) peak and average crystalline domain size along the [002] and [310] directions estimated through Scherrer's approximation for apatite nanocrystals synthesized under different conditions. (b) SF, crystallinity index (splitting factor) evaluated from ν_4 PO_4 vibrational mode in FTIR spectra.³⁰

Sample	(002) position ($2\theta^\circ$)	$D_{[002]}$, nm	$D_{[310]}$, nm	$D_{[002]}/$ $D_{[310]}$	SF ^b
Ap	25,877	60	10	6	3.76
MgAp5	25,890	34	8	4	2.78
MgAp10	25,900	31	7	4	2.68
MgAp15	25,908	34	9	4	2.49
RCPAp	25,874	51	9	6	3.51
RCPMgAp5	25,881	38	10	4	2.83
RCPMgAp10	25,879	34	9	4	2.40
RCPMgAp15	25,876	38	9	4	---

Samples were characterized by Raman Spectroscopy as a complementary technique. Raman spectra (Figure 3a) display the typical phosphate peaks belonging to HA. Concretely, the most intense peak at 961 cm^{-1} corresponds to the symmetric stretching mode (ν_1) of the tetrahedral PO_4 group while other less intense peaks appear at 433 cm^{-1} with a shoulder at 450 cm^{-1} (double degenerated bending mode ν_2), at 589 cm^{-1} with a shoulder at 612 cm^{-1} (triple degenerated bending mode ν_4) and at 1051 , 1075 and 1087 cm^{-1} (triple degenerated asymmetric stretching mode ν_3).²⁸ The main peak at 961 cm^{-1} is slightly broader in the spectra of apatites synthesized in the presence of Mg and RCP, showing a more prominent widening for the combined effect of RCP and Mg/Ca molar ratio of 0.15 (RCPMgAp15) (Figure 3b). The fitting of this peak for four representative samples (Ap, MgAp15, RCPAp and RCPMgAp15) (Figure 3c) shows the existence of two overlapping features: one at 952 cm^{-1} attributed to ACP³²⁻³⁴ and other one at 961 cm^{-1} attributed to HA.¹⁰ The area ratio of both features (A_{952}/A_{961}) was quantified for all samples. The results indicated a higher amount of ACP when mineralization was carried out at the highest Mg/Ca molar ratio (MgAp15) or in the presence of RCP (RCPAp) (Figure 3d). This effect was more prominent for the samples synthesized in presence of RCP and the highest Mg/Ca molar ratio (RCPMgAp15, Figure 3d). In addition, RCPMgAp5, RCPMgAp10 and RCPMgAp15 spectra also show a decreasing intensity and a widening of the apatitic ν_{OH} mode at $\sim 3570 \text{ cm}^{-1}$ (inset of Figure 3a), confirming the presence of higher amount of ACP.

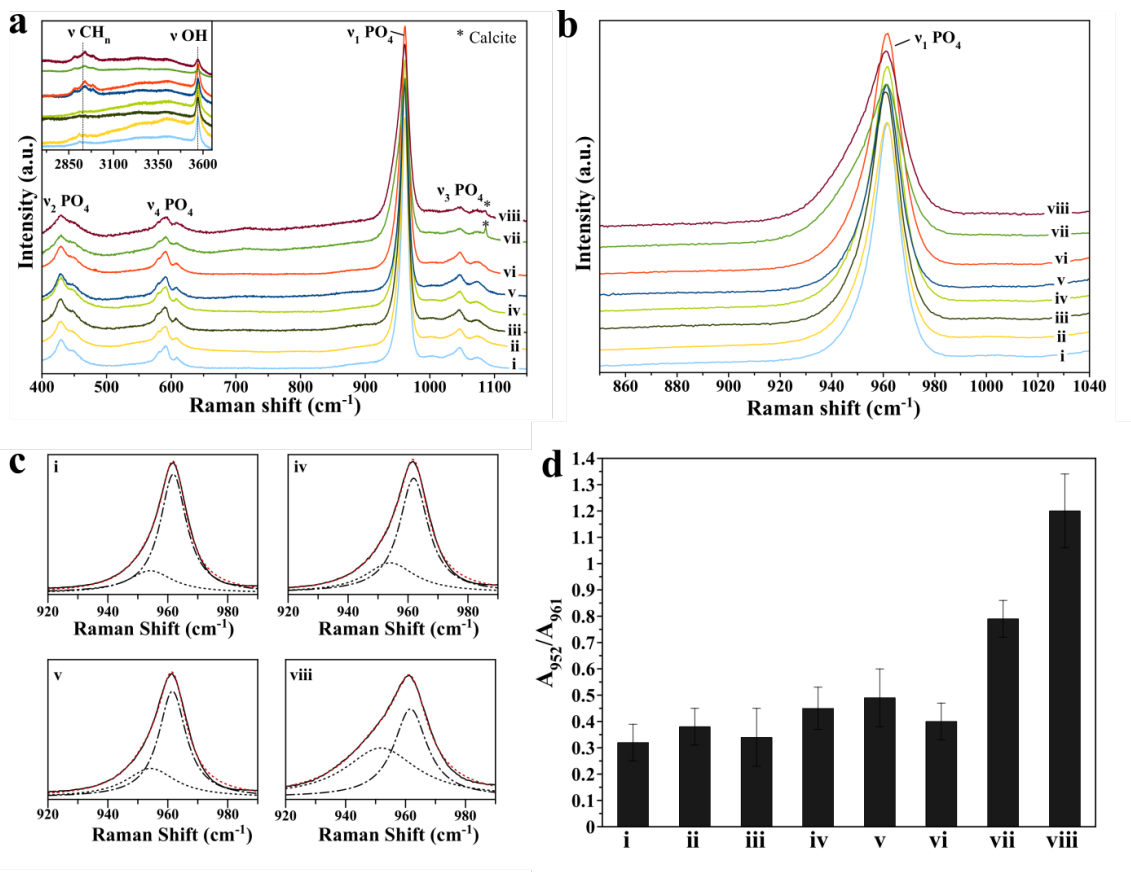


Figure 3. Raman spectra from 400-1150 cm⁻¹ (a) and in the ν₁ PO₄ mode region (b) collected for synthesized samples: i) Ap; ii) MgAp5; iii) MgAp10; iv) MgAp15; v) RCPAp; vi) RCPMgAp5; vii) RCPMgAp10 and viii) RCPMgAp15. (c) Curve fittings of the peak at ca 961 cm⁻¹ related to symmetric stretching mode (ν₁) of the tetrahedral PO₄ group in Raman spectra for 4 representative samples Ap (i), MgAp15 (iv), RCPAp (v) and RCPMgAp15 (viii). The vertical graph bar (d) represents the area ratio of ν₁ peaks from ACP (952 cm⁻¹) and Ap (961 cm⁻¹) for all the samples. Data are expressed as mean ± SD (n=3).

A deeply characterization by TEM, ICP-OES and TGA has been carried out for synthesized samples in the presence of the highest Mg/Ca molar ratio and/or RCP (Ap, MgAp15, RCPAp, RCPMgAp15). TEM observations of Ap, MgAp15, RCPAp and RCPMgAp15 revealed that poor crystalline Ap nanoparticles were obtained in all conditions without relevant differences in terms of nanoparticle dimensions and shape among them (length~100nm and width~10nm) (Figure 4). SAED pattern (inset in Figure 4a) of Ap elongated nanocrystals showed diffraction rings of the typical 002 and 211 hydroxyapatite reflections (HA, ASTM card file 09-432). We can distinguish the presence of smaller round shape nanoparticles (indicated by the white arrows) that could be attributed to ACP, according to Raman spectroscopy studies. Inspections at higher magnifications of RCPMgAp15 (inset Figure 4d) revealed lattice fringes spaced

at *ca.* 0.344 nm corresponding to the distance of the (002) plane of HA (ASTM card file 09-432). Moreover, the edge of the nanocrystals exhibits lack of order that could be associated to the presence of an amorphous layer covering the crystalline core, as previously proposed.^{10,35}

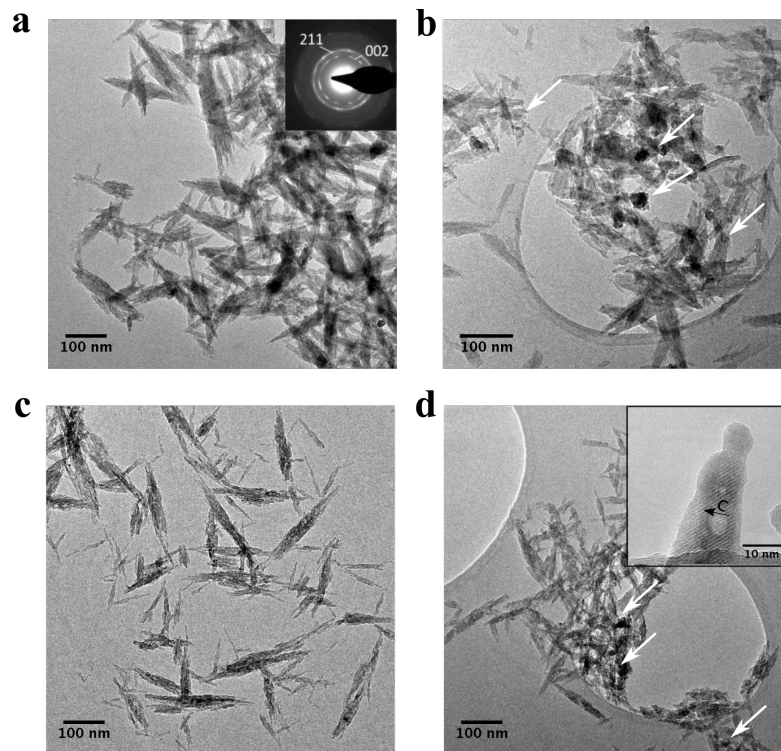


Figure 4. TEM micrographs of powdered samples synthesized in different conditions: (a) Ap, where inset shows corresponding SAED pattern; (b) MgAp15; (c) RCPAp and (d) RCPMgAp15, where inset shows High-Resolution TEM images of a nanocrystal.

The chemical composition of Ap, MgAp15, RCPAp and RCPMgAp15 was analyzed by ICP-OES and TGA (Table 3). ICP-OES analysis indicated that the Mg content in the precipitates was lower than that used during the synthesis (Mg/Ca=15 % mol). Less than a half of the initial amount of Mg was incorporated into MgAp15 precipitates whereas higher Mg content was incorporated in RCPMgAp15 samples (Table 3). The Ca/P ratio of Ap and RCPAp samples were closer to stoichiometric HA (Ca/P=1.67) whereas MgAp15 and RCPMgAp15 showed lower values. The specific surface area (SSA) of the precipitates is also shown in Table 3. Noticeably, samples synthesized in the presence of Mg and/or RCP exhibited higher SSA than Ap.

Table 3. Chemical composition of Ap, MgAp15, RCPAp and RCPMgAp15 samples. (a) Elemental composition calculated from ICP-OES analysis; (b) RCP and water content (wt.%) determined from TGA curves and (c) specific surface area calculated from BET adsorption. Data are expressed as mean \pm SD (n=3).

Sample	Ca/P (mol) ^a	Mg (wt.%) ^a	Mg/Ca (%mol) ^a	RCP (wt%) ^b	Water (wt.%) ^b	SSA _{BET} (m ² g ⁻¹) ^c
Ap	1.58 \pm 0.10	-----	-----	-----	4.86 \pm 0.17	73.36
MgAp15	1.54 \pm 0.04	1.06 \pm 0.02	5.14 \pm 0.14	-----	6.28 \pm 0.11	99.21
RCPAp	1.64 \pm 0.06	-----	-----	2.87 \pm 0.32	6.63 \pm 0.24	95.77
RCPMgAp15	1.54 \pm 0.03	1.50 \pm 0.01	8.05 \pm 0.12	3.79 \pm 0.44	9.24 \pm 0.19	91.14

Thermogravimetric analyses were carried out to quantify the presence of RCP (water soluble peptide) that remained attached to Ap after the washing procedure (Figure 5). Firstly, thermogravimetric analysis of RCP stock material was carried out to determine its degradation temperature that was closed to 273 °C (TGA-DSC curve, Figure 5a). RCP was completely degraded at 700 °C. TGA curve of Ap, MgAp15, RCPAp and RCPMgAp15 (Figure 5b) mainly exhibited four weight losses that were attributed to adsorbed water (from room temperature to 150 °C), structural water (from 150 to 400 °C),³⁶ RCP (from 270 to 700 °C) and carbonate (from 700 to 1000 °C).¹⁰ Table 3 covers the weight loss belongs to decomposition of water and RCP calculated from TGA curves of synthesized samples. Higher amount of RCP was bound to Ap when mineralization took place in presence of magnesium (RCPMgAp15). Moreover, higher water content was obtained for the samples synthesized in the presence of Mg and/or RCP when compared to Ap. Probably, a higher amount of ACP in the Mg- and/or RCP-containing sample is the responsible of this finding.

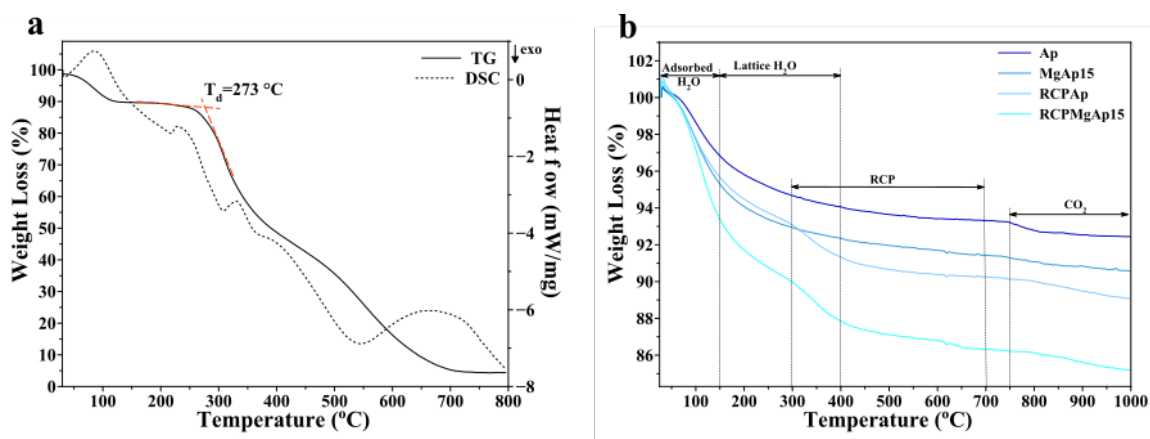


Figure 5. (a) TGA/DSC curve of RCP where the thermal degradation temperature of RCP was determined close to 273 °C and (b) TGA curves of Ap, MgAp15, RCPAp and RCPMgAp15 samples.

3.4. Discussion

In this chapter, we have adapted the bioinspired mineralization protocol of natural collagen developed by Tampieri *et al.*³⁷ for the mineralization of recombinant collagen peptide. We have studied the process *in situ* with conductivity measurements and characterized the powdered samples to evaluate the role of RCP and/or Mg in the mineralization mechanism of calcium phosphate.

The *in situ* measurement of the electrical conductivity variation, that can be considered to be an indirect way of measuring ionic concentration, might give an insight into the reaction mechanism and transformations. Electrical conductivity values during mineralization indicated the presence of three regions. According to previous studies,³⁸ region I can be associated to ACP formation step and region II to ACP to HA transformation. No noticeable changes on the conductivity in the region III might indicate that the final product was reached exactly after the end of acid addition. Several calcium phosphate phases have been proposed as Ap precursor phase depending on pH of the solution. In slightly acidic solutions the transformation occurs via octacalcium phosphate (OCP, $\text{Ca}_4\text{H}(\text{PO}_4)_3 \cdot 2.5\text{H}_2\text{O}$) and/or dicalcium phosphate dihydrate (DCPD, $\text{CaHPO}_4 \cdot 2\text{H}_2\text{O}$) whereas in basic solutions, it occurs via amorphous calcium phosphate (ACP, $\text{Ca}_3(\text{PO}_4)_2 \cdot \text{H}_2\text{O}$).³⁹⁻⁴¹ Prakash *et al.* correlated the variations of the conductivity of the reaction mixture with ionic concentration and determined that $\text{Ca}_3(\text{PO}_4)_2$ is the precursor phase of HA during the CaP precipitation through dropwise phosphoric acid into calcium hydroxide solution.³⁸

In our work, poor crystalline apatites (Ap) were obtained in all the conditions, as indicated XRD and FTIR spectra of synthesized samples. Furthermore, the presence of ACP was detected by Raman Spectroscopy. In detail, crystal domain sizes estimated along [002] and [310] directions have put in evidence the role of Mg in inhibiting Ap crystal growth along the *c*-axis, providing thus more isometric crystals. FTIR indicated lower splitting factor for crystallization experiments in the presence of Mg and/or RCP. It was not possible to calculate the SF for RCPMgAp15 due to lack of crystallinity. SF values were in the range of that found for fin bones of zebrafish. Lower SF values are related to young forming bones whereas higher values correspond to mature bone, indicating the increase of crystallinity with the bone maturation.³ Raman spectra have also shown that Mg and RCP synergistically induced a stronger stabilization of ACP with respect to their individual role. In fact, RCPMgAp15 seems to be mainly

composed for ACP. It has been previously proposed that Mg kinetically hinders nucleation and subsequent growth of Ap by competing for structural sites with chemically similar but larger Ca ions, favouring stabilization of ACP.²⁶ Francesco Abbona *et al.* determined that the presence of magnesium in the solution prolonged by at least four times the induction time of transformation of ACP into HA. The influence of magnesium was attributed to its incorporation in the ACP cluster and Ap pre-nuclei and also its adsorption onto the surfaces of ACP and Ap crystallites.⁴² The inhibitory effect of organic molecules (i.e., amino acids, biological macromolecules or small molecules such as citrate) on Ap crystallization via ACP precursors is also well reported.^{6,7,9,10,43} In fact, NCPs, due to their poly-anionic character, have been proposed to play an essential role in controlling mineral deposition and growth during bone formation.^{2,44,45} Conversely, only few studies on the simultaneous action of Mg and organic molecules as stabilizers of ACP have been carried out to date. In particular, Tao *et al.* pointed out that either Mg or aspartate monomer can stabilize the ACP phase whereas their cooperative effect consists in a switch on crystallization mechanism in which Mg inhibits ACP to Ap transformation whilst aspartate monomers promote the transformation.⁴⁶ On the other hand, Yang *et al.* suggested that acidic (Asp), neutral (Gly) and basic (Lys) amino acids in the absence and in the presence of Mg ions promoted Ap nucleation by shortening the induction and transformation times.⁷ Despite that the amino acid sequences for a number of proteins involved in the biomineralization processes have been determined, the effect of specific amino acid sequences and Mg ions is still unclear.

Considering that relevance differences were found between Ap, MgAp15, RCPAp and RCPMgAp15 samples, these samples were thoroughly investigated and Mg/Ca molar ratio 0.15 was selected for the further studies along this thesis.

TEM images revealed that Ap nanocrystals surrounded by an amorphous layer were obtained for all evaluated conditions. In fact, the presence of round shape nanoparticles in TEM images of MgAp15 and RCPMgAp15 might indicate the role of ACP as metastable precursor phase. Elemental compositional analysis by ICP-OES indicated a higher Mg incorporation on synthesized Ap in the presence of RCP (RCPMgAp15) compared to synthesized samples with the same Mg/Ca molar ratio but in the absence of RCP (MgAp15). Ca/P ratio of RCPMgAp15 samples was lower than that of stoichiometric HA (Ca/P=1.67) that can be associated to the presence of ACP that present lower Ca/P molar ratio.⁴⁷ RCPMgAp15 showed higher Mg content compared to

MgAp15. This effect could be attributed to a larger presence of amorphous phase for RCPMgAp15 as well as ion-sequestration by positively charged carboxylate groups from aspartic and glutamic acid residues of RCP which remained adsorbed into Ap surface of RCPMgAp15, as indicated TGA analysis. TGA curve of RCPMgAp15 showed higher water content as well as a higher amount of bound RCP respect to RCPAp samples. These effects can be associated to the fact that Mg sites can coordinate and bind water in a higher extent than Ca, thus leading to a more effective protein adsorption.⁴⁸

3.5. Conclusions

Understanding the mineralization mechanism of synthetic peptide has recently aroused great interest especially in the development of advanced materials for bone regeneration. Herein, we study the mineralization of a recombinant collagen type I derived peptide (RCP) enriched with RGD sequences through a neutralization reaction, previously applied for natural collagen mineralization. Moreover, magnesium ions (Mg) are introduced to closer mimic bone composition. The role of both RCP and Mg ions in controlling the precipitation of the mineral phase is in depth evaluated. TEM and X-Ray powder diffraction reveal the crystallization of nanocrystalline apatite (Ap) in all the evaluated conditions with a clear effect of Mg on decreasing crystallite size along *c*-axis. However, Raman spectra point out also the precipitation of amorphous calcium phosphate (ACP). This amorphous phase is more evident when RCP and Mg (Mg/Ca molar ratio 0.15) are at work, indicating the synergistic role of both in stabilizing the amorphous precursor. To the best of our knowledge this work represents the first attempt to mineralize recombinant collagen type I derived peptide proving the simultaneous effect of the organic phase (RCP) and Mg on ACP stabilization. This study opens the possibility to engineer, through biomineralization process, advanced hybrid matrices for bone regeneration (Chapter 4).

References

1. Nudelman, F. and Sommerdijk, N.A.J.M. Biomineralization as an Inspiration for Materials Chemistry. *Angew Chem Int Ed* **51**, 6582, 2012.
2. Olszta, M.J., Cheng, X., Jee, S.S., Kumar, R., Kim, Y.-Y., Kaufman, M.J., Douglas, E.P. and Gower, L.B. Bone structure and formation: A new perspective. *Mater Sci Eng R* **58**, 77, 2007.
3. Mahamid, J., Sharir, A., Addadi, L. and Weiner, S. Amorphous calcium phosphate is a major component of the forming fin bones of zebrafish:

- Indications for an amorphous precursor phase. *Proc Natl Acad Sci USA* **105**, 12748, 2008.
4. Beniash, E., Metzler, R.A., Lam, R.S.K. and Gilbert, P.U.P.A. Transient amorphous calcium phosphate in forming enamel. *J Struct Biol* **166**, 133, 2009.
 5. Mahamid, J., Aichmayer, B., Shimoni, E., Ziblat, R., Li, C., Siegel, S., Paris, O., Fratzl, P., Weiner, S. and Addadi, L. Mapping amorphous calcium phosphate transformation into crystalline mineral from the cell to the bone in zebrafish fin rays. *Proc Natl Acad Sci USA* **107**, 6316, 2010.
 6. Gómez-Morales, J., Delgado-López, J.M., Iafisco, M., Hernández-Hernández, A. and Prat, M. Amino Acidic Control of Calcium Phosphate Precipitation by Using the Vapor Diffusion Method in Microdroplets. *Cryst Growth Des* **11**, 4802, 2011.
 7. Yang, X., Xie, B., Wang, L., Qin, Y., Henneman, Z.J. and Nancollas, G.H. Influence of magnesium ions and amino acids on the nucleation and growth of hydroxyapatite. *CrystEngComm* **13**, 1153, 2011.
 8. Palazzo, B., Walsh, D., Iafisco, M., Foresti, E., Bertinetti, L., Martra, G., Bianchi, C.L., Cappelletti, G. and Roveri, N. Amino acid synergetic effect on structure, morphology and surface properties of biomimetic apatite nanocrystals. *Acta Biomater* **5**, 1241, 2009.
 9. George, A. and Veis, A. Phosphorylated Proteins and Control over Apatite Nucleation, Crystal Growth, and Inhibition. *Chem Rev* **108**, 4670, 2008.
 10. Delgado-López, J.M., Iafisco, M., Rodríguez, I., Tampieri, A., Prat, M. and Gómez-Morales, J. Crystallization of bioinspired citrate-functionalized nanoapatite with tailored carbonate content. *Acta Biomater* **8**, 3491, 2012.
 11. Delgado-López, J.M., Frison, R., Cervellino, A., Gómez-Morales, J., Guagliardi, A. and Masciocchi, N. Crystal Size, Morphology, and Growth Mechanism in Bio-Inspired Apatite Nanocrystals. *Adv Funct Mater* **24**, 1090, 2014.
 12. Iafisco, M., Ramírez-Rodríguez, G.B., Sakhno, Y., Tampieri, A., Martra, G., Gómez-Morales, J. and Delgado-López, J.M. The growth mechanism of apatite nanocrystals assisted by citrate: relevance to bone biomineralization. *CrystEngComm* **17**, 507, 2015.
 13. Nudelman, F., Pieterse, K., George, A., Bomans, P.H.H., Friedrich, H., Brylka, L.J., Hilbers, P.A.J., de With, G. and Sommerdijk, N. The role of collagen in bone apatite formation in the presence of hydroxyapatite nucleation inhibitors. *Nat Mater* **9**, 1004, 2010.
 14. SPRIO, S., SANDRI, M., PANSERI, S. and IAFISCO, M. Bone substitutes based on biomineralization. *Bone Substitute Biomaterials*, 1, 2014.
 15. Tampieri, A., Sandri, M., Landi, E., Pressato, D., Francioli, S., Quarto, R. and Martin, I. Design of graded biomimetic osteochondral composite scaffolds. *Biomaterials* **29**, 3539, 2008.
 16. Kon, E., Delcogliano, M., Filardo, G., Fini, M., Giavaresi, G., Francioli, S., Martin, I., Pressato, D., Arcangeli, E., Quarto, R., Sandri, M. and Marcacci, M. Orderly osteochondral regeneration in a sheep model using a novel nano-composite multilayered biomaterial. *J Orth Res* **28**, 116, 2010.
 17. Luo, T. and Kiick, K.L. Collagen-like peptides and peptide-polymer conjugates in the design of assembled materials. *Eur Polym J* **49**, 2998, 2013.
 18. Zhai, Y., Cui, F.Z. and Wang, Y. Formation of nano-hydroxyapatite on recombinant human-like collagen fibrils. *Curr Appl Phys* **5**, 429, 2005.
 19. Zhai, Y. and Cui, F. Recombinant human-like collagen directed growth of hydroxyapatite nanocrystals. *J Cryst Growth* **291**, 202, 2006.

20. Wang, Y., Cui, F., Zhai, Y., Wang, X., Kong, X. and Fan, D. Investigations of the initial stage of recombinant human-like collagen mineralization. *Mater Sci Eng C* **26**, 635, 2006.
21. Ruoslahti, E. RGD and other recognition sequences for integrins. *Annu Rev Cell Dev Biol* **12**, 697, 1996.
22. Tampieri, A., Celotti, G., Landi, E., Sandri, M., Roveri, N. and Falini, G. Biologically inspired synthesis of bone - like composite: Self - assembled collagen fibers/hydroxyapatite nanocrystals. *Journal of Biomedical Materials Research Part A* **67**, 618, 2003.
23. Gómez-Morales, J., Iafisco, M., Delgado-López, J.M., Sarda, S. and Drouet, C. Progress on the preparation of nanocrystalline apatites and surface characterization: Overview of fundamental and applied aspects. *Prog Cryst Growth Ch* **59**, 1, 2013.
24. Sprio, S., Tampieri, A., Landi, E., Sandri, M., Martorana, S., Celotti, G. and Logroscino, G. Physico-chemical properties and solubility behaviour of multi-substituted hydroxyapatite powders containing silicon. *Mater Sci Eng C* **28**, 179, 2008.
25. Rodriguez-Lorenzo, L. and Vallet-Regi, M. Controlled crystallization of calcium phosphate apatites. *Chem Mater* **12**, 2460, 2000.
26. Ferguson, J.F. and McCarty, P.L. Effects of carbonate and magnesium on calcium phosphate precipitation. *Environ Sci Technol* **5**, 534, 1971.
27. Geng, Z., Cui, Z., Li, Z., Zhu, S., Liang, Y., Lu, W.W. and Yang, X. Synthesis, characterization and the formation mechanism of magnesium-and strontium-substituted hydroxyapatite. *Journal of Materials Chemistry B* **3**, 3738, 2015.
28. Koutsopoulos, S. Synthesis and characterization of hydroxyapatite crystals: A review study on the analytical methods. *J Biomed Mater Res* **62**, 600, 2002.
29. Gadaleta, S., Paschalis, E., Betts, F., Mendelsohn, R. and Boskey, A. Fourier transform infrared spectroscopy of the solution-mediated conversion of amorphous calcium phosphate to hydroxyapatite: new correlations between X-ray diffraction and infrared data. *Calcif Tissue Int* **58**, 9, 1996.
30. Termine, J.D. and Posner, A.S. Infra-red determination of the percentage of crystallinity in apatitic calcium phosphates. 1966.
31. Antonakos, A., Liarokapis, E. and Leventouri, T. Micro-Raman and FTIR studies of synthetic and natural apatites. *Biomaterials* **28**, 3043, 2007.
32. Sauer, G.R., Zunic, W.B., Durig, J.R. and Wuthier, R.E. Fourier transform raman spectroscopy of synthetic and biological calcium phosphates. *Calcif Tissue Int* **54**, 414, 1994.
33. Ramírez-Rodríguez, G.B., Delgado-López, J.M. and Gómez-Morales, J. Evolution of calcium phosphate precipitation in hanging drop vapor diffusion by in situ Raman microspectroscopy. *CrystEngComm* **15**, 2206, 2013.
34. Chatzipanagis, K., Iafisco, M., Roncal-Herrero, T., Bilton, M., Tampieri, A., Kröger, R. and Delgado-López, J.M. Crystallization of citrate-stabilized amorphous calcium phosphate to nanocrystalline apatite: a surface-mediated transformation. *CrystEngComm* **18**, 3170, 2016.
35. Sakhno, Y., Bertinetti, L., Iafisco, M., Tampieri, A., Roveri, N. and Martra, G. Surface Hydration and Cationic Sites of Nanohydroxyapatites with Amorphous or Crystalline Surfaces: A Comparative Study. *J Phys Chem C* **114**, 16640, 2010.
36. LeGeros, R.Z., Bonel, G. and Legros, R. Types of “H₂O” in human enamel and in precipitated apatites. *Calcif Tissue Res* **26**, 111, 1978.

37. Tampieri, A., Celotti, G., Landi, E., Sandri, M., Roveri, N. and Falini, G. Biologically inspired synthesis of bone-like composite: Self-assembled collagen fibers/hydroxyapatite nanocrystals. *J Biomed Mater Res A* **67A**, 618, 2003.
38. Prakash, K., Kumar, R., Ooi, C., Cheang, P. and Khor, K. Conductometric study of precursor compound formation during wet-chemical synthesis of nanocrystalline hydroxyapatite. *The Journal of Physical Chemistry B* **110**, 24457, 2006.
39. Nancollas, G. and Tomazic, B. Growth of calcium phosphate on hydroxyapatite crystals. Effect of supersaturation and ionic medium. *J Phys Chem* **78**, 2218, 1974.
40. Boskey, A.L. and Posner, A.S. Conversion of amorphous calcium phosphate to microcrystalline hydroxyapatite. A pH-dependent, solution-mediated, solid-solid conversion. *J Phys Chem* **77**, 2313, 1973.
41. Meyer, J.L. and Weatherall, C.C. Amorphous to crystalline calcium phosphate phase transformation at elevated pH. *J Colloid Interf Sci* **89**, 257, 1982.
42. Abbona, F. and Baronnet, A. A XRD and TEM study on the transformation of amorphous calcium phosphate in the presence of magnesium. *J Cryst Growth* **165**, 98, 1996.
43. Nudelman, F., Pieterse, K., George, A., Bomans, P.H.H., Friedrich, H., Brylka, L.J., Hilbers, P.A.J., De With, G. and Sommerdijk, N.A.J.M. The role of collagen in bone apatite formation in the presence of hydroxyapatite nucleation inhibitors. *Nat Mater* **9**, 1004, 2010.
44. Glimcher, M.J. and Muir, H. Recent Studies of the Mineral Phase in Bone and Its Possible Linkage to the Organic Matrix by Protein-Bound Phosphate Bonds [and Discussion]. *Philos Trans R Soc Lond B Biol Sci* **304**, 479, 1984.
45. Landis, W.J., Song, M.J., Leith, A., McEwen, L. and McEwen, B.F. Mineral and Organic Matrix Interaction in Normally Calcifying Tendon Visualized in Three Dimensions by High-Voltage Electron Microscopic Tomography and Graphic Image Reconstruction. *J Struct Biol* **110**, 39, 1993.
46. Tao, J., Zhou, D., Zhang, Z., Xu, X. and Tang, R. Magnesium-aspartate-based crystallization switch inspired from shell molt of crustacean. *Proc Natl Acad Sci USA* **106**, 22096, 2009.
47. Combes, C. and Rey, C. Amorphous calcium phosphates: Synthesis, properties and uses in biomaterials. *Acta Biomater* **6**, 3362, 2010.
48. Bertinetti, L., Drouet, C., Combes, C., Rey, C., Tampieri, A., Coluccia, S. and Martra, G. Surface Characteristics of Nanocrystalline Apatites: Effect of Mg Surface Enrichment on Morphology, Surface Hydration Species, and Cationic Environments. *Langmuir* **25**, 5647, 2009.

Chapter 4: Biomimetic mineralization of recombinant collagen peptide to obtain hybrid matrices for bone regeneration

4.1. Introduction

Bone, in dry conditions, is defined as bioceramic composite mainly made of collagen type I (~30 wt.%) and hard inorganic components (~70 wt.%, belonging to poor crystalline hydroxyapatite, HA).¹ The degree of mineralization varies within different bone tissues. For instance, mineral density of trabecular bone from the calcaneus was measured at $1.136 \pm 0.147 \text{ g/cm}^3$, while in trabecular bone from the iliac crest it was indicated close to $1.099 \pm 0.077 \text{ g/cm}^3$.² Composite biomaterial can combine the advantages of both materials, the strength of a ceramic phase (i.e., calcium phosphate phase, CaP) and the toughness and plasticity of a polymer phase. Furthermore, the introduction of CaP into an organic matrix could enhance the biological tissue response owing to the osteoconductive properties of CaP such as hydroxyapatite.^{3,4} However, the blending of ceramic materials with polymers presents several drawbacks, including poor dispersion and agglomeration that leads to heterogeneous composition of the blend as well as reduction in mechanical properties.⁴ Substantial research efforts have already been focused on the development of ceramic-polymer composites for bone graft applications, in which the major challenge was related to achieve a good chemical and/or physical bond between the polymer and the ceramic phase. For instance, bio-inspired mineralization of natural collagen (e.g., extracted from horse tendon) has been extensively applied for the development of nanocomposite scaffolds with good interaction between the mineral and the organic phase.⁵ The process enables the direct nucleation of HA nanocrystals on self-assembled collagen fibres. In this case, the two components (80 wt.% HA and 20 wt.% collagen) exhibited strong interactions since collagen negatively charged carboxylate groups bound to the calcium ions of HA. The composite materials showed a complete analogy with calcified natural tissue.⁶

The goal of this PhD is the fabrication of new hybrid scaffolds with enhancing biofunctionality through biomimetic mineralization (adapted from bioinspired mineralization of natural collagen developed by Tampieri *et al.*⁶) of a recombinant collagen type I derived peptide (RCP) enriched in RGD sequences. However, unlike collagen, RCP is water-soluble and does not self-assembly into large microfibers.

Therefore, the forthcoming goal is to determine the maximum mineral extent, obtained after RCP mineralization, to maintain a good chemical interaction between the two phases and a uniform mineral integration into the organic matrix since both of them will ensure a homogeneous composition of the designed scaffolds through freeze-drying the mineralized slurry.

In addition to the chemical similarity to the bone tissue, the nanocomposite biomaterials obtained through biomimetic mineralization also exhibit unique surface properties such as surface topography, specific surface area, surface wettability and surface energy. It is well-known that material surface properties mediate specific protein adsorption (i.e., fibronectin, vitronectin and laminin) and bioactivity before cells adhere on implants, further regulating cell behaviour and dictating tissue regeneration and osseointegration of the material.⁷ Several studies have demonstrated that nanostructured materials with cell favourable surface properties may promote greater amounts of specific protein interactions to more efficiently stimulate new bone growth compared to conventional materials.⁸ Biomimetic mineralization approach allows to tailor the physic-chemical properties of the mineral phase and subsequent interfacial properties of designed materials enhancing their osteoconductivity and osteoinductivity.^{9,10} For instance, previous *in vivo* studies of calcium phosphate coatings indicated that early bone formation was dependent on the nanosized hydroxyapatite features, but it was unclear whether this finding was an isolated effect of the chemistry, an isolated effect of the nanotopography or a combined effect of both.¹¹ In this chapter, hybrid matrices are developed through biomimetic mineralization of RCP in the absence (Ap/RCP) and in the presence of magnesium (MgAp/RCP). The chemical interaction between mineral phase and organic matrix was evaluated by FTIR spectroscopy. Furthermore, mineral distribution in the organic matrix for both scaffold compositions was assessed by SEM and AFM. The interfacial properties were evaluated both at nanoscale (roughness values) and macroscopic level (hydrophobicity and water retention ability). The correlation between the scaffold interfacial properties and the extent of mineralization, the mineral composition, crystallinity and morphology and the mineral integration in organic matrix resulting from mineralization process of RCP was investigated.

4.2. Methods

4.2.1. Prototype 3D scaffolds: Evaluation of the maximum mineral content

3D scaffold prototypes with increasing mineral/organic weight ratio (min/org) were developed by biomimetic mineralization of RCP (previously described in chapter 3) and further freeze-drying of mineralized suspension. The reagent concentrations for each scaffold composition are summarized in table 1. The samples were characterized by X-ray powder diffraction (XRD), thermogravimetric analysis (TGA) and scanning electron microscopy (SEM).

Table 1. Concentrations of the reagents for the preparation of hybrid matrices with increasing min/org weight ratio.

Min/Org (wt.%)	Ca(OH) ₂ , M	H ₃ PO ₄ , M	RCP , mM
40/60	1.18	0.71	1.50
50/50	1.58	0.95	1.56
60/40	2.45	1.47	1.61
70/30	4.03	2.42	1.70

4.2.2. Preparation of hybrid matrices of different compositions

Mineralized hybrid matrices (min/org=40/60) in the absence (Ap/RCP) and in the presence of magnesium (MgAp/RCP) were developed by the same mineralization protocol described previously for the synthesis of RCPAp and RCPMgAp15 samples, respectively (Chapter 3). In this case, mineralized slurry was freeze-dried after 2 hours of mineralization. Non-mineralized matrices (RCP) were also prepared as a control by freeze-drying RCP solution (7.5 wt.%). Samples were characterized by FTIR spectroscopy, SEM and atomic force microscopy (AFM). Wettability and swelling capacity of hybrid matrices were also evaluated.

Scaffold prototypes and hybrid matrices were fabricated by freeze-drying in a teflon mould in the freeze-drier (5Pascal, Cinquepascal srl, Italy). The final freezing temperature was set up at -40 °C with a constant cooling rate of 10 °C/h. Once the samples reached -40 °C, drying process started by heating up to 25 °C with a heating rate of 5 °C/h under vacuum (0.0858 mbar).

4.3. Results

4.3.1. Amount of mineral suitable to obtain 3D structures

Prototype 3D porous scaffolds were obtained for an initial min/org weight ratio up to 60/40 whereas powdered and brittle samples were obtained for an initial min/org weight ratio of 70/30 (Table 2). XRD patterns of designed scaffolds showed the presence of hydroxyapatite (HA, ASTM Card file No 9-432,) as unique crystalline phase (Figure 1a). The mineral content at the top and base of the scaffolds was calculated by TGA (Table 2) as the residual mass of the samples at 800 °C, temperature in which RCP is completely degraded ($T_d=273$ °C, see chapter 3). The base of scaffolds showed a higher mineral content due to sedimentation of the mineral phase during the freezing stage (Table 2). In fact, scaffolds developed with higher initial min/org weight ratio, showed a higher mineral deposition with relevant difference on the mineral content from the top to the base of the scaffold (Figure 1b). Scaffolds with an initial min/org weight ratio of 40/60 showed the most homogeneous mineral distribution.

Table 2. Macroscopic structure of prototype scaffolds and mineral/organic weight ratio at the top and base of scaffolds calculated by TGA.

(Min/Org) _{Th} (wt.%)	Structure	(Min/Org) _{Top} (wt.%)	(Min/Org) _{Base} (wt.%)
40/60	Scaffold	40/60	45/55
50/50	Scaffold	40/60	56/46
60/40	Brittle Scaffold	46/54	63/37
70/30	Powder	-----	-----

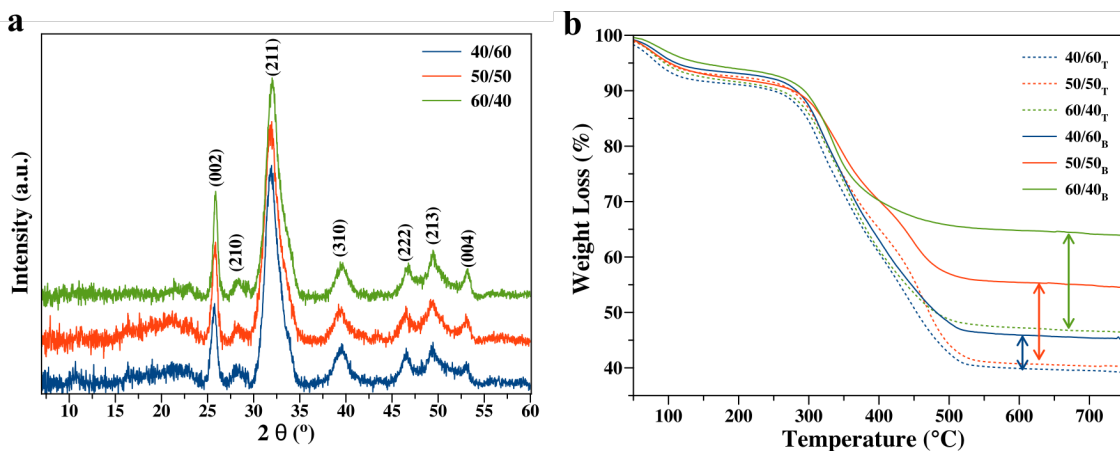


Figure 1. XRD (a) and TGA curves (b) of top (discontinuous line) and base (continuous line) of mineralized scaffolds developed with three different theoretical min/org weight ratio: 40/60, 50/50 and 60/40.

SEM observations showed a more homogeneous porous structure for prototype scaffolds with the lowest min/org weight ratio (40/60) whereas more compact and heterogeneous structures were obtained for scaffolds developed with higher initial mineral content (50 and 60 wt.%) (Figure 2). SEM images at higher magnification of the surface of the scaffolds (at the base of the scaffold) showed a uniform mineral incorporation into the organic matrix for scaffold prototypes developed with the lowest mineral content (40 wt.%). On the other hand, micrometric mineral aggregates (indicated with white arrows in Figure 2), that seemed not to be incorporated into the organic matrix, were identified at the base of scaffold prototypes with higher mineral content (50 and 60 wt.%).

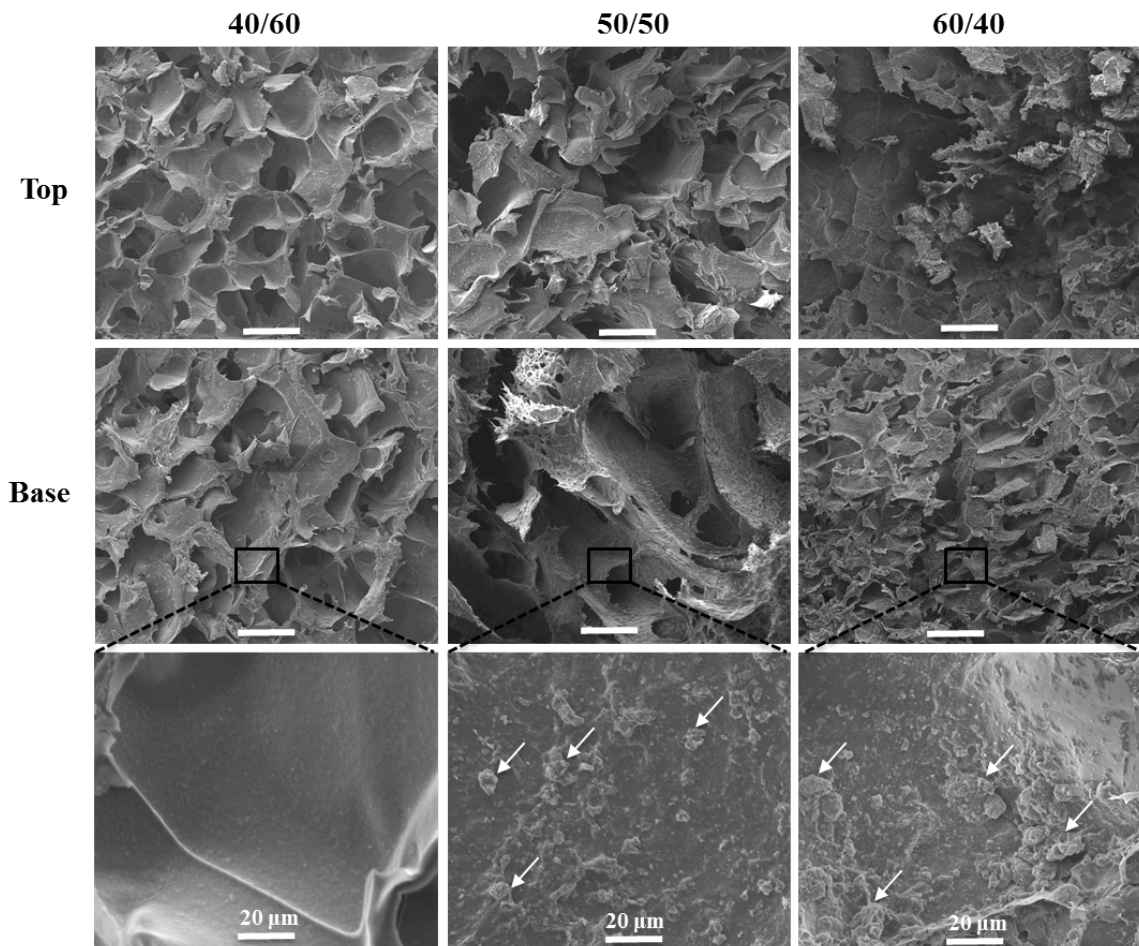


Figure 2. SEM micrographs of the top and base of scaffold prototypes designed with increasing initial mineral/organic weight ratio: 40/60, 50/50 and 60/40. Scale bar: 250 μm. Higher magnification SEM images of the scaffold surface at the base.

4.3.2. How modification of mineralization protocol can alter macroscopic properties?

The chemical interaction between the mineral and the organic phase of hybrid matrices was evaluated by FTIR spectroscopy. Figure 3 displays the FTIR spectrum of non-mineralized matrix showing the RCP amide bands, i.e., amide I (1637 cm^{-1}), amide II (1542 cm^{-1}) and amide III (1242 cm^{-1}).¹² FTIR spectrum of Ap/RCP matrix exhibits amide bands of RCP together with phosphate vibrational peaks corresponding to HA: the main band of phosphate group appears at $\sim 1032\text{ cm}^{-1}$ with shoulders at 1046 cm^{-1} and 1087 cm^{-1} due to the triply degenerated asymmetric stretching mode ($\nu_3\text{PO}_4$) and less intense peaks associated to triply degenerated bending mode (ν_4 of the O-P-O bond) appear at 602 , 574 (shoulder) and 561 cm^{-1} .¹³ On the other hand, FTIR spectrum of MgAp/RCP matrix exhibits broad and relatively featureless phosphate bands characteristic of ACP.¹⁴ FTIR spectra of Ap/RCP and MgAp/RCP also show the ν_2 vibration mode of CO_3^{2-} group at 873 cm^{-1} indicating the carbonation of the mineral phase.¹⁵ Moreover O-C-O stretching vibration of carboxylate groups from aspartic and glutamic acids containing in RCP sequence appears at 1392 cm^{-1} in the spectrum of RCP (Figure 3b). This peak is blue-shifted for mineralized matrices, appearing at 1398 and 1408 cm^{-1} for Ap/RCP and MgAp/RCP, respectively. Shifts of the symmetric OCO stretching vibrations have been previously associated to the interaction of these functional groups with Ca and/or Mg ions.^{16,17}

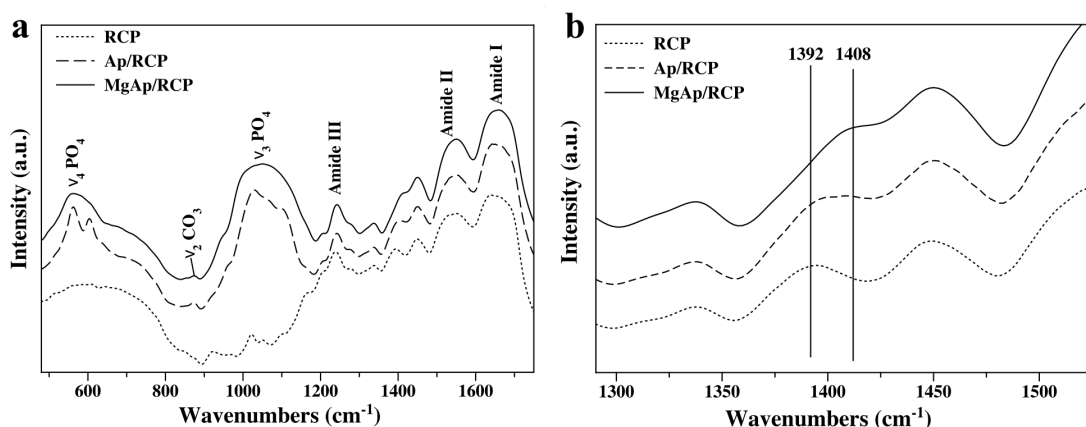


Figure 3. FTIR spectra (a) of non-mineralized (RCP) and mineralized matrices in the absence (Ap/RCP) and in the presence of Mg (MgAp/RCP). (b) FTIR spectra of the matrices in the region of OCO stretching vibration mode.

The surface and structure of designed matrices (RCP, Ap/RCP and MgAp/RCP) were evaluated by SEM (Figure 4). Designed matrices revealed heterogeneous porous structure with pore size ranging from few microns to 200 μm , as showed by SEM images (Figure 4a, b and c). SEM observations of the surface of the matrices at higher magnification showed smooth surface for the non-mineralized RCP matrices (Figure 4d) whereas mineralized matrices provided rough surfaces (Figure 4e and f) due to the integration of the mineral phase. Large mineral aggregates, marked with white arrows in Figure 4e, were found on the surface of Ap/RCP matrices.

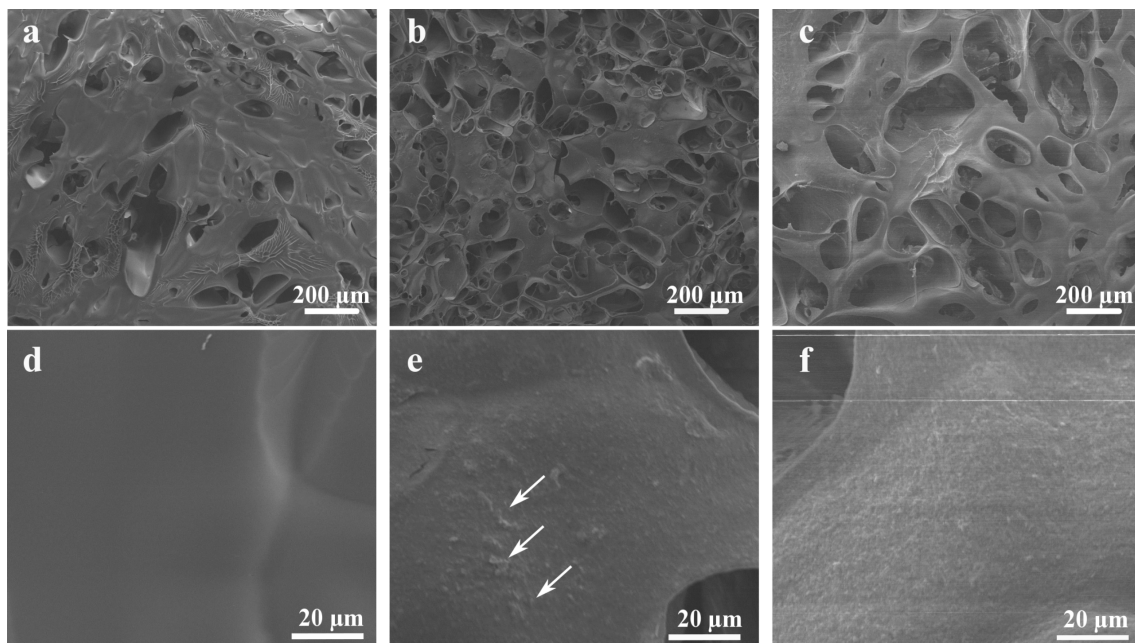


Figure 4. SEM micrographs of RCP (a, d), Ap/RCP (b, e) and MgAp/RCP (c, f) matrices at low (a-c) and higher (d-f) magnification.

SEM observations were confirmed by AFM analysis at the nanoscale level (Figure 5a, b and c). 3D AFM image of Ap/RCP matrix (Figure 5b) showed areas non-covered by the mineral phase (indicated as RCP), isolated needle-like apatite nanocrystals (Ap) and large aggregates of nanocrystals. Conversely, 3D AFM image of MgAp/RCP matrix (Figure 5c) showed a surface completely covered by the mineral phase. This homogeneous mineral distribution provided a lower surface roughness (74.2 ± 18.2 nm) for MgAp/RCP in comparison to that of Ap/RCP (224.1 ± 14.5 nm), as indicated in Figure 5d. Material wettability is reported in Figure 6a. The presence of the mineral phase enhanced the material wettability since Ap/RCP and MgAp/RCP had a slightly lower contact angle than RCP. Nevertheless, all the matrices showed exceptional

swelling capacity (around 600 wt.% of water uptake) without statistical difference between them (Figure 6b).

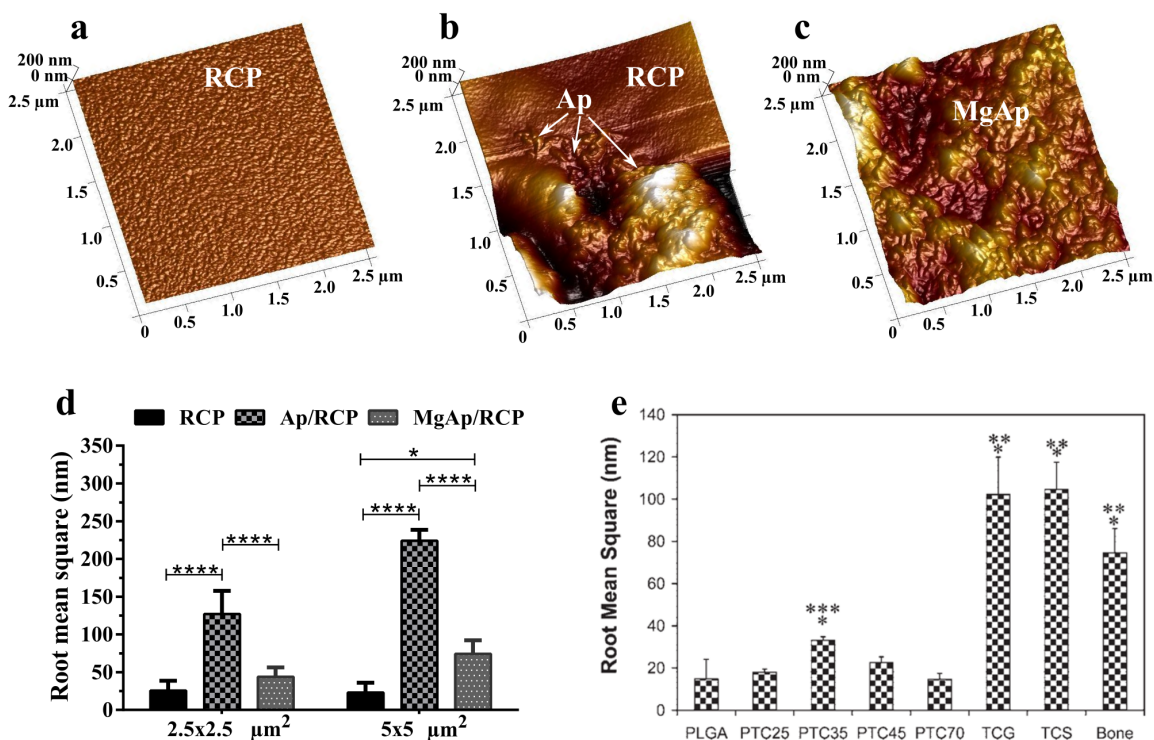


Figure 5. 3D AFM images of the surface of RCP (a), Ap/RCP (b) and MgAp/RCP (c) matrices. d) Mean surface roughness values for each sample measured from two scan areas: 2.5x2.5 μm^2 and 5x5 μm^2 . Data are expressed as mean \pm SD (n=5). *p<0.05; ****p<0.0001. e) Surface roughness of titania/PLGA composites and natural bone reprinted from Liu H. *et al.*,¹⁸ Copyright (2006) with permission of John Wiley & Sons, Inc: Journal of Biomedical Materials Research Part A.

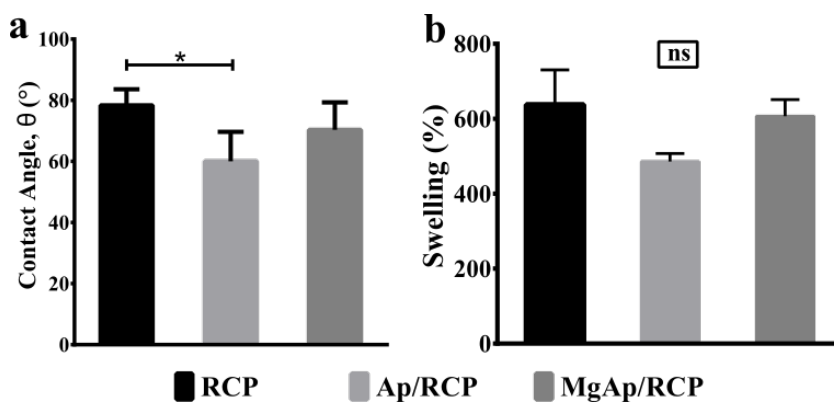


Figure 6. Macroscopic properties of non-mineralized (RCP) and Ap/RCP and MgAp/RCP mineralized matrices: (a) contact angle and (b) swelling capacity (%). Data are expressed as mean \pm SD (n = 3). *p<0.05.

4.4. Discussion

Two main goals are accomplished along this chapter. Firstly, prototype scaffolds were developed by freeze-drying in order to determine the most suitable mineral/organic weight ratio to obtain hybrid scaffolds with homogeneous mineral integration into the organic matrix. Once that min/org weight ratio was selected, hybrid matrices were developed through mineralization in the presence and in the absence of magnesium (Mg) in order to evaluate how Mg incorporation during mineralization can interfere final physic-chemical properties.

As we indicated above, the first goal of this chapter is the preparation of 3D porous scaffolds easily handle and not brittle to touch that show homogeneous mineral distribution along the scaffold. The highest min/org weight ratio prompted to powdered samples (70/30) whereas porous scaffolds were obtained for lower min/org weight ratio values. Homogeneous mineral integration into the organic matrix was only appreciated for scaffold prototype developed for an initial min/org weight ratio 40/60, which is lower than the mineral content in natural bone¹⁹ and the mineral content of mineralized collagen scaffolds.²⁰ A lower homogenous mineral integration into RCP matrix might be associated to the fact that RCP molecules do not self-assembly into large microfibers as collagen does²¹ or due to the lower concentration of charged amino acid groups in RCP molecules when compared to collagen since they play a relevant role in controlling mineral deposition and growth during bone formation.^{22,23} Martin *et al.* indicated that 58% of the mineral in canine whole bone is intrafibrillar, 14% interfibrillar, and 28% from within the gaps between the ends of collagen fibrils.²⁴ Comparing RCP with denatured collagen (gelatin), hybrid scaffolds made of gelatin and calcium phosphate (mineral content in the range of 10-30 wt.%) have showed an up-regulation of the alkaline phosphatase (ALP) and osteocalcin (OC) levels produced by the cells when compared to ALP and OC levels of cells cultured on pure gelatin,²⁵⁻²⁷ indicating the osteoconductive effect of composite scaffolds containing lower mineral content than native bone.

The second goal of this chapter aims at understanding how Mg can affect the interaction between the mineral and RCP and how it can determine the mineral distribution in the organic matrix. FTIR spectra of mineralized matrices showed a shift of $\nu_s\text{OCO}$ modes from aspartic (contained in RGD sequence) and glutamic acid of the RCP sequence with respect to the non-mineralized organic matrix. This shift may be due to the interaction

between negatively charged carboxylate groups of RCP and calcium and/or magnesium ions.²⁸ The higher shift observed for MgAp/RCP could be due to a stronger interaction between the mineral phase and the organic matrix. This can be associated to the fact that Mg sites can coordinate and bind water in a higher extent than Ca, thus leading to a more effective protein adsorption.²⁹

Other highly relevant feature of the mineralization process here proposed is the control on the surface properties of the mineralized matrices. Until now, most of the designed biomimetic scaffolds to support cell and tissue growth have been focused on “bulk properties” such as porosity and mechanical response.³⁰ Nevertheless, biomaterial surface properties play a crucial role in cell response³¹ since they mediate specific protein adsorption before cells adhere on implants, further regulating cell behaviour and dictating tissue regeneration.³² Among biomaterial interfacial properties, it has been claimed that surface roughness affects cellular response, enhancing cell adhesion and proliferation.³³ In this work, relevant differences on mineral distribution and surface roughness of designed materials were attributed to the mineralization protocol. The non-mineralized organic samples (RCP) exhibited smooth surface whereas hybrid matrices showed surfaces with higher roughness due to incorporation of the mineral phase into the organic matrix. We found that MgAp/RCP matrices showed a homogeneous mineral distribution with the surface completely covered by the mineral phase. However, large mineral aggregates, isolated Ap nanocrystals and non-covered regions were observed on the surface of Ap/RCP matrices. The homogeneous mineral distribution found in MgAp/RCP matrices provided mean roughness value closer to that found in biological bone (Figure 5e).³⁴ Recent research has indeed suggested that biomaterials with surface properties similar to that found in bone aids in the formation of new bone at the tissue/biomaterial interface.³⁴ In fact, Webster *et al.* reported significant increases in the initial protein adsorption and subsequent osteoblast adhesion on single-phase nanosized ceramic materials when compared with conventional micrometer-sized ceramic materials.^{34,35} Modifications on surface roughness also imply changes in contact angle.³⁶ Ap/RCP matrices show lower contact angle than MgAp/RCP ones.

4.5. Conclusions

In this chapter, biomimetic mineralization of recombinant collagen peptide (RCP) has been carried out at increasing initial theoretical mineral/organic weight ratio in order to

determine the most suitable mineral content to obtain hybrid scaffolds with homogeneous mineral integration. Scaffold prototype containing a 40 wt.% of mineral was selected as the best condition due to homogeneity of the sample as well as good mineral integration. Then, hybrid matrices with 40 wt.% of mineral content were prepared to evaluate the effect of introduction of magnesium (Mg) during mineralization on the interfacial properties of designed biomaterial. SEM and AFM imaging showed an homogeneous mineral distribution on the RCP matrix mineralized in presence of Mg, which provided a surface roughness similar to that found in bone. Furthermore, hybrid matrices showed exceptional swelling properties. The results indicated that biomimetic mineralization of recombinant collagen peptide is a promising approach for the development of scaffolds for bone regeneration (Chapter 6).

References

1. Salgado, A.J., Coutinho, O.P. and Reis, R.L. Bone tissue engineering: state of the art and future trends. *Macromol Biosci* **4**, 743, 2004.
2. Follet, H., Boivin, G., Rumelhart, C. and Meunier, P. The degree of mineralization is a determinant of bone strength: a study on human calcanei. *Bone* **34**, 783, 2004.
3. Bongio, M., van den Beucken, J.J., Leeuwenburgh, S.C. and Jansen, J.A. Development of bone substitute materials: from 'biocompatible' to 'instructive'. *J Mater Chem* **20**, 8747, 2010.
4. Kim, H.W., Lee, H.H. and Knowles, J. Electrospinning biomedical nanocomposite fibers of hydroxyapatite/poly (lactic acid) for bone regeneration. *J Biomed Mater Res A* **79**, 643, 2006.
5. Mitsak, A.G., Kemppainen, J.M., Harris, M.T. and Hollister, S.J. Effect of polycaprolactone scaffold permeability on bone regeneration in vivo. *Tissue Engineering Part A* **17**, 1831, 2011.
6. Tampieri, A., Celotti, G., Landi, E., Sandri, M., Roveri, N. and Falini, G. Biologically inspired synthesis of bone-like composite: Self-assembled collagen fibers/hydroxyapatite nanocrystals. *J Biomed Mater Res A* **67A**, 618, 2003.
7. Webster, T.J. Nanophase ceramics: The future orthopedic and dental implant material. *Advances in Chemical Engineering: Academic Press*; 2001. pp. 125.
8. Webster, T.J., Schadler, L.S., Siegel, R.W. and Bizios, R. Mechanisms of enhanced osteoblast adhesion on nanophase alumina involve vitronectin. *Tissue Eng* **7**, 291, 2001.
9. Samavedi, S., Whittington, A.R. and Goldstein, A.S. Calcium phosphate ceramics in bone tissue engineering: a review of properties and their influence on cell behavior. *Acta Biomater* **9**, 8037, 2013.
10. Wang, P., Zhao, L., Liu, J., Weir, M.D., Zhou, X. and Xu, H.H. Bone tissue engineering via nanostructured calcium phosphate biomaterials and stem cells. *Bone research* **2**, 14017, 2014.

11. Meirelles, L., Arvidsson, A., Andersson, M., Kjellin, P., Albrektsson, T. and Wennerberg, A. Nano hydroxyapatite structures influence early bone formation. *J Biomed Mater Res A* **87**, 299, 2008.
12. Morris, M.D. and Finney, W.F. Recent developments in Raman and infrared spectroscopy and imaging of bone tissue. *Spectroscopy* **18**, 155, 2004.
13. Koutsopoulos, S. Synthesis and characterization of hydroxyapatite crystals: A review study on the analytical methods. *J Biomed Mater Res* **62**, 600, 2002.
14. Gadaleta, S., Paschalis, E., Betts, F., Mendelsohn, R. and Boskey, A. Fourier transform infrared spectroscopy of the solution-mediated conversion of amorphous calcium phosphate to hydroxyapatite: new correlations between X-ray diffraction and infrared data. *Calcif Tissue Int* **58**, 9, 1996.
15. Antonakos, A., Liarokapis, E. and Leventouri, T. Micro-Raman and FTIR studies of synthetic and natural apatites. *Biomaterials* **28**, 3043, 2007.
16. Klawitter, J. and Hulbert, S. Application of porous ceramics for the attachment of load bearing internal orthopedic applications. *J Biomed Mater Res* **5**, 161, 1971.
17. Rai, R., Keshavarz, T., Roether, J., Boccaccini, A.R. and Roy, I. Medium chain length polyhydroxyalkanoates, promising new biomedical materials for the future. *Mater Sci Eng R* **72**, 29, 2011.
18. Liu, H., Slamovich, E.B. and Webster, T.J. Increased osteoblast functions among nanophase titania/poly (lactide-co-glycolide) composites of the highest nanometer surface roughness. *J Biomed Mater Res A* **78**, 798, 2006.
19. Weiner, S. and Wagner, H.D. The Material Bone: Structure-Mechanical Function Relations. *Annu Rev Mater Sci* **28**, 271, 1998.
20. Roveri, N., Falini, G., Sidoti, M.C., Tampieri, A., Landi, E., Sandri, M. and Parma, B. Biologically inspired growth of hydroxyapatite nanocrystals inside self-assembled collagen fibers. *Materials Science and Engineering C* **23**, 441, 2003.
21. Shoulders, M.D. and Raines, R.T. Collagen structure and stability. *Annu Rev Biochem* **78**, 929, 2009.
22. Landis, W.J., Song, M.J., Leith, A., McEwen, L. and McEwen, B.F. Mineral and Organic Matrix Interaction in Normally Calcifying Tendon Visualized in Three Dimensions by High-Voltage Electron Microscopic Tomography and Graphic Image Reconstruction. *J Struct Biol* **110**, 39, 1993.
23. Glimcher, M.J. and Muir, H. Recent Studies of the Mineral Phase in Bone and Its Possible Linkage to the Organic Matrix by Protein-Bound Phosphate Bonds [and Discussion]. *Philos Trans R Soc Lond B Biol Sci* **304**, 479, 1984.
24. Martin, R.B., Burr, D.B. and Sharkey, N.A. *Skeletal tissue mechanics*: Springer; 1998.
25. Kemeñçe, N. and Bölgen, N. Gelatin-and hydroxyapatite-based cryogels for bone tissue engineering: synthesis, characterization, in vitro and in vivo biocompatibility. *J Tissue Eng Regen Med* 2013.
26. Kim, H.W., Knowles, J.C. and Kim, H.E. Hydroxyapatite and gelatin composite foams processed via novel freeze-drying and crosslinking for use as temporary hard tissue scaffolds. *J Biomed Mater Res A* **72**, 136, 2005.
27. Kim, H.-W., Kim, H.-E. and Salih, V. Stimulation of osteoblast responses to biomimetic nanocomposites of gelatin-hydroxyapatite for tissue engineering scaffolds. *Biomaterials* **26**, 5221, 2005.
28. Byler, D.M. and Farrell, H.M. Infrared spectroscopic evidence for calcium ion interaction with carboxylate groups of casein. *J Dairy Sci* **72**, 1719, 1989.

29. Bertinetti, L., Drouet, C., Combes, C., Rey, C., Tampieri, A., Coluccia, S. and Martra, G. Surface Characteristics of Nanocrystalline Apatites: Effect of Mg Surface Enrichment on Morphology, Surface Hydration Species, and Cationic Environments. *Langmuir* **25**, 5647, 2009.
30. Polo-Corrales, L., Latorre-Esteves, M. and Ramirez-Vick, J.E. Scaffold design for bone regeneration. *J Nanosci Nanotechnol* **14**, 15, 2014.
31. Chang, H.-I. and Wang, Y. Cell responses to surface and architecture of tissue engineering scaffolds: INTECH Open Access Publisher; 2011.
32. Zhang, L. and Webster, T.J. Nanotechnology and nanomaterials: Promises for improved tissue regeneration. *Nano Today* **4**, 66, 2009.
33. Anselme, K. Osteoblast adhesion on biomaterials. *Biomaterials* **21**, 667, 2000.
34. Webster, T.J., Siegel, R.W. and Bizios, R. Nanoceramic surface roughness enhances osteoblast and osteoclast functions for improved orthopaedic/dental implant efficacy. *Scr Mater* **44**, 1639, 2001.
35. Sato, M., Slamovich, E.B. and Webster, T.J. Enhanced osteoblast adhesion on hydrothermally treated hydroxyapatite/titania/poly(lactide-co-glycolide) sol-gel titanium coatings. *Biomaterials* **26**, 1349, 2005.
36. Wenzel, R.N. Surface Roughness and Contact Angle. *J Phys Chem* **53**, 1466, 1949.

Chapter 5: Investigations of different crosslinking approaches of mineralized recombinant collagen peptide

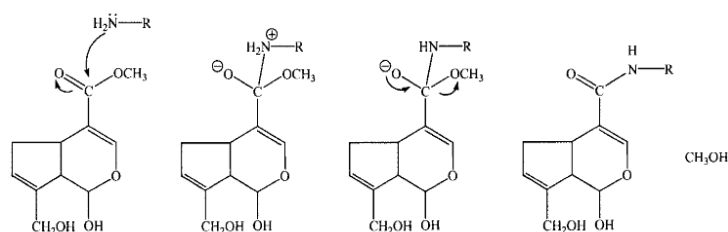
5.1. Introduction

Mineralization of recombinant collagen type I derived peptide (RCP) containing RGD sequences provided hybrid structures with similar physic-chemical features than bone extracellular matrix (ECM). However, one of the main drawbacks of the use of RCP is the fast degradation and total dissolution under physiological conditions. 3D structure for bone regeneration should maintain mechanical stability during *in vivo* bone remodelling and simultaneously undergo degradation to allow the ultimate replacement by newly formed bone.¹ To improve the resistance to the degradation as well as the mechanical performance of different polymers/proteins/peptides used in biomedical field, different crosslinking methodologies have been adopted. The crosslinking methods can be divided in three main groups: i) physical methods (e.g., dehydrothermal treatment (DHT) or ultraviolet and gamma irradiation),²⁻⁴ ii) chemical methods using crosslinking agents such as glutaraldehyde (GA)^{5,6} and diisocyanates, carbodiimides⁷⁻⁹ (e.g., 1-ethyl-3-(3-dimethylamino propyl) carbodiimide hydrochloride (EDC) and *N*-hydroxysuccinimide (NHS)), polyepoxy compounds^{10,11} (e.g., 1,4-butanediol diglycidyl ether (BDDGE) and glycidyl isopropyl ether (PGE)) and acyl azide methods^{12,13} and iii) biological methods^{14,15} (e.g., transglutaminase). Most of the chemical crosslinking agents are highly cytotoxic and may impair the biocompatibility of the crosslinked biomaterials. Therefore, much interest is now directed toward naturally derived crosslinking reagents presenting lower cytotoxicity.

Genipin is an aglycone derived from an iridoid glycoside called geniposide present in fruit of *Gardenia jasminoides* Ellis. It is obtained from its parent compound, geniposide, via enzymatic hydrolysis with β -glucosidase.¹⁶ Several works demonstrated that genipin reacts with materials containing primary amine groups, such as collagen, chitosan, gelatin, peptides and polypeptides, to form covalently crosslinked networks.¹⁷⁻²⁰ It has been proposed that the crosslinking mechanism consists of two reactions, involving different sites on the genipin molecule (Figure 1).²¹ Reaction scheme I corresponds to the nucleophilic substitution reaction that involves the replacement of the ester group on the genipin molecule by a secondary amide linkage. By the time that the ester

substitution occurred, it is believed that the other half of the crosslinked have already formed following reaction scheme 2 (Figure 1).²¹ This reaction starts with an initial nucleophilic attack of the genipin C3 carbon atom from a primary amine group to form an intermediate aldehyde group. The newly formed secondary amine reacts with the aldehyde group to form a heterocyclic compound. Once that the heterocyclic compound has formed, oxygen radical-induced polymerization of genipin occurs, given the sample a blue colour.

Reaction Scheme 1



Reaction Scheme 2

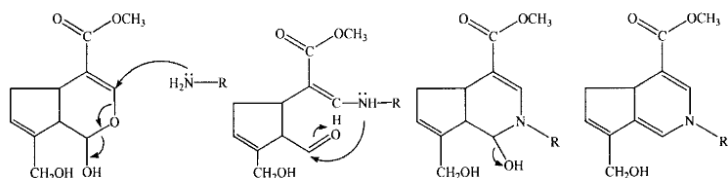


Figure 1. Proposed crosslinking reactions involving genipin and amine groups of collagen-based biomaterials. Reprinted from Butler *et al.*,²¹ Copyright (2003), with permission from Wiley Periodicals, Inc., A Wiley Company: Journal of Polymer Science Part A: Polymer Chemistry.

In vitro evaluation of cytotoxicity of genipin showed that the cellular compatibility of the genipin-fixed tissue was superior to its glutaraldehyde-fixed counterpart.²² It was reported that genipin is about 5,000–10,000 times less cytotoxic than glutaraldehyde.²³ Yao *et al.*²⁴ also found that if the concentration of genipin is lower than 0.5 wt.%, the risk of cytotoxicity could be avoided. Ceramic composed of gelatin and genipin has been tested as bone substitute in rabbit calvarial bone.²⁵ This material showed a good biocompatibility, osteoconductivity and biodegradability with a progressive replacement of the composite for new bone. Indeed, genipin can be used in a broad range of applications including personal care, cosmetics, dietary supplements, packaging, textiles, beverages, foodstuffs, drugs and animal feeds.²⁶

The other crosslinking method evaluated along this chapter is dehydrothermal treatment (DHT). DHT is a thermal process able to induce ester and amide bonds among collagen

Chapter 5: Investigations of different crosslinking

macromolecules via condensation reactions when collagen is subjected to increased temperature ($>98.8^{\circ}\text{C}$) under vacuum (Figure 2). An advantage of DHT crosslinking is that it does not involve the use of cytotoxic reagents.²⁷

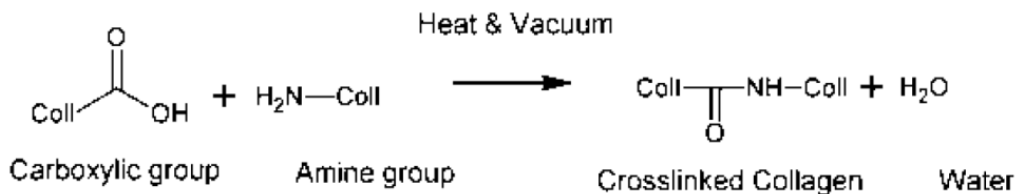


Figure 2. Scheme of reaction during DHT treatment. Reprinted from Haugh *et al.*,²⁷ Copyright (2011), with permission from Mary Ann Liebert, Inc.: Tissue Engineering Part A.

On one hand physical treatment can present lower cytotoxicity but it can also promote lower crosslinking degree. On the other hand, the chemical treatment provides higher crosslinking degree but it can provoke change in the scaffold structure and further cytotoxic effects. The selection of a suitable crosslinking technique for the hybrid RCP scaffolds is the main issue of this chapter.

Herein, we prepared genipin-crosslinked scaffolds by three different methodologies in order to select the most feasible technique and the most suitable genipin concentration. Then, non-mineralized (RCP) and mineralized (Ap/RCP and MgAp/RCP) scaffolds were chemically crosslinked with genipin and compared with the physically crosslinked scaffolds by DHT through the assessment of the crosslinking degree, the degradation rate and the enzymatic resistance of crosslinked scaffolds (described in Chapter 2).

5.2. Methods

The chemical crosslinking with genipin was carried out by three different techniques, as shown in Figure 3:

- a. **Pre-crosslinking:** RCP was crosslinked before mineralization. Genipin was added directly to RCP solution and stirred at 50°C during three hours. After that, mineralization was carried out following the protocol previously described in Chapter 3. After 2 hours of mineralization, the crosslinked-mineralized slurry was freeze-dried.

b. **Post-crosslinking:** RCP was crosslinked after mineralization. RCP mineralization was carried out following the protocol previously described in Chapter 3. After 2 hours of mineralization, genipin solution was added to mineralized slurry, stirred vigorously and kept two days at room temperature. After that, the sample was freeze-dried.

c. **Scaffold crosslinking:** Fabricated scaffolds were crosslinked by immersion in genipin solution. In the case of hybrid scaffolds, firstly mineralization was carried out, then mineralized slurry was freeze-dried and finally mineralized scaffolds were crosslinked by immersion in genipin solution. Then, scaffolds were washed with Milli-Q water and dried into the oven at 40 °C. Considering that RCP is water soluble, genipin concentration as well as composition of genipin solvent were optimized (Table 1).

Pre-Crosslinking:



Post-Crosslinking:



Scaffold Crosslinking:



Figure 3. Different techniques to chemically crosslink scaffold with genipin.

Table 1. Divisions of the conditions of crosslinking of RCP by scaffold immersion into genipin solution.

Genipin concentration (wt.%)	Water/Ethanol
0.05	0/100
0.125	90/10-70/30-50/50-30/70-10/90-0/100
0.25	0/100
0.5	0/100

DHT treatment of RCP scaffolds was carried out at 160 °C for 48 hours under vacuum.²⁸

5.3. Results

5.3.1. Chemical crosslinking with genipin

Figure 4 displays the macroscopic view of the pre- and post-crosslinked mineralized RCP samples. Pre-crosslinked samples (Figure 4a) showed a homogeneous blue colour that may indicate the homogeneity of the sample after mineralization and crosslinking. On the other hand, post-crosslinked samples (Figure 4b) showed the formation of two phases: i) a phase of dark blue colour at the top of the solution mainly composed by crosslinked non-mineralized organic matrix and ii) a phase with yellow-orange colour that may belong to mineralized RCP suspension with lower crosslinking degree. After freeze-drying the slurries, the respective scaffold structure and composition was analysed by SEM and TGA. SEM images of the scaffold surface (at the base-middle zones) showed the presence of larger aggregates in the surface of pre-crosslinked samples whereas homogeneous mineral integration was observed for the post-crosslinked samples. On the other hand, the thermogravimetric analysis indicated a significant heterogeneity for post-crosslinked samples containing only organic phase at the top of the scaffolds (Figure 4c, Post_T). TGA curve of pre-crosslinked samples (Figure 4c) also verified the heterogeneous composition of the obtained hybrid scaffolds with a higher mineral content at the base (~50 wt.%) respect to the top of the scaffold (~30 wt.%).

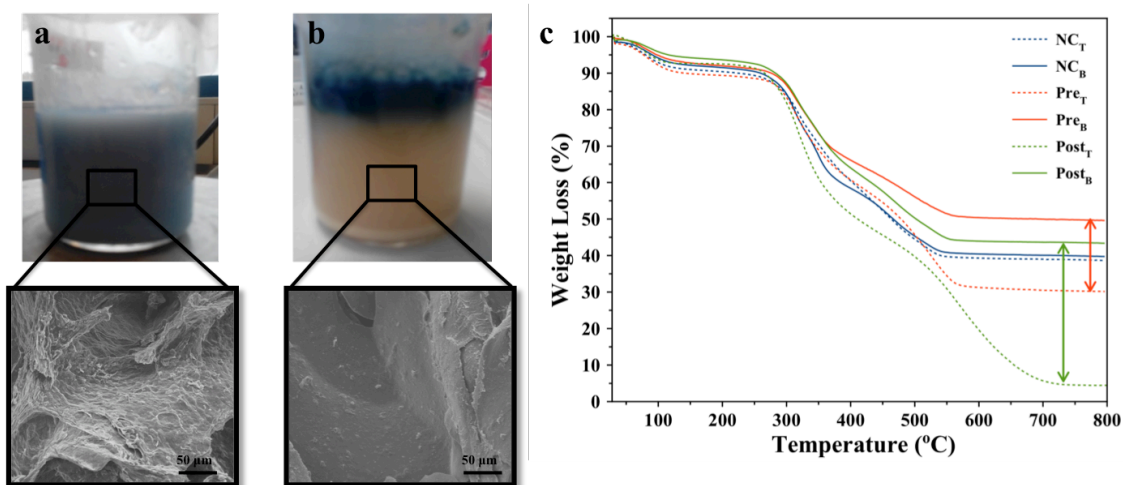


Figure 4. Image of pre (a) and post-crosslinked (b) RCP mineralized slurry before freeze-drying and SEM images of the surface of scaffolds obtained after the freeze-

drying protocol. (c) TGA curves of the top (_T) and base (_B) of non-crosslinked (NC), pre-crosslinked (Pre) and post-crosslinked (Post) hybrid scaffolds.

Taking into account the drawbacks of pre- and post-crosslinking methodologies, we decided to carry out the crosslinking and mineralization individually in a two-step protocol named as scaffold crosslinking (Figure 3). Considering that RCP is water soluble, firstly we evaluated the composition of the genipin solvent to determine the most suitable volume ratio of water/ethanol (v/v) to avoid scaffold dissolution and loose of the structure (Figure 5). Secondly, several concentrations of genipin were assessed (Figure 6). For the first aim, scaffolds were immersed in genipin solutions with fixed genipin concentration (0.125 wt.%) and increasing ethanol contents (Table 1). After 48 hours, scaffolds were completely dissolved for crosslinking experiments in genipin solutions in 10, 30 and 50 % (v/v) of ethanol. For scaffold crosslinking in genipin solution in 70 % (v/v) ethanol, scaffolds degraded partially as indicated the blue colour of genipin solution due to release of RCP molecules that continued to react with genipin (Figure 5). On the other hand, scaffolds crosslinked in genipin solutions in 90 % (v/v) of ethanol kept the macroscopic structure without release of RCP molecules as indicated by transparent colour of the genipin solution (Figure 5). After crosslinking, scaffolds were washed with water and dried into the oven at 40 °C. SEM images of scaffolds before and after crosslinking in genipin solution in 90 % (v/v) of ethanol (Figure 5) indicated no changes in the scaffold structures after crosslinking. It means that it is not necessary a secondary freeze-drying to recover porous structure which simplifies the system for future scale-up of the process.

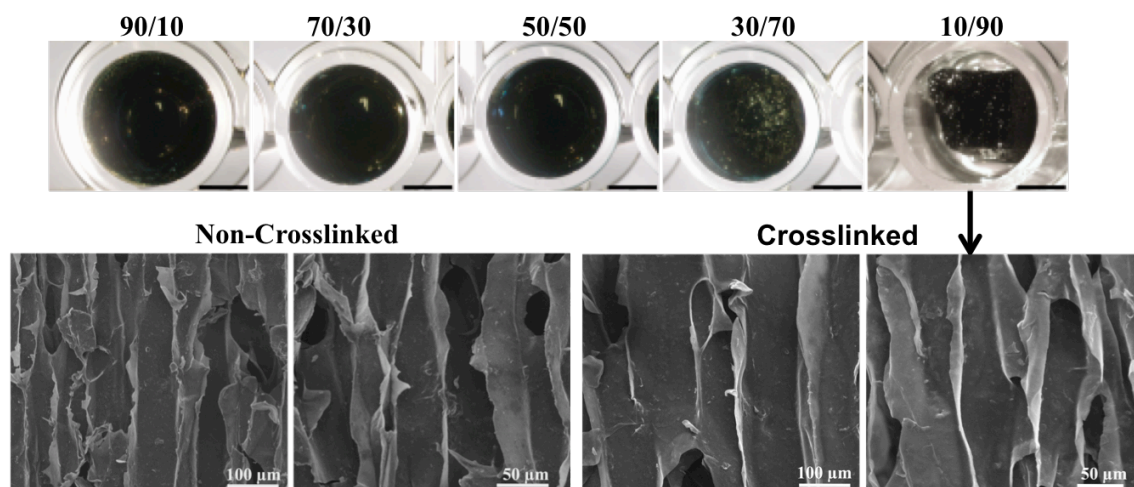


Figure 5. Optical microscopy images of crosslinked structures after 48 hours immersed in genipin (0.125 wt.%) aqueous solution with increasing ethanol content (% v/v).

Chapter 5: Investigations of different crosslinking

Scale bar: 500 μ m. SEM images of RCP scaffolds before and after crosslinking by immersion in genipin (0.125 wt.%) solution in aqueous/ethanol volume ratio 10/90.

The next step is to evaluate the most suitable genipin concentration. Scaffolds were crosslinked by immersion in 2 mL of ethanol (90 % v/v) containing different concentrations of genipin (0.05, 0.125, 0.25 and 0.5 wt.%). After 24 hours, scaffolds immersed in solution with the lowest genipin concentration showed yellow colour whereas the rest of scaffolds showed dark blue colour (Figure 6a). After 48 hours, all the scaffolds showed dark blue colour. The dark-blue coloration of the scaffolds is associated with the oxygen radical-induced polymerization of genipin as well as its reaction with amino groups.²¹

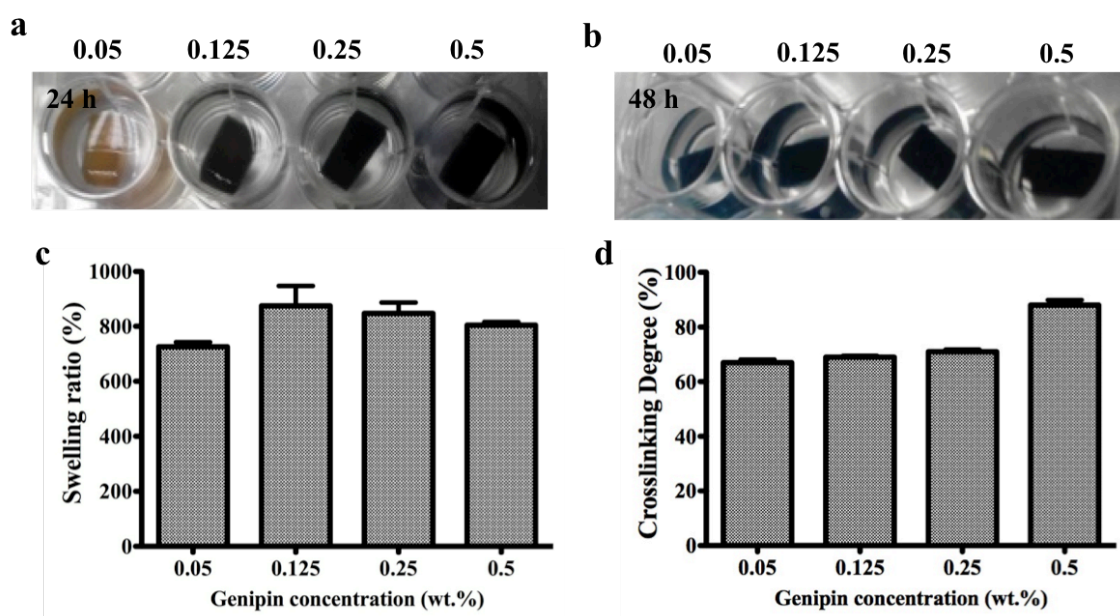


Figure 6. Images of scaffolds after 24 hours (a) and 48 hours (b) of crosslinking in increasing genipin concentrations in aqueous ethanol solution (90 % v/v ethanol); (c) Swelling capacity of crosslinked scaffolds at increasing genipin concentrations and (d) crosslinking degree of RCP scaffolds after crosslinking with increasing genipin concentrations. Data are expressed as mean \pm SD (n=3).

After 48 hours of crosslinking, scaffolds were washed to eliminate non-reacted genipin and dried. The swelling capacity of crosslinked scaffolds with different genipin concentrations upon exposure to PBS (pH 7.4) at 37 °C for 24 hours is shown in Figure 6c. It was found that RCP scaffolds crosslinked with the lowest genipin concentration showed the lowest capacity to absorb water. Figure 6d displays the extent of crosslinking of the scaffolds calculated by TNBS assay. The crosslinking degree of the scaffolds crosslinked with different genipin concentrations was roughly the same

(around 70%) except for the scaffolds crosslinked with the highest genipin concentration that showed a higher extent of crosslinking (88%). Considering the swelling properties, the crosslinking extent and the possible cytotoxic effects due to the use of high genipin concentrations, 0.125 wt% of genipin in 90% (v/v) ethanol solution was selected as crosslinking protocol for the further studies.

5.3.2. Investigations of different crosslinking of RCP hybrid scaffolds

Chemical crosslinking technique with genipin is compared respect to physical crosslinking by DHT through the assessment of the crosslinking degree, the stability under physiological conditions and the enzymatic resistance of crosslinked scaffolds. This study is carried out for the three scaffold compositions evaluated until now: non-mineralized scaffolds (RCP), mineralized scaffolds (Ap/RCP) and mineralized in the presence of magnesium (MgAp/RCP).

The figure 7 displays the extent of crosslinking of RCP, Ap/RCP and MgAp/RCP scaffolds crosslinked by the two different methodologies. The scaffolds crosslinked with genipin showed a higher crosslinking extent when compared to scaffolds with same composition, but crosslinked by DHT ($p < 0.0001$). Respect to scaffold compositions, non-mineralized scaffolds (RCP) showed the highest crosslinking extent for both crosslinking techniques whereas MgAp/RCP scaffolds showed the lowest value.

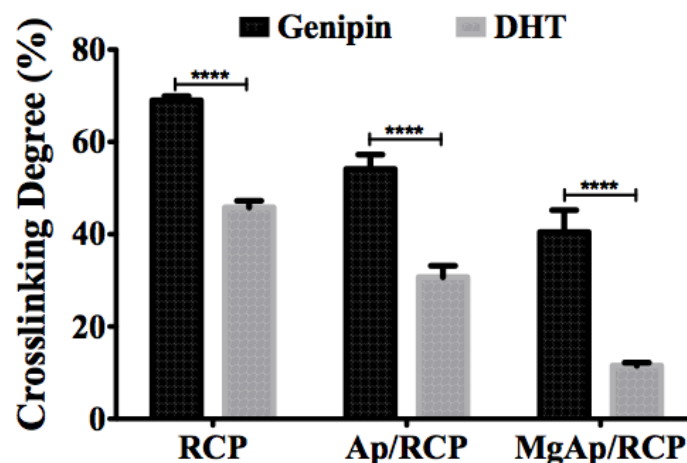


Figure 7. Crosslinking degree of three scaffold compositions (RCP, Ap/RCP and MgAp/RCP) crosslinked by two different techniques: genipin and DHT. Data are expressed as mean \pm SD (n=3). ****p<0.0001.

The stability of the crosslinked scaffolds under physiological conditions was evaluated up to 28 days in PBS at 37 °C (Figure 8). From macroscopic observation, there was no loss of shape or weakening of structural architecture of the scaffolds after this period. RCP scaffolds crosslinked by DHT showed negative weight loss due to gain of weight for the precipitation of salts that were not well removed during washing of the scaffold. MgAp/RCP scaffolds crosslinked by DHT or genipin showed the highest weight loss (7.9 ± 0.6 and 10.2 ± 3.6 wt.%, respectively) after 28 days in PBS. The degradation test did not indicate relevant differences on the weight loss of scaffolds with same composition differing on crosslinking methodology. Overall, more than 90 wt.% of weight of scaffolds remained after 28 days in PBS as well as its structure did not suffer any alteration, indicating the effectiveness of crosslinking techniques.

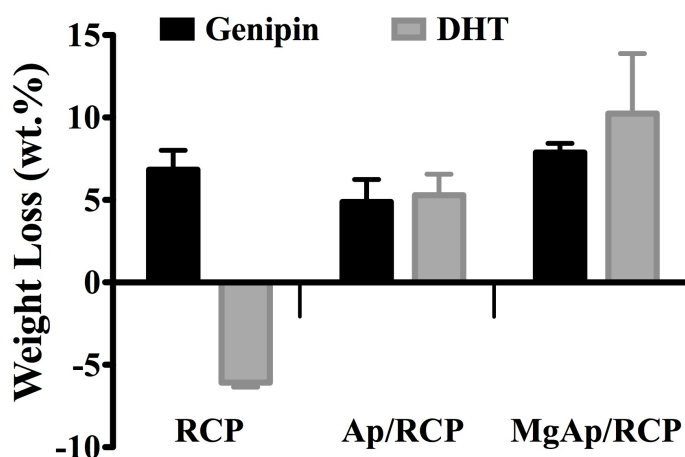


Figure 8. Weight loss of crosslinked scaffolds (RCP, Ap/RCP and MgAp/RCP) after 28 days of immersion in PBS medium at 37 °C. Data are expressed as mean \pm SD (n=3).

In vitro degradation studies were carried out in the presence of bacterial collagenase from *Clostridium histolyticum*. Figure 9a displays the weight loss of crosslinked scaffolds after 1 day in collagenase solution. The RCP release to the medium due to scaffold degradation was also evaluated by protein quantification (Figure 9b). RCP and MgAp/RCP scaffolds crosslinked with genipin were completely dissolved after 24 hours in collagenase solution whereas Ap/RCP scaffolds crosslinked with genipin kept the structure presenting a weight loss of 11.4 ± 2.4 wt.%. This weight loss is associated to release of RCP to the medium, which is around the 40% of the organic component of the scaffold. Ap/RCP scaffolds crosslinked by DHT showed a higher resistance to

enzymatic degradation compared to genipin, as indicated the negative weight loss and the lower protein release to the medium after 24 hours in collagenase solution. Unlike RCP scaffolds crosslinked with genipin, RCP scaffolds crosslinked by DTH showed a higher resistance to enzymatic degradation with a small percentage of RCP molecules released to the medium (Figure 9b). On the other hand, MgAp/RCP scaffolds crosslinked by DHT showed a completely degradation (100 wt.% weight loss) after 24 hours in collagenase solution (Figure 9a).

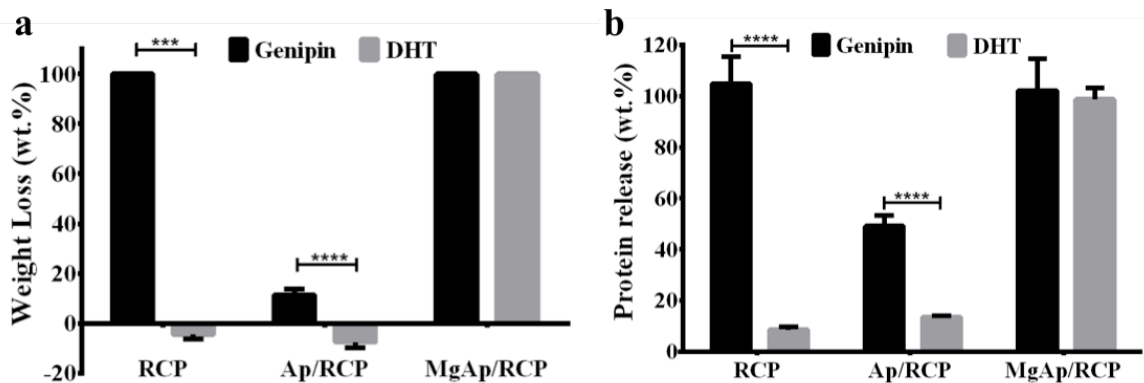


Figure 9. Enzymatic degradation of crosslinked scaffolds after 24 hours in Tris-HCl solution containing collagenase: (a) weight loss and (b) protein release. Data are expressed as mean \pm SD (n=3). *** p<0.001 and ****p<0.0001.

5.4. Discussion

An ideal scaffold for bone tissue engineering should maintain the structure and mechanical stability in order to guide the development of new bone formation and simultaneously it might present a suitable biodegradation to be absorbed by the surrounding tissue allowing the ultimate replacement by new formed bone without the need for surgical removal. The aim of this chapter is to investigate the crosslinking of RCP molecules in order to enhance stability of scaffolds under physiological conditions for the long-term biomedical applications. Two different crosslinking methodologies are evaluated: genipin, a natural chemical crosslinking agent with low cytotoxicity and dehydrothermal crosslinking, previously used for the crosslinking of RCP²⁸ and also for crosslinking of hybrid scaffolds.^{8,29}

In previous studies, the crosslinking of collagen/gelatin biomaterials with genipin has been carried out by different methodologies: i) scaffold crosslinking by immersion of

scaffold in genipin solution in PBS and the further freeze-drying,³⁰ ii) gel-crosslinking by immersion of gelatin hydrogel (4 °C) in genipin solution³¹ and iii) mixing crosslinking³² by adding genipin solution to polymer and keeping under stirring for a specific time interval. Despite the fact that most of hybrid scaffolds developed for bone regeneration were crosslinked, low number of works has investigated how the mineral phase can affect to the crosslinking reaction.

In this study, three different methodologies have been evaluated for chemical crosslinking of RCP with genipin. We have proposed the mixing crosslinking by adding genipin to RCP solution before the mineralization (pre-crosslinking) in order to have more available amine groups for the crosslinking. However, after freeze-drying, hybrid scaffolds showed heterogeneous composition and the formation of larger aggregates that may indicate that pre-crosslinking interfered in the mineralization of RCP molecules. To overcome this shortcoming, genipin was added after RCP mineralization (post-crosslinking). However, during crosslinking reaction (48 hours), mineral phase tend to sediment while genipin mainly reacted with non-mineralized RCP molecules present at the top triggering to the formation of a two-phase composite material. Therefore, and considering the drawbacks of mixing crosslinking, we decided to investigate the scaffold crosslinking by immersion in genipin solution. Considering that RCP is water soluble, genipin was dissolved in aqueous solutions at increasing ethanol content. We selected genipin solution in 90% (v/v) ethanol for the crosslinking of scaffolds since scaffolds kept the structure and did not dissolve after 48 hours of crosslinking, avoiding a secondary freeze-drying process. The other advantage of this method is the possibility of washing the scaffolds after the crosslinking procedure in order to remove the non-reacted genipin that can promote cytotoxic effect of the designed biomaterial. Respect to the concentration of genipin, RCP scaffolds crosslinked by immersion in genipin solution (0.125 wt.%) provided a 70% of crosslinking extent, similar to the crosslinking extent on genipin-crosslinked chitosan/collagen³³ or gelatin¹⁷ scaffolds/films. The crosslinked scaffolds with these parameters also showed exceptional swelling properties.

The next aim is to compare the chemical *versus* the physical crosslinking of hybrid scaffolds. For the three scaffold compositions (RCP, Ap/RCP and MgAp/RCP), the highest extent of crosslinking was achieved for the scaffolds crosslinked with genipin. A lower extent of crosslinking for scaffolds crosslinked by DHT may be related to the fact that DHT is a zero-length crosslinking in which amide bonds are directly formed

between adjacent amine and carboxylic groups without any bridging molecule being incorporated in the network.³⁴ On the other hand, genipin may bridge between peptide chains that have a distance up to 1.6-2.5nm, by introducing a dimeric genipin-spacer with a cyclic structure. Moreover, genipin molecules may be polymerized before crosslinking amino groups, by introducing an oligomeric-genipin spacer.³⁵

For both crosslinking methodologies, mineralized scaffolds showed lower extent of crosslinking compared to non-mineralized ones. This effect can be associated to the presence of the mineral phase since calcium and phosphate ions interact electrostatically with carboxylic and amine groups of RCP, reducing the number of amine and carboxylic groups available for the crosslinking reaction. In fact, MgAp/RCP scaffolds crosslinked by DHT showed the lowest extent of crosslinking that can be associated to a stronger interaction (more than in Ap/RCP scaffolds) between carboxylic groups of RCP and calcium and magnesium ions of the mineral phase (as previously demonstrated in chapter 4) hindering the crosslinking reaction. Lower crosslinking extent explained a higher degradation of MgAp/RCP scaffolds under physiological conditions. In general, all the scaffold compositions crosslinked by genipin or DHT showed good stability under physiological conditions (weight loss <10wt.%).

On the other hand, the enzymatic resistance of crosslinked scaffolds seemed not to be dependent on the crosslinking extent. Scaffolds with the highest crosslinking extent (RCP crosslinked with genipin) showed a completely degradation after 24 hours in collagenase solution whereas crosslinked Ap/RCP scaffolds (with lower extent of crosslinking than RCP scaffolds) showed the highest enzymatic resistance. These results are contrary to previous studies in literature that indicated that chemical crosslinking (EDC/NHS) showed higher enzymatic resistance than physical crosslinking techniques.⁸

5.5 Conclusions

In this study, crosslinking of hybrid structures have been carried out by two different techniques, genipin and DHT. The chemical crosslinking with genipin has been set-up in order to avoid interfering the mineralization mechanism of RCP. Genipin concentration as well as genipin solvent has been selected taking into account the removal of a secondary freeze-drying process, the crosslinking degree and the water uptake capacity of designed scaffolds. The highest extent of crosslinked was achieved for scaffolds (independently of the scaffold composition) crosslinked with genipin.

Nevertheless, the results indicated that the presence of the mineral phase might hinder the crosslinking reaction since lower crosslinking degree was obtained for hybrid scaffolds. Even if crosslinked scaffolds either by genipin or DHT showed a good stability under physiological conditions, the scaffolds crosslinked by DHT were endowed with a higher enzymatic resistance. The results highlight, for the first time, the effect of the mineral phase hindering the crosslinking reactions and therefore diminishing scaffold stability. In this case, due to higher enzymatic resistance, DHT was selected as crosslinking methods of RCP hybrid scaffolds for bone regeneration.

References

1. Wu, S., Liu, X., Yeung, K.W., Liu, C. and Yang, X. Biomimetic porous scaffolds for bone tissue engineering. *Mater Sci Eng R* **80**, 1, 2014.
2. Tierney, C.M., Haugh, M.G., Liedl, J., Mulcahy, F., Hayes, B. and O'Brien, F.J. The effects of collagen concentration and crosslink density on the biological, structural and mechanical properties of collagen-GAG scaffolds for bone tissue engineering. *J Mech Behav Biomed Mater* **2**, 202, 2009.
3. Weadock, K.S., Miller, E.J., Keuffel, E.L. and Dunn, M.G. Effect of physical crosslinking methods on collagen - fiber durability in proteolytic solutions. *J Biomed Mater Res* **32**, 221, 1996.
4. Drexler, J.W. and Powell, H.M. Dehydrothermal crosslinking of electrospun collagen. *Tissue Engineering Part C: Methods* **17**, 9, 2010.
5. Damink, L.O., Dijkstra, P., Van Luyn, M., Van Wachem, P., Nieuwenhuis, P. and Feijen, J. Glutaraldehyde as a crosslinking agent for collagen-based biomaterials. *J Mater Sci Mater Med* **6**, 460, 1995.
6. Chang, M.C. and Tanaka, J. FT-IR study for hydroxyapatite/collagen nanocomposite cross-linked by glutaraldehyde. *Biomaterials* **23**, 4811, 2002.
7. Li, J., Ren, N., Qiu, J., Jiang, H., Zhao, H., Wang, G., Boughton, R.I., Wang, Y. and Liu, H. Carbodiimide crosslinked collagen from porcine dermal matrix for high-strength tissue engineering scaffold. *Int J Biol Macromol* **61**, 69, 2013.
8. Kozłowska, J. and Sionkowska, A. Effects of different crosslinking methods on the properties of collagen–calcium phosphate composite materials. *Int J Biol Macromol* **74**, 397, 2015.
9. Pieper, J., Hafmans, T., Veerkamp, J. and Van Kuppevelt, T. Development of tailor-made collagen–glycosaminoglycan matrices: EDC/NHS crosslinking, and ultrastructural aspects. *Biomaterials* **21**, 581, 2000.
10. Tampieri, A., Sandri, M., Landi, E., Pressato, D., Francioli, S., Quarto, R. and Martin, I. Design of graded biomimetic osteochondral composite scaffolds. *Biomaterials* **29**, 3539, 2008.
11. Nicoletti, A., Fiorini, M., Paolillo, J., Dolcini, L., Sandri, M. and Pressato, D. Effects of different crosslinking conditions on the chemical–physical properties of a novel bio-inspired composite scaffold stabilised with 1,4-butanediol diglycidyl ether (BDDGE). *J Mater Sci Mater Med* **24**, 17, 2013.
12. Petite, H., Rault, I., Huc, A., Menasche, P. and Herbage, D. Use of the acyl azide method for cross - linking collagen - rich tissues such as pericardium. *J Biomed Mater Res* **24**, 179, 1990.

13. Anselme, K., Petite, H. and Herbage, D. Inhibition of Calcification In Vivo by Acyl Azide Cross-Linking of a Collagen-Glycosaminoglycan Sponge. *Matrix* **12**, 264, 1992.
14. Orban, J.M., Wilson, L.B., Kofroth, J.A., El - Kurdi, M.S., Maul, T.M. and Vorp, D.A. Crosslinking of collagen gels by transglutaminase. *J Biomed Mater Res A* **68**, 756, 2004.
15. Chen, R.-N., Ho, H.-O. and Sheu, M.-T. Characterization of collagen matrices crosslinked using microbial transglutaminase. *Biomaterials* **26**, 4229, 2005.
16. Carmona, M., Zalacain, A., Sánchez, A.M., Novella, J.L. and Alonso, G.L. Crocetin esters, picrocrocine and its related compounds present in *Crocus sativus* stigmas and *Gardenia jasminoides* fruits. Tentative identification of seven new compounds by LC-ESI-MS. *J Agric Food Chem* **54**, 973, 2006.
17. Bigi, A., Cojazzi, G., Panzavolta, S., Roveri, N. and Rubini, K. Stabilization of gelatin films by crosslinking with genipin. *Biomaterials* **23**, 4827, 2002.
18. Yan, L.P., Wang, Y.J., Ren, L., Wu, G., Caridade, S.G., Fan, J.B., Wang, L.Y., Ji, P.H., Oliveira, J.M. and Oliveira, J.T. Genipin - cross - linked collagen/chitosan biomimetic scaffolds for articular cartilage tissue engineering applications. *J Biomed Mater Res A* **95**, 465, 2010.
19. Chiono, V., Pulieri, E., Vozzi, G., Ciardelli, G., Ahluwalia, A. and Giusti, P. Genipin-crosslinked chitosan/gelatin blends for biomedical applications. *J Mater Sci Mater Med* **19**, 889, 2008.
20. Cheng, N.-C., Estes, B.T., Young, T.-H. and Guilak, F. Genipin-crosslinked cartilage-derived matrix as a scaffold for human adipose-derived stem cell chondrogenesis. *Tissue engineering Part A* **19**, 484, 2012.
21. Butler, M.F., Ng, Y.F. and Pudney, P.D. Mechanism and kinetics of the crosslinking reaction between biopolymers containing primary amine groups and genipin. *J Polym Sci, Part A: Polym Chem* **41**, 3941, 2003.
22. Sung, H.-W., Huang, R.-N., Huang, L.L. and Tsai, C.-C. In vitro evaluation of cytotoxicity of a naturally occurring cross-linking reagent for biological tissue fixation. *J Biomater Sci, Polym Ed* **10**, 63, 1999.
23. Nishi, C., Nakajima, N. and Ikada, Y. In vitro evaluation of cytotoxicity of diepoxy compounds used for biomaterial modification. *J Biomed Mater Res A* **29**, 829, 1995.
24. Yao, C.H., Liu, B.S., Hsu, S.H., Chen, Y.S. and Tsai, C.C. Biocompatibility and biodegradation of a bone composite containing tricalcium phosphate and genipin crosslinked gelatin. *J Biomed Mater Res A* **69**, 709, 2004.
25. Yao, C.-H., Liu, B.-S., Hsu, S.-H. and Chen, Y.-S. Calvarial bone response to a tricalcium phosphate-genipin crosslinked gelatin composite. *Biomaterials* **26**, 3065, 2005.
26. Wu, S. and Horn, G. Genipin-rich material and its use. Google Patents; 2015.
27. Haugh, M.G., Murphy, C.M., McKiernan, R.C., Altenbuchner, C. and O'Brien, F.J. Crosslinking and mechanical properties significantly influence cell attachment, proliferation, and migration within collagen glycosaminoglycan scaffolds. *Tissue Engineering Part A* **17**, 1201, 2011.
28. Parvizi, M., Plantinga, J.A., van Speuwel - Goossens, C.A., van Dongen, E.M., Kluijtmans, S.G. and Harmsen, M.C. Development of recombinant collagen - peptide - based vehicles for delivery of adipose - derived stromal cells. *J Biomed Mater Res A* **104**, 503, 2016.

29. Sarikaya, B. and Aydin, H.M. Collagen/Beta-Tricalcium Phosphate Based Synthetic Bone Grafts via Dehydrothermal Processing. *BioMed Research International* **2015**, 9, 2015.
30. Sung, H.-W., Chang, W.-H., Ma, C.-Y. and Lee, M.-H. Crosslinking of biological tissues using genipin and/or carbodiimide. *Journal of Biomedical Materials Research Part A* **64A**, 427, 2003.
31. Sundararaghavan, H.G., Monteiro, G.A., Lapin, N.A., Chabal, Y.J., Miksan, J.R. and Shreiber, D.I. Genipin - induced changes in collagen gels: Correlation of mechanical properties to fluorescence. *Journal of Biomedical Materials Research Part A* **87**, 308, 2008.
32. Mu, C., Zhang, K., Lin, W. and Li, D. Ring-opening polymerization of genipin and its long-range crosslinking effect on collagen hydrogel. *Journal of Biomedical Materials Research - Part A* **101 A**, 385, 2013.
33. Bi, L., Cao, Z., Hu, Y., Song, Y., Yu, L., Yang, B., Mu, J., Huang, Z. and Han, Y. Effects of different cross-linking conditions on the properties of genipin-cross-linked chitosan/collagen scaffolds for cartilage tissue engineering. *J Mater Sci Mater Med* **22**, 51, 2011.
34. Madaghiele, M., Calò, E., Salvatore, L., Bonfrate, V., Pedone, D., Frigione, M. and Sannino, A. Assessment of collagen crosslinking and denaturation for the design of regenerative scaffolds. *J Biomed Mater Res A* **104**, 186, 2016.
35. Sung, H.W., Chang, W.H., Ma, C.Y. and Lee, M.H. Crosslinking of biological tissues using genipin and/or carbodiimide. *J Biomed Mater Res A* **64**, 427, 2003.

Chapter 6: Fabrication of 3D isotropic hybrid scaffolds through freeze-drying and evaluation of their osteoinductive potential

6.1. Introduction

The previous work was focused on the study of biomineralization of recombinant collagen peptide (RCP) in order to achieve chemical composition similar to bone. For this purpose, the introduction of foreign ions such as magnesium was carried out to improve osteoinductivity. On the other hand, for bone tissue engineering, the optimization of scaffold structure has also a large impact on the final outcome. Scaffolds must encourage the diffusion of cells and nutrients while maintaining adequate mechanical properties.¹ Moreover, scaffolds should be biocompatible and meet biodegradability at a commensurate rate with remodelling.

The porosity of a material is defined as the percentage of void space in a solid² and it is a morphological property that is independent of the material. In bone tissue regeneration it has been proved that more tissue ingrowth and new bone formation occurred in the areas with higher porosity after implantation in rabbit craniums.³ Moreover, the pores are necessary for bone tissue formation because they allow cell migration and proliferation from surrounding bone tissues to the inner areas of the scaffolds, as well as the vascularization.⁴ Pore size greater than 200 μm has been proposed as the minimum required for bone formation and capillary innervation, with 400 μm as an upper limit due to mechanical stability.^{1,5,6} Furthermore, the interconnections between pores within the scaffold structure are also an important aspect of porosity, and an interconnect size below 100 μm restricts bone regeneration.⁷ Bone-like scaffold can be generally divided into two groups: sponge-like scaffold mimicking trabecular bone consisting in an isotropic structure that exhibits high porosity and parallel aligned pore scaffold resembling cortical bone.

Several technologies have been used to create porosity in a biomaterial, such as salt leaching, gas foaming, phase separation, ice-templating and sintering.⁸ The ice-templating includes any technique that utilizes ice to form a three-dimensional structure (i.e., freeze-drying and freeze casting). The technique consists in the freezing of a water-based solution that begins on ice nucleation within the solution and the

concentration of the solute in the regions between the growing crystals. Then, the ice is removed via sublimation and the solute remains in a porous structure that can be either isotropic or anisotropic. In fact, the final porous structure relies on the variables that influence ice nucleation and growth (Figure 1). The type and concentration of solutes within the solution and the set cooling rate before freezing can be altered during nucleation. After nucleation, crystal growth and annealing processes, such as Ostwald ripening, determine the features of the final scaffold. Several parameters such as set freezing temperature, freezing rate as well as concentration of solute will affect ice crystal growth and so the final scaffold structure.⁹

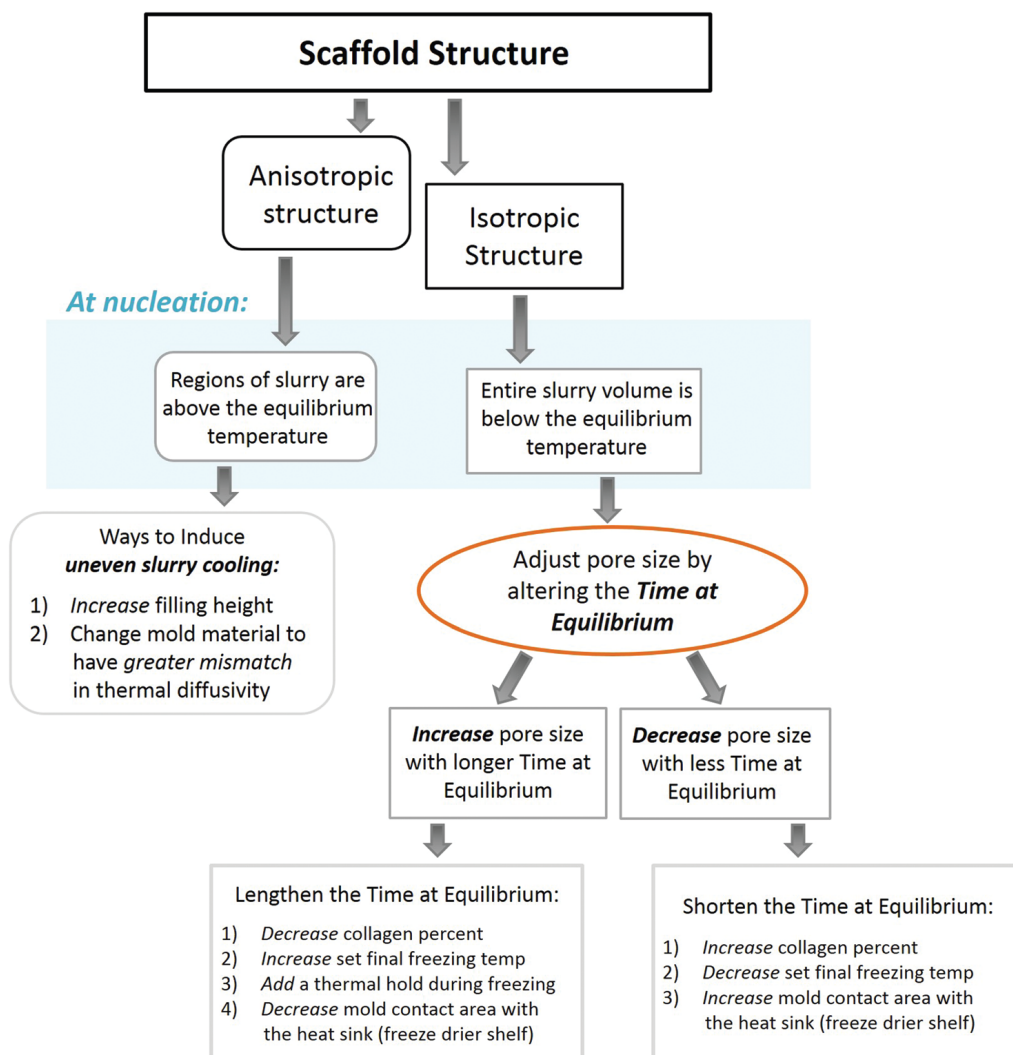


Figure 1. A flow chart summarizing the key points for the design of scaffold structure and the variables of the process that allow tailoring the scaffold porosity. Reprinted from Pawelec *et al.*,⁹ Copyright (2014) with permission from AIP Publishing LLC: Applied Physics Reviews.

The objective of the present chapter is to design bioactive, biofunctional and biodegradable 3D scaffolds for bone tissue regeneration through biomimetic mineralization of RCP and freeze-drying. We focused on the design of sponge-like scaffold with isotropic and high porosity mimicking cancellous bone. The effect of mineral phase on scaffold pore size, porosity, permeability and mechanical properties was evaluated. Furthermore, the *in vitro* kinetic degradation of mineralized scaffolds was evaluated to determine the ion release (Ca^{2+} and Mg^{2+}) to the cell medium since they might affect to cellular behaviour.¹⁰ The ultimate point, the *in vitro* response of mesenchymal stem cells (MSCs) to the biochemical and biophysical cues provided to the scaffolds by biomimetic mineralization is investigated in terms of cell adhesion, proliferation, migration and further expression of osteogenic related markers.

6.2. Methods

6.2.1. Scaffold preparation

Firstly, the conventional (without magnesium) mineralization of RCP was carried out as previously described in Chapter 3 (same preparation than RCPAp sample). Then, mineralized slurry was freeze-dried to obtain 3D structures. As we described above, several parameters can be adjusted during the freezing process in order to obtain isotropic porous structure with suitable pore size. Herein, we evaluated:

- Mould: Teflon mould or well-plate. Teflon mould has a thicker bottom part that restricts the thermal conductivity prompting different thermal profile inside the slurry affecting nucleation and growth of ice and so pore structure.
- Freezing temperature: at higher freezing temperature, larger pores are obtained.
- Solid content: Higher solid content prompts to dense scaffolds with lower porosity.

The frozen samples were freeze-dried with a heating ramp of 5°C/h under vacuum (0.1 mbar) (5Pascal, Cinquepascal srl, Italy). The porous structures obtained under the conditions (summarized in Table 1) were assessed by SEM. Once that the conditions of freeze-drying have been selected, 3D isotropic scaffolds of three different compositions were developed: non-mineralized ones (RCP), mineralized in the absence of magnesium (Ap/RCP) and mineralized in the presence of magnesium (MgAp/RCP). Cylindrical scaffolds of 8 mm in diameter and 5 mm of height were obtained by cutting with a

biopsy puncher (HS Biopsy punch 8 mm, HShospitalService, Italy). Then, scaffold stability and degradability rate was adjusted by physical crosslinking *via* dehydrothermal treatment at 160 °C for 48 hours under vacuum (0.001 mbar).¹¹ All scaffolds were sterilized by autoclave before *in vitro* degradation studies and *in vitro* tests.

Table 1. Variables and parameters tested for the design of isotropic porous scaffolds through freeze-drying of mineralized slurry.

Mould	T_{freezing}, °C	Solid Content, wt.%
Teflon	-80	12.5
		10.0
	-40	12.5
		10.0
	-20	12.5
		10.0
Well-Plate	-40	12.5
		10.0
	-20	12.5
		10.0
		7.0

6.2.2. Cell culture and cell seeding on scaffolds

Mouse mesenchymal stem cells (C57BL/6) (MSCs), purchased from Invitrogen (Carlsbad, CA), were cultured in standard tissue culture flask and maintained in standard cell culture Dulbecco Modified Eagle’s Medium (DMEM, Gibco) supplemented with 10% (v/v) fetal bovine serum (FBS) and 1% (v/v) penicillin/streptomycin (Pen/Strep; 100 U ml⁻¹/100 µg ml⁻¹) at 37 °C with 5% CO₂. Cells were detached from culture flasks by trypsinization, centrifuged and resuspended. Cell number and viability were assessed with the trypan-blue dye exclusion test. Before cell seeding, sterilized scaffolds were pre-incubated overnight with standard cell culture medium (1.5 mL). Then, the scaffolds were replaced in a 24-well plate and each one was seeded by carefully dropping 30 µL of cell suspension containing 5.0 x 10⁴ cells onto the upper surface, allowing cell attachment for 30 min at 37 °C with 5% CO₂ before adding 1.5 ml of cell culture medium. MSCs were incubated in osteogenic medium consisting in α -MEM media supplemented with 10% (v/v) FBS, 1% (v/v) Pen/Strep, 10 mM β -glicerofosfato, 50 µg/ml L-ascorbic acid and 100 nM

dexamethasone and under standard conditions (37 °C, 5% CO₂) for up to 28 days (time points: 1, 3, 7, 14, 21 and 28 days). Culture medium was partially changed every three days. All the cell-handling procedures were performed in a sterile laminar flow hood. Cell viability and proliferation, cell morphology, cell migration, gene expression by quantitative real-time polymerase chain reaction, western blot analysis and immunofluorescence, were carried out as described in chapter 2.

6.3. Results

6.3.1. Design of 3D structures through freeze-drying

Table 2 shows the SEM images of the longitudinal and transversal section from the scaffolds fabricated in Teflon mould using different freezing temperatures. The increase of the pore size due to the increasing final freezing temperature was clearly evident (see SEM images of transversal section at higher magnification). The scaffolds fabricated by freezing at -80 °C in the freezer and -40 °C in the shelf of the freeze-drier showed aligned porous structure. On the other hand, scaffolds obtained by freezing at -20 °C showed heterogeneous porous structure composed of areas where ice crystal grew preferentially along longitudinal direction triggering to aligned pores and others regions where ice crystals grew in all the directions prompting to random pore orientation. SEM images may indicate that freezing using Teflon mould preferably induced aligned porous structures. Unlike the teflon mould, scaffolds fabricated in well-plate did not show aligned porous structures as indicated SEM images of longitudinal section (Table 3). More homogeneous porous structures were obtained for scaffolds fabricated by freezing at -20 °C in the freezer compared to scaffolds frozen in well plate inside freeze-drier (-40 °C). Among the scaffolds fabricated at -20 °C, homogeneous isotropic porous structure were obtained for solid content of 10 wt.% and 7 wt.%. The lowest solid content prompted to larger pores. Considering the isotropic porous structure and the suitable pore size, this condition was selected to prepared 3D scaffolds.

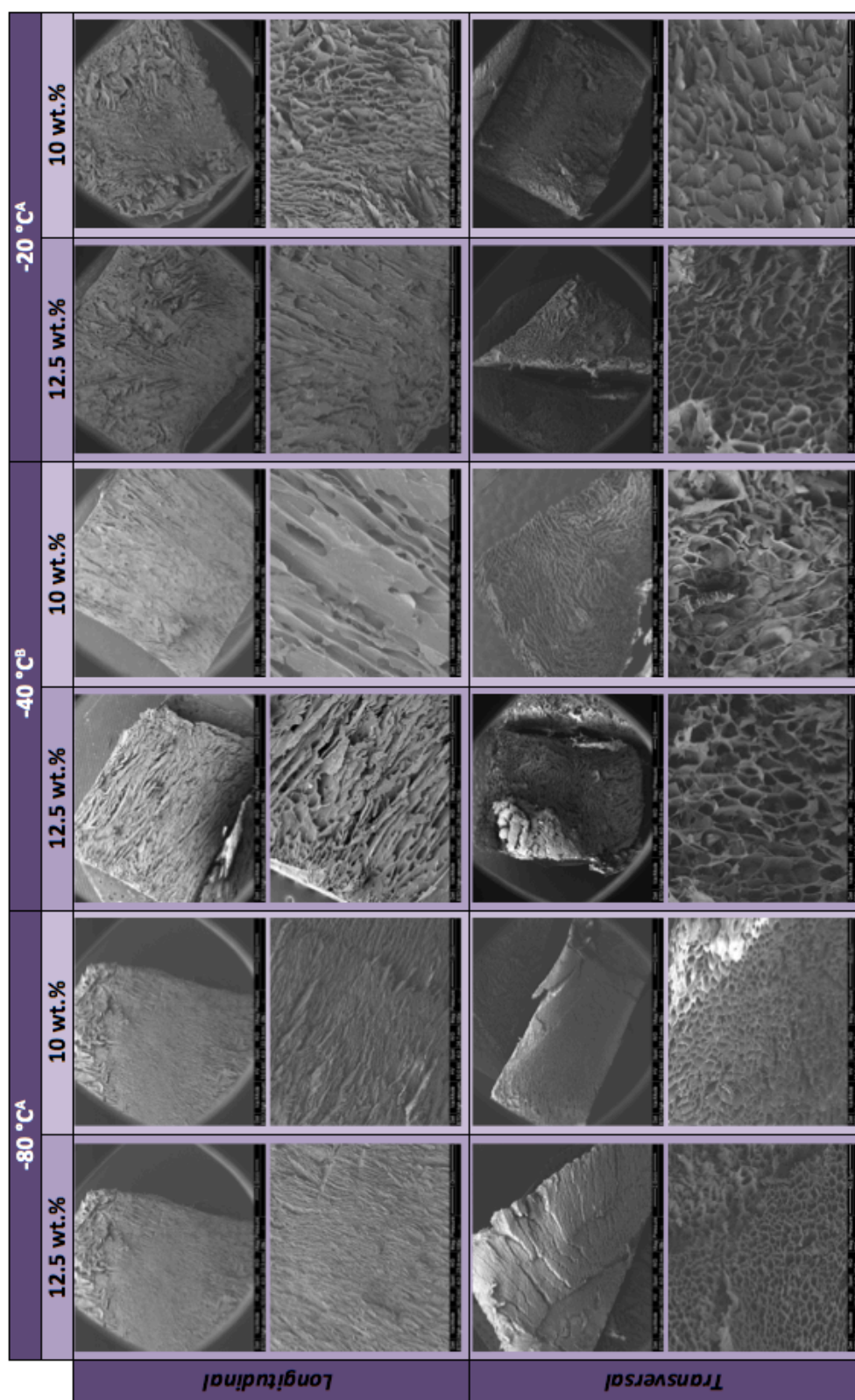
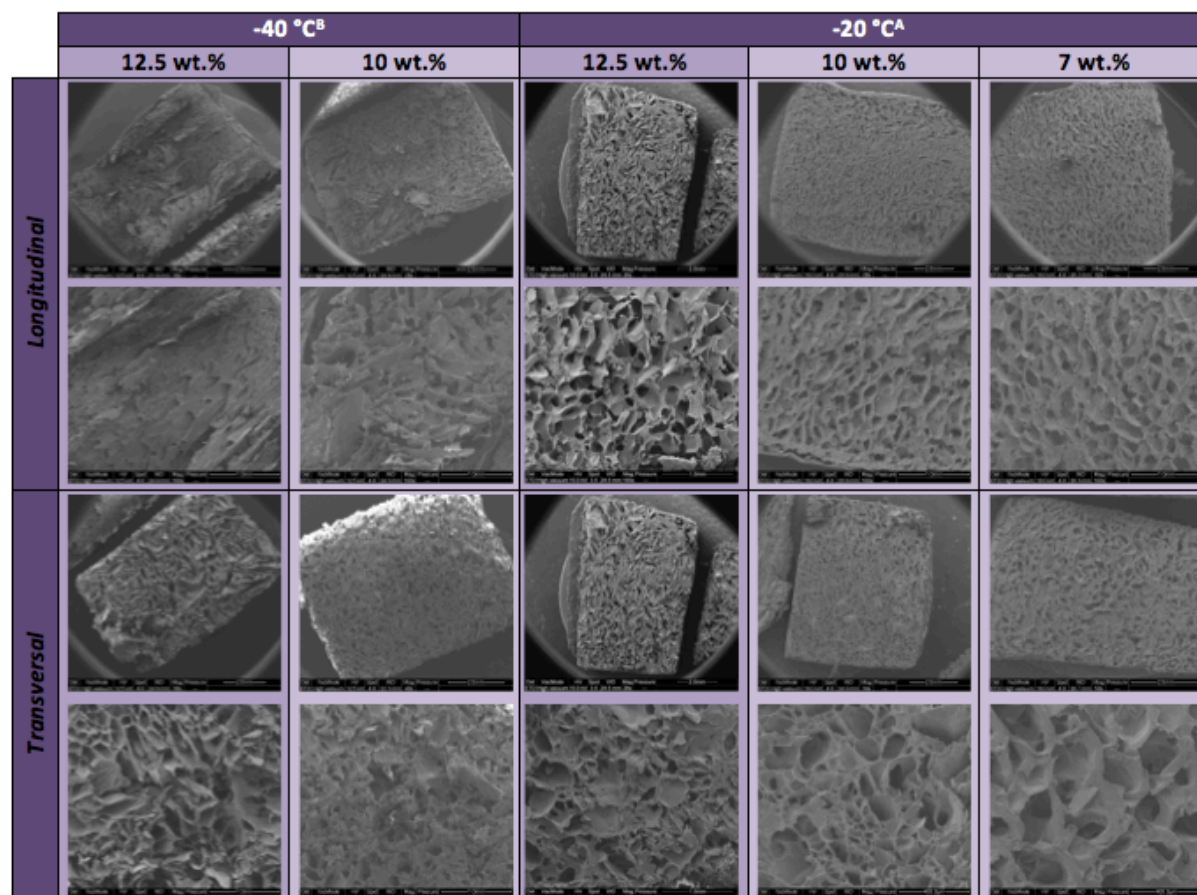


Table 2. SEM images of longitudinal and transversal section of 3D scaffolds designed by freeze-drying mineralized slurry in Teflon mold at -80 °C and -20 °C in freezer (A) and -40 °C inside freeze-dryer (B).

Table 3. SEM images of longitudinal and transversal section of 3D scaffolds designed by freeze-drying mineralized slurry in well plate at -40 °C in freeze-drier (B) and -20 °C in freezer (A).



6.3.2. Characterization of physic-chemical properties of designed 3D scaffold

The XRD pattern of non-mineralized scaffolds (RCP) exhibited a broad band belonging to organic phase whereas XRD pattern of mineralized scaffolds (Ap/RCP and MgAp/RCP) showed reflections ascribed to HA (ASTM card file No 9-432) (Figure 2a). The peaks were rather broad in both patterns indicating low crystallinity and nano-sized dimensions of the diffracting crystal domains obtained through the RCP biomimetic mineralization. In fact, FTIR spectrum of MgAp/RCP scaffolds (Figure 2b) also exhibited broad and relatively featureless phosphate bands indicating lower crystallinity of the mineral phase compared to Ap/RCP scaffold, as it is reported by the index for crystallinity degree calculated from FTIR spectra (splitting factor, Table 4).^{12,13} All FTIR spectra showed the presence of amide bands belongs to RCP: amide I (1637 cm^{-1}), amide II (1542 cm^{-1}) and amide III (1242 cm^{-1}).¹⁴ FTIR spectra of mineralized scaffolds also showed the ν_2 vibration mode of CO_3^{2-} group at 873 cm^{-1} that

corresponds with B-type carbonation (substitution of PO_4 by CO_3).¹⁵ The absence of the peak at 880 cm^{-1} (associated to A-type carbonation) could indicate that the carbonation can be assigned only to the B position. In fact, previous studies of the mineral phase along the chapter 3 revealed the B-type carbonation for synthesized apatites that was associated to the carbon dioxide surrounding the reaction vessel or to the presence of CaCO_3 impurities in the reactants.

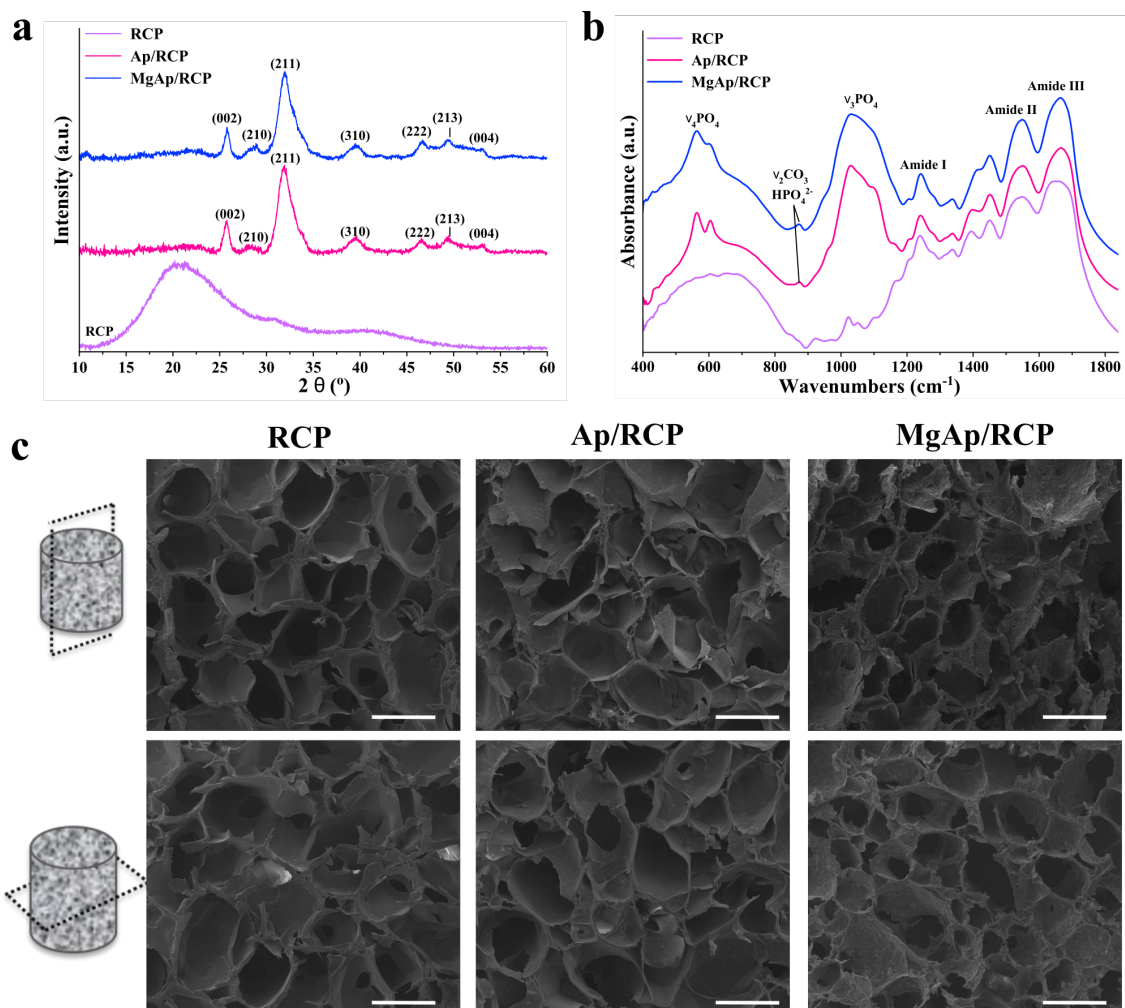


Figure 2. XRD (a), FTIR spectra (b) and SEM micrographs (c) of longitudinal and transversal section of RCP, Ap/RCP and MgAp/RCP scaffolds. Scale bar = 250 μm .

The carbonation of the as-synthesized apatite may explain the fact the Ca/P ratio of mineral phase was higher than stoichiometric hydroxyapatite ($\text{Ca/P} > 1.67$) (Table 4). The Mg/Ca molar ratio of MgAp/RCP scaffolds reached 1.29 wt.% in respect to the total scaffold weight (Table 4), which was slightly higher than the magnesium content reported for biological bone apatite.¹⁶

Table 4. Chemical composition of mineralized scaffolds analysed by ICP-OES (a). Splitting factor calculated from FTIR spectra of mineralized scaffolds (b).¹³ Data are expressed as mean ± SD of three samples (n=3).

Sample	Ca (mol) ^a	P (mol) ^a	Ca/P (mol) ^a	Mg (wt.%) ^a	Mg/Ca (% mol) ^a	SF ^b
RCP	0.01±0.01	0.00±0.00	-----	-----	-----	-----
Ap/RCP	0.39±0.01	0.21±0.00	1.83±0.04	0.10±0.02	-----	2.37±0.04
MgAp/RCP	0.37±0.00	0.20±0.00	1.87±0.01	1.29±0.00	14.4±0.06	2.09±0.03

Respect to scaffold microstructure, SEM observations clearly showed homogeneous pore structures in all the 3 scaffold compositions (Figure 2c). Large spherical pores were evenly distributed and well stacked along longitudinal and transversal section. Moreover, small pores could be seen on the walls of the large ones indicating good interconnectivity. The scaffolds exhibited a mean pore size close to 250 µm in all the cases (Table 5). On the other hand, mineralized scaffolds (Ap/RCP and MgAp/RCP) exhibited lower porosity (≈86% and 83%, respectively) when compared to non-mineralized one (≈92%) (Table 5). This effect is associated with an increase of the solid loading (e.g., concentration of the nanoparticles) that promotes a decrease of the resulting scaffold porosity.^{17,18} Scaffold permeability was evaluated by falling head method (described in Chapter 2). RCP and MgAp/RCP scaffolds showed similar permeability ($7 \cdot 10^{-6} \text{ m}^2$) whereas it decreased up to $4 \cdot 10^{-6} \text{ m}^2$ for Ap/RCP scaffolds (Table 5). Moreover, scaffold mechanical properties were measured by dynamic mechanical analysis (DMA, Chapter 2). Contrary to what might be expected, RCP scaffolds showed the highest young modulus whereas mineralized scaffolds showed lower values (Table 5). In fact, young modulus decreased approximately a threefold and seven fold for Ap/RCP and MgAp/RCP scaffolds, respectively.

Table 5. Macroscopic scaffolds properties: mean pore size of dried scaffolds calculated from SEM images (n=60), porosity calculated by gravimetry method (n=5), permeability determined by head falling method (n=5) and young modulus analysed by DMA (n=5). Data are expressed as mean ± SD.

Sample	Mean Pore Size (µm)	Porosity (%)	Permeability $10^{-6} \text{ (m}^2\text{)}$	Young Modulus (KPa)
RCP	260±65	92.2±0.4	7.25±1.15	174±40
Ap/RCP	226±51	86.5±0.6	4.01±0.29	68±15
MgAp/RCP	242±54	83.3±0.5	7.91±1.21	23±2

6.3.3. Evaluation of *in vitro* degradation of the scaffolds

The *in vitro* degradation of the scaffold was evaluated by quantification of the mass loss as well as the ion release from the scaffold under physiological condition (Figure 3). The weight of RCP and Ap/RCP scaffolds remained nearly constant along 28 days whereas the weight of MgAp/RCP scaffolds slightly decreased after 28 days in PBS (Figure 3a). The overall mass loss for the three scaffold compositions was very low thus indicating good scaffold stability under physiological conditions. Moreover, ion release quantified by ICP-OES analysis indicated that MgAp/RCP scaffolds showed a faster ion release than Ap/RCP scaffolds (Figure 3b). In fact, Ca ion released from MgAp/RCP scaffolds was 3 times higher than Ca ion released from Ap/RCP scaffolds. Moreover, Ca ion release from Ap/RCP scaffolds seemed to reach a plateau after 28 days of soaking while Ca and Mg ion release from MgAp/RCP was still rising at this time point. Surprisingly, MgAp/RCP scaffolds showed a higher cumulative Mg ion release (7.06 ± 0.07 wt.%) compared to Ca ion (0.16 ± 0.01 wt.%) after 28 days (Figure 3b), indicating a faster release of Mg ions compared to Ca ions.

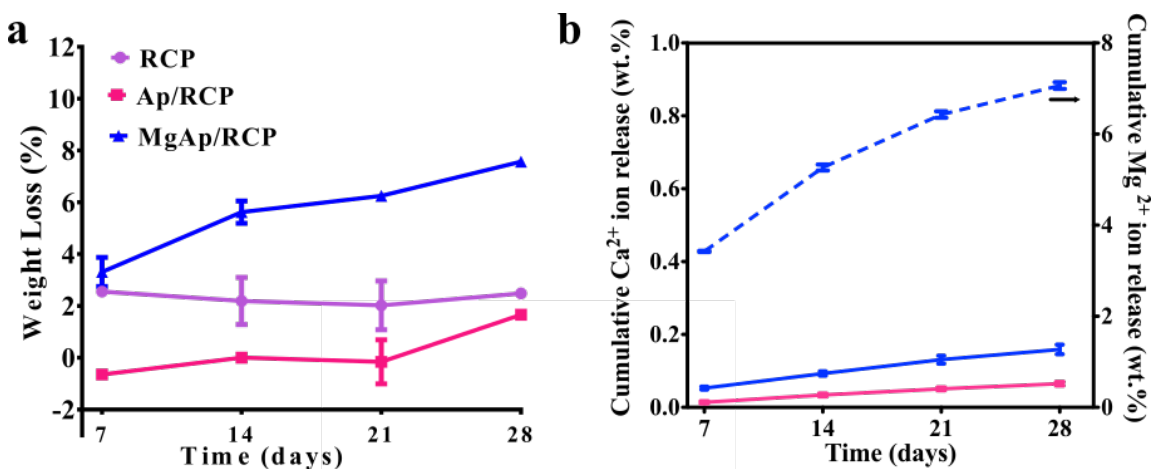


Figure 3. (a) Degradation profile of scaffolds after soaking in PBS displayed as weight loss respect to immersion time and (b) cumulative ion released from Ap/RCP (pink line) and MgAp/RCP (blue line) scaffolds in PBS medium determined by ICP-OES as a function of time. Ca²⁺ ion concentration (wt.% respect to the total Ca content in Ap/RCP and MgAp/RCP scaffold) is represented in continuous line (y left axis) whereas Mg²⁺ concentration (wt.% respect to total Mg content in MgAp/RCP scaffold) is displayed in dashed line (y right axis). Data are expressed as mean \pm SD (n=3).

6.3.4. Cell viability and proliferation

Cell viability was qualitatively assessed after 1 day of cell culture with live/dead assay. Figure 4a shows just few dead cells and homogeneous distribution of live cell on the top of RCP, Ap/RCP and MgAp/RCP scaffolds indicating good cell seeding and high cell viability after 1 day of cell culture. Moreover, cell viability on the three different scaffold compositions was quantitatively assessed by MTT assay (Figure 4b). The results indicated a significant increase of MSC proliferation over the time for all the scaffolds ($p < 0.001$). The rate of MSC proliferation on RCP and MgAp/RCP scaffolds was significantly higher than Ap/RCP scaffolds on day 3, 7 and 21 ($p < 0.01$). In detail, MgAp/RCP scaffolds showed the highest MSC proliferation at day 7, 14 and 21 of cell culture ($p < 0.01$). After 28 days of culture, these differences on MSC proliferation disappeared (Figure 4b).

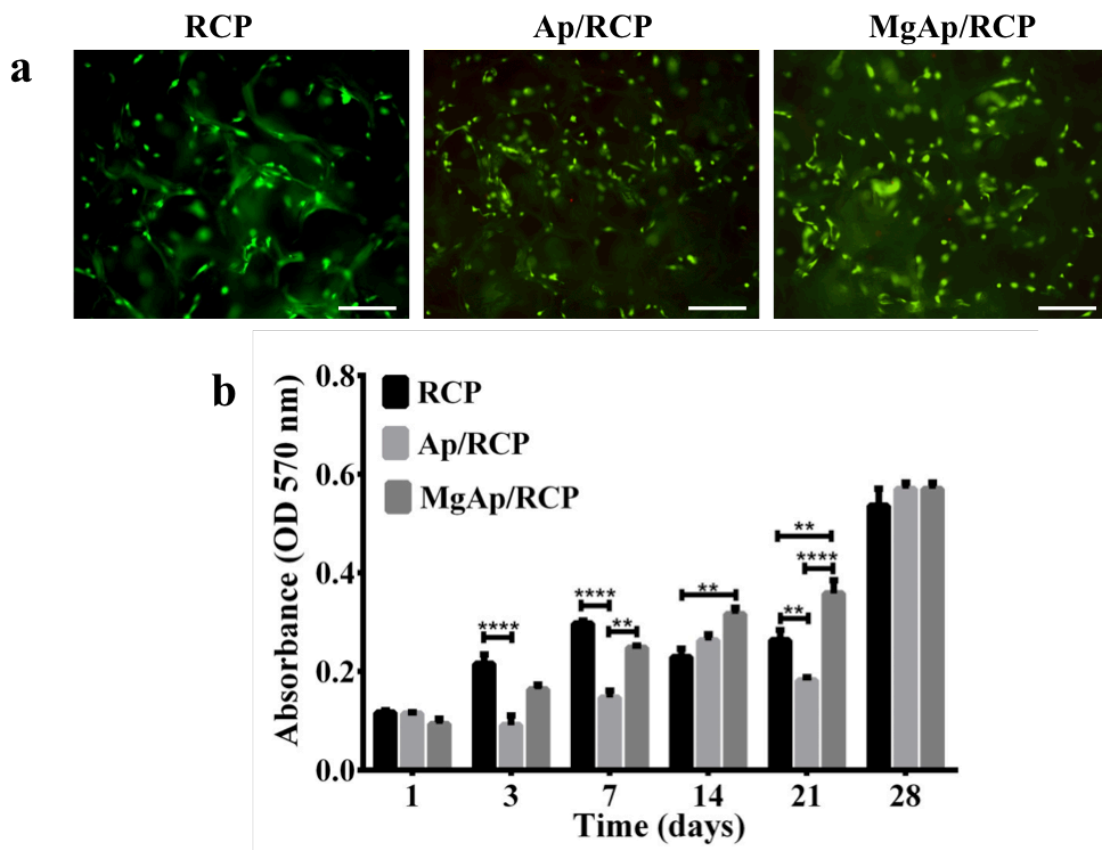


Figure 4. Cytocompatibility. (a) Live/dead assay to evaluate cell viability after 1 day of cell culture. Live cells in green, dead cells in red on RCP, Ap/RCP and MgAp/RCP scaffolds, respectively (Scale bar: 100 μ m). (b) Cell viability evaluated by MTT assay after 1, 3, 7, 14, 21 and 28 days. Data are expressed as mean \pm SEM (n=3). ** $p < 0.01$ and **** $p < 0.0001$.

6.3.5. Cell-material interaction

MSC adhesion and spreading on the different scaffold compositions after 1 and 7 days of culture were analyzed by SEM (Figure 5). After 1 day of cell culture, cells were well spread in the top scaffold surface with tight interactions, without significant differences among the three groups. However, obvious differences could be observed in terms of adhered cell amount and morphology between RCP, Ap/RCP and MgAp/RCP scaffolds after 7 days of cell culture. Whereas the number of cells was remarkably larger and the cells spread better in RCP and MgAp/RCP scaffolds at the same time point of culture (7 days), the Ap/RCP scaffolds seemed to promote a detrimental effect on the cell adhesion and spreading, as previously observed in MTT analysis (Figure 4b).

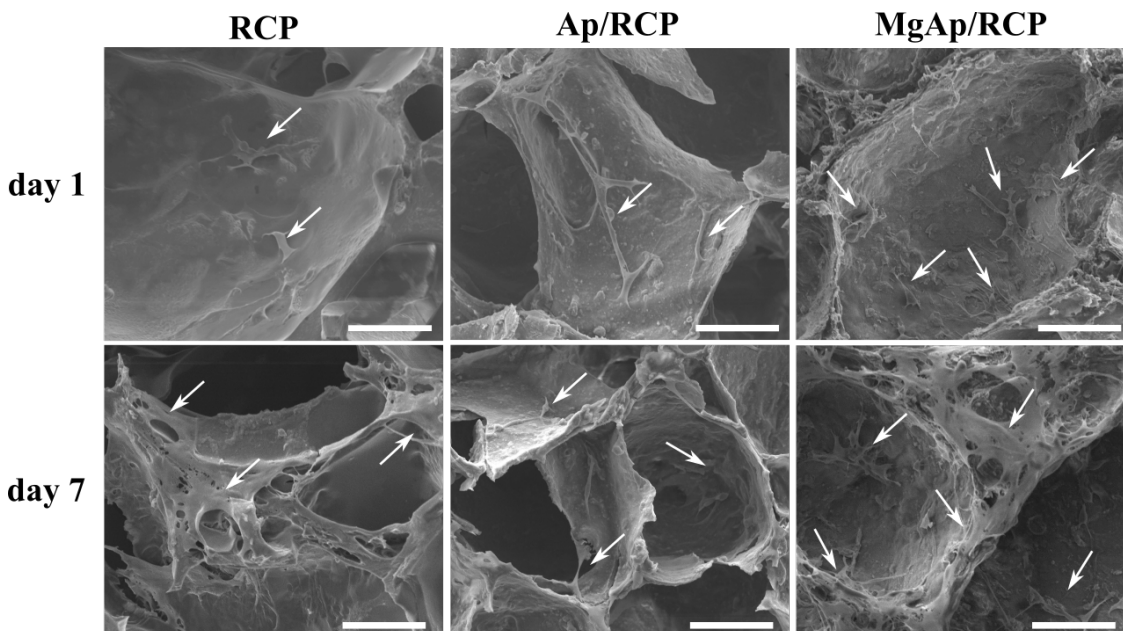


Figure 5. SEM images of MSC cells (white arrows) adhered on the top of the scaffold surfaces after 1 and 7 days of cell culture. Scale bar: 150 μ m.

While previous analysis gave an estimation of the cell proliferation over the time (MTT assay) and cell distribution at the top surface of the scaffolds (SEM analysis), they did not provide information related to the spatial distribution of the cells inside the scaffolds. For that purpose, each sample was longitudinally sectioned, cell nuclei were stained with DAPI and the inner scaffold surface was scanned in three different areas (top, middle and bottom) (Figure 6b). Images of the upper scaffold surface (Figure 6a) clearly revealed a larger number of cells in the external part compare to the three different inner areas (Figure 6b). Furthermore, MgAp/RCP scaffolds showed a larger

number of cells in the inner part of the scaffold (top, middle and bottom) compared to Ap/RCP ($p < 0.001$) and RCP scaffolds ($p < 0.0001$), as indicated in figure 6d.

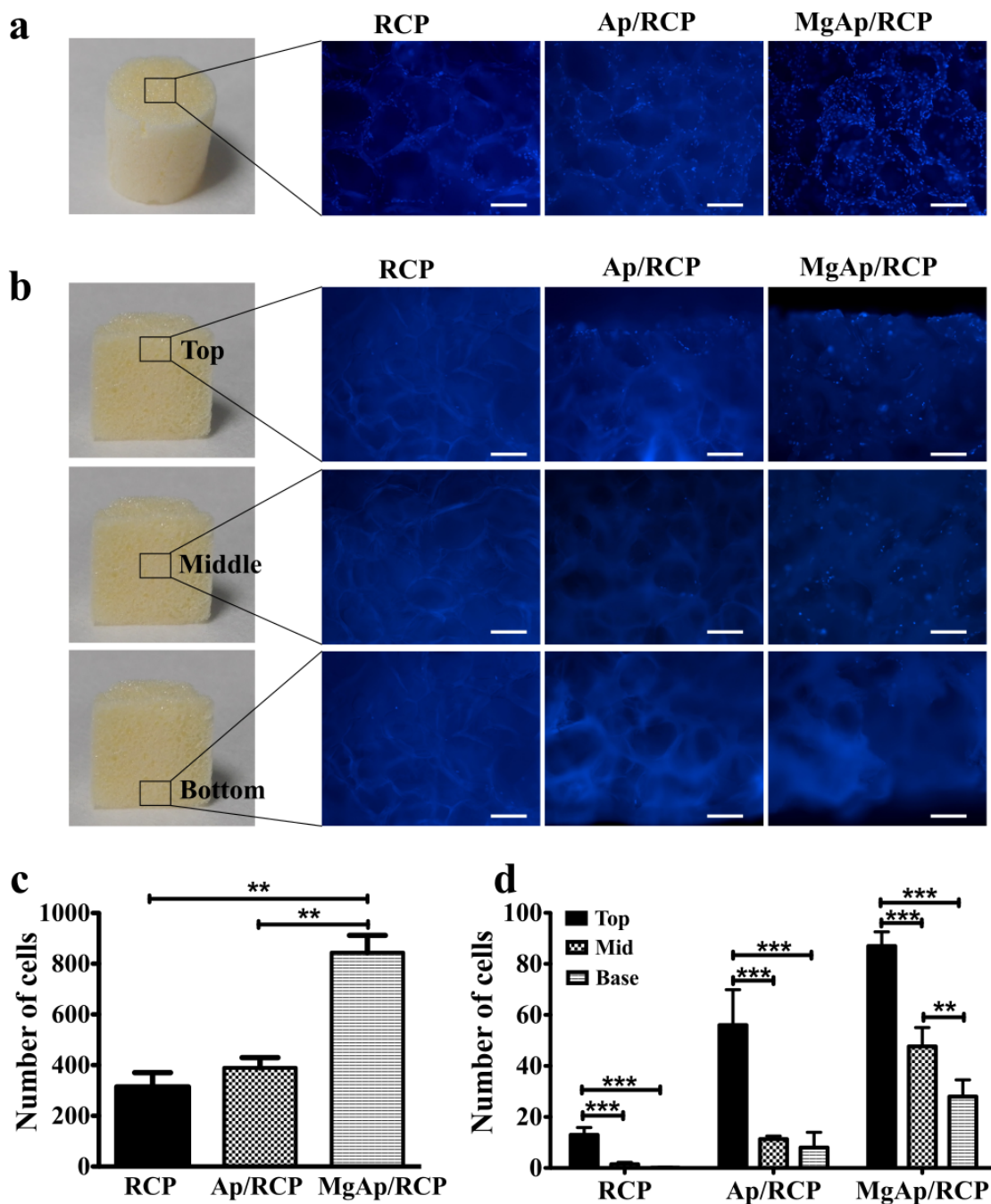


Figure 6. Cell distribution in the scaffolds after 14 days of cell culture. (a) Microscopic images of the upper surface of scaffolds. (b) Microscopic images of three areas from inner part of scaffolds (top, middle and bottom). Blue: cell nuclei. Scale bar: 200 μ m. Graphs display the quantification of the number of cells at the upper surface of the scaffolds (c) and in 3 different inner areas of each scaffold. Data are expressed as mean \pm SEM obtained from three different images ($n=3$). ** $p < 0.01$ and **** $p < 0.0001$.

6.3.6. Effect of the scaffold on the osteogenic marker expression

To examine any effect on the expression of the osteogenic markers, induced by the three different scaffolds, ascribable to the three types of scaffolds, mRNA level of alkaline phosphatase (ALP), osteopontin (OPN) and collagen (Col1) was analyzed by qPCR (Figure 7a, b and c, respectively), β -catenin protein expression by western blotting (Figure 7d) and the expression of runt-related transcription factor 2 (RUNX-2) by immunofluorescence (Figure 8). The results indicated that the ALP expression was up-regulated in MSCs grown in Ap/RCP and MgAp/RCP and these differences were statistically significant compare to RCP ($p < 0.001$) after 14 days of culture (Figure 7a). ALP mRNA level decreased after 28 days of cell culture compared to 14 days. However, the significant up-regulation of this gene compared to the RCP was maintained ($p < 0.05$).

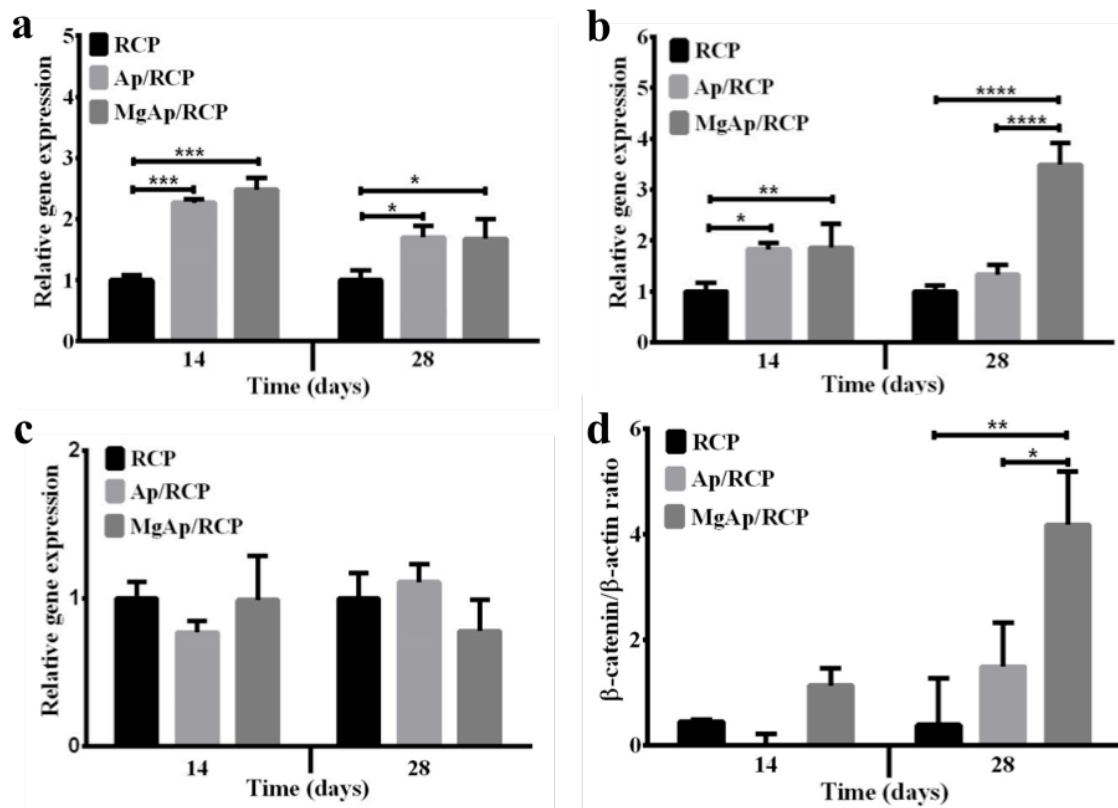


Figure 7. Relative quantification ($2^{-\Delta\Delta C_t}$) of gene expression profiling of ALP (a), OPN (b) and COL 1 (c) with respect to the expression of the cells grown on RCP (control), using as housekeeping gene GAPDH, after 14 and 28 days. (d) Western blot analysis of β -catenin expression in comparison with β -actin (loaded as a control) after 14 and 28 days of cell culture. Data are expressed as mean \pm SEM (n=3). * $p < 0.05$; ** $p < 0.01$, *** $p < 0.001$ and **** $p < 0.0001$.

The same trend was observed in OPN expression; in fact, MSCs cultured for 14 days on Ap/RCP and MgAp/RCP scaffolds displayed a significant increase of OPN mRNA level compared to RCP scaffolds ($p < 0.05$ and $p < 0.01$, respectively) (Figure 7b). The level of this gene remained unvaried after 28 days in the cells growing on Ap/RCP scaffolds while showed a significant up-regulation in cells cultured in MgAp/RCP scaffolds compared to RCP and Ap/RCP ones ($p < 0.0001$). No differences were found in the Col1 expression of MSCs cultured in RCP, Ap/RCP and MgAp/RCP scaffolds at both time points (Figure 7c). Western blot analysis (Figure 7d) demonstrated that MSCs cultured for 28 days onto MgAp/RCP scaffolds induced significantly higher expression of β -catenin levels compare to MSCs cultured onto RCP and Ap/RCP scaffolds ($p < 0.01$ and $p < 0.05$, respectively).

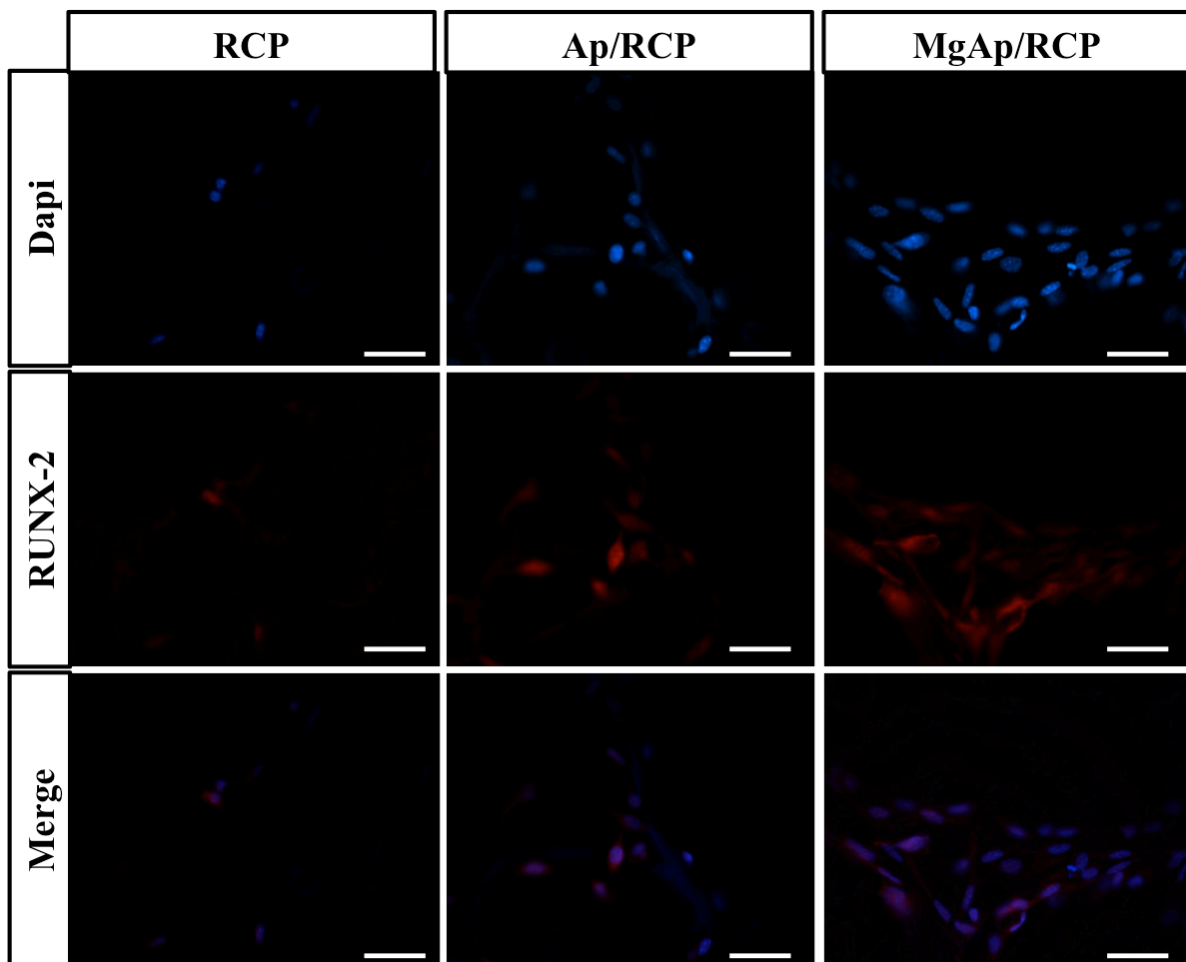


Figure 8. Representative immunofluorescence images of MSCs cells after 14 days on the three different scaffold composition. RUNX-2 in red and cell nuclei in blue. Scale bar: 50 μm .

In addition, the immunofluorescent evaluation of RUNX-2 after 14 days of cell culture might indicate a higher amount of this osteogenic marker in MSCs cultured on MgAp/RCP than Ap/RCP and RCP scaffolds (Figure 8).

6.4. Discussion

In bone tissue regeneration, the interactions of bone substitutes with the host tissue play a key role in the regeneration process. In detail, its surface could enhance cell adhesion and/or osteogenic differentiation and often lead to an improvement of transplantation efficiency.¹⁹ Current challenges in bone tissue regeneration include the engineering of scaffolds with new levels of biofunctionality that attempt to recreate nanoscale topographical and biofactor cues from bone extra cellular matrix (ECM). In this work, 3D isotropic hybrid scaffolds for bone regeneration were produced by bioinspired mineralization of recombinant collagen type I derived peptide (RCP) and further freeze-drying. By controlling several parameters during freezing, scaffolds with desired porous structure were fabricated. The last goal was to demonstrate that biom mineralized samples enhance cell migration throughout the whole scaffold as well as potentially induce the expression of MSC osteogenic markers *in vitro*.

By modifying different parameters of freezing protocol, porous structure was optimized. For both moulds, teflon and well plate, higher freezing temperature as well as lower solid content led to larger pores, as it has been pointed out previously by several authors.^{9,20} Nevertheless, isotropic porous scaffolds with homogeneous structure were obtained for scaffolds fabricated by freezing mineralized slurry at -20°C in well plate. With these parameters, scaffolds of three different compositions were developed: non-mineralized (RCP), mineralized (Ap/RCP) and mineralized in the presence of magnesium (MgAp/RCP). The three scaffold compositions (RCP, Ap/RCP and MgAp/RCP) showed mean pore diameter close to 250 µm that is on the range of pore sizes (between 200-350 µm) claimed as the optimum for osteoconduction.²¹⁻²³ Moreover, the porosity of designed scaffolds showed similar values to that found in cancellous bone (around 75-95%) providing the required space for marrow and blood vessels development necessary for bone regeneration.²⁴ Another key factor, correlated to the porosity, to consider in the design of tissue-engineered scaffolds is the permeability that dictates diffusive transport of cytokines, nutrients, and waste throughout the scaffold.^{25,26} The permeability of bone-like scaffolds designed in this

work was higher than the permeability values reported for cancellous bone based upon Darcy's Law,²⁷ indicating a promising *in vivo* performance of the herein designed scaffolds.

Bioinspired mineralization of natural collagen has been proved to enhance scaffold mechanical properties.²⁸ Conversely, in this work, non-mineralized scaffolds showed higher young modulus than mineralized ones (Ap/RCP and MgAp/RCP). This effect may indicate that the mechanical properties of designed scaffolds do not rely on scaffold composition (mineral content), but may rely on other parameters such as structure²⁹ or crosslinking extent^{30,31} of the organic matrix. Considering that the three scaffold compositions have similar porosity and pore size, a higher stiffness of RCP scaffolds respect to Ap/RCP and MgAp/RCP may be associated to the crosslinking extent since RCP scaffolds were endowed with the highest extent of crosslinking (Chapter 5).

As we mentioned above, the main benefit of biomimetic mineralization protocol consists in controlling both biophysical and biochemical cues at scaffold interface that synergistically regulate the fate of MSCs *in vitro* or *in vivo* environment.^{10,32} Poor crystalline apatite was obtained *via* biomimetic mineralization of RCP due to the individual and synergistic effect of the organic matrix (Ap/RCP) and Mg ions (MgAp/RCP) on stabilizing the amorphous precursor phase.³³ FTIR spectra indicated the lower crystallinity of the mineral phase containing in MgAp/RCP scaffolds that can promote a higher reactivity under physiological conditions. Previous works that evaluated solubility of the mineral phase by electrokinetic studies indicated that both the Mg substitution and the B-type carbonation improved the solubility of the apatite powder at the physiological pH value (≈ 7.4).³⁴ Actually, MgAp/RCP scaffolds exhibited a faster Ca ion release kinetic when compared to Ap/RCP scaffolds. It has been reported that the Ca and Mg ions in culture medium enhance the adhesion and stimulate the osteogenic differentiation of cells.^{10,35-38} Yoshizawa *et al.*³⁹ demonstrated that hBMSCs proliferated faster and they produced more mineralized matrix *in vitro* due the presence of 10 mM MgSO₄ in cell culture medium. Concerning Ca, it has been found that Ca concentration of 7.8 mM in cell culture medium could enhance the proliferation and the up-regulation of osteogenic genes in hMSCs.³⁸ In our studies, enhanced cell growth and proliferation was found on MgAp/RCP scaffolds when compared to Ap/RCP and RCP scaffolds at day 7, 14 and 21. This effect could be attributed to the Mg ions release from the scaffolds that was more than six times higher than the release of Ca ions.

Nevertheless, the cell proliferation reached the plateau for all the groups after 28 days and did not show statistical differences among them at the end of the experiment.

In our study, it was also important to identify those scaffolds that best supported cell colonization and proliferation within the inner part of the scaffolds since it would be a requirement for successful integration *in vivo*. The *in vitro* cell culture studies revealed that biomimetic mineralization of RCP enhanced the cell-material interaction. In fact, MgAp/RCP scaffolds potentially induced cell migration throughout the whole 3D scaffold when compared to Ap/RCP and RCP scaffolds. Most of previous works have been focused on determining the effect of pore size on cell attachment,^{20,30} but only small number of works have analysed the cell migration throughout the whole 3D scaffold.^{40,41} Since scaffolds exhibited similar pore size and porosity, a greater cell migration on MgAp/RCP scaffolds could be related with its physic-chemical surface properties. On one hand, the presence of Mg could improve the cell-material interaction since it has been previously reported that Mg interacts with osteoblast integrins, which are responsible for cell adhesion and stability.^{35,36} On the other hand, cell-material interaction could be enhanced by surface roughness of MgAp/RCP scaffolds which was similar to that found in bone (Chapter 4). The main concern of cell migration inside the scaffolds is related to the *in vivo* performance of the scaffolds since the cell distribution within the scaffolds has been related to the distribution of tissue subsequently formed within engineered constructs,⁴² suggesting that uniform cell seeding could establish the basis for uniform tissue generation.

Another important indicator of bioactivity is the induction of the expression of genes and protein related to the MSC osteogenic commitment, that is on the basis of the bone regenerative process.⁴³ The differentiation process towards osteoblasts is regulated by a number of key factors and signalling pathways. ALP, which is responsible for the mineralization of the ECM,⁴³ OPN, that is the mainly non-collagenous protein of the mineralized matrix,⁴⁴ and RUNX2 which is often referred to as the master switch of osteogenic differentiation,^{45,46} are commonly used as early markers of osteogenic differentiation *in vitro*. In this work a protein and gene expression profile of the cells grown in the three different scaffolds were analysed. Our results showed that ALP and OPN genes were up-regulated in both Ap/RCP and MgAp/RCP scaffolds compared to RCP after 14 days of culture, indicating that the physic-chemical features of the scaffold provided by the presence of biomimetic apatite play an important role in the regulation of MSC fate, as previously demonstrated on *in vitro* studies of hydroxyapatite

nanocrystals.⁴⁷ Moreover, MSCs cultured for 28 days in MgAp/RCP scaffolds lead to an increase of OPN mRNA and β -catenin protein expression, considered an important factor involved in the signalling pathways that promotes MSC differentiation and osteoblast activity.⁴⁸ These results highlighted the key role of interfacial properties (chemical and physical cues) of scaffolds on cell migration and the greatest potential of MgAp/RCP scaffolds inducing MSC osteogenic differentiation *in vitro*.

6.5. Conclusions

In this work, 3D scaffolds for bone regeneration were synthesized by bioinspired mineralization of recombinant collagen type I derived peptide (RCP) and further freeze-drying. By controlling several freezing parameters such as freezing temperature and solid content and also by using different moulds, we can obtain anisotropic or isotropic structures with different pore sizes. 3D isotropic porous scaffolds differing on chemical composition (RCP, Ap/RCP and MgAp/RCP) but with similar mean pore size (250 μm), porosity (close to 90%) and great permeability were designed through optimized freeze-drying protocol. Mineralized scaffolds showed a better cell migration in the inner areas of scaffold compared to non-mineralized scaffolds as well as displayed excellent potential for improving the expression of osteogenic markers of MSCs, which was reflected by a series of *in vitro* assays both on the cellular and molecular levels. Magnesium incorporation during mineralization protocol (MgAp/RCP) actually heightens the cell migration and osteogenic potential of designed scaffolds. Thus, this work indicates a promising approach for the development of high quality bone grafts with smart interfaces through biomimetic mineralization of synthetic engineering peptides and the optimized freeze-drying protocol.

References

1. Tsuruga, E., Takita, H., Itoh, H., Wakisaka, Y. and Kuboki, Y. Pore size of porous hydroxyapatite as the cell-substratum controls BMP-induced osteogenesis. *The journal of biochemistry* **121**, 317, 1997.
2. y Leon, C.A.L. New perspectives in mercury porosimetry. *Adv Colloid Interface Sci* **76**, 341, 1998.
3. Roy, T.D., Simon, J.L., Ricci, J.L., Rekow, E.D., Thompson, V.P. and Parsons, J.R. Performance of degradable composite bone repair products made via three-dimensional fabrication techniques. *J Biomed Mater Res A* **66**, 283, 2003.
4. Kuboki, Y., Takita, H., Kobayashi, D., Tsuruga, E., Inoue, M., Murata, M., Nagai, N., Dohi, Y. and Ohgushi, H. BMP-induced osteogenesis on the surface

- of hydroxyapatite with geometrically feasible and nonfeasible structures: topology of osteogenesis. *J Biomed Mater Res* **39**, 190, 1998.
5. Correia, C., Bhumiratana, S., Yan, L.-P., Oliveira, A.L., Gimble, J.M., Rockwood, D., Kaplan, D.L., Sousa, R.A., Reis, R.L. and Vunjak-Novakovic, G. Development of silk-based scaffolds for tissue engineering of bone from human adipose-derived stem cells. *Acta Biomater* **8**, 2483, 2012.
 6. Murphy, C.M., Haugh, M.G. and O'Brien, F.J. The effect of mean pore size on cell attachment, proliferation and migration in collagen–glycosaminoglycan scaffolds for bone tissue engineering. *Biomaterials* **31**, 461, 2010.
 7. Jones, A.C., Arns, C.H., Huttmacher, D.W., Milthorpe, B.K., Sheppard, A.P. and Knackstedt, M.A. The correlation of pore morphology, interconnectivity and physical properties of 3D ceramic scaffolds with bone ingrowth. *Biomaterials* **30**, 1440, 2009.
 8. Karageorgiou, V. and Kaplan, D. Porosity of 3D biomaterial scaffolds and osteogenesis. *Biomaterials* **26**, 5474, 2005.
 9. Pawelec, K., Husmann, A., Best, S.M. and Cameron, R.E. Ice-templated structures for biomedical tissue repair: From physics to final scaffolds. *Applied Physics Reviews* **1**, 021301, 2014.
 10. Samavedi, S., Whittington, A.R. and Goldstein, A.S. Calcium phosphate ceramics in bone tissue engineering: a review of properties and their influence on cell behavior. *Acta Biomater* **9**, 8037, 2013.
 11. Parvizi, M., Plantinga, J.A., van Speuwel-Goossens, C.A., van Dongen, E.M., Kluijtmans, S.G. and Harmsen, M.C. Development of recombinant collagen-peptide-based vehicles for delivery of adipose-derived stromal cells. *J Biomed Mater Res A* **104**, 503, 2016.
 12. Koutsopoulos, S. Synthesis and characterization of hydroxyapatite crystals: A review study on the analytical methods. *J Biomed Mater Res* **62**, 600, 2002.
 13. Termine, J.D. and Posner, A.S. Infra-red determination of the percentage of crystallinity in apatitic calcium phosphates. 1966.
 14. Morris, M.D. and Finney, W.F. Recent developments in Raman and infrared spectroscopy and imaging of bone tissue. *Spectroscopy* **18**, 155, 2004.
 15. Antonakos, A., Liarokapis, E. and Leventouri, T. Micro-Raman and FTIR studies of synthetic and natural apatites. *Biomaterials* **28**, 3043, 2007.
 16. Gómez-Morales, J., Iafisco, M., Delgado-López, J.M., Sarda, S. and Drouet, C. Progress on the preparation of nanocrystalline apatites and surface characterization: Overview of fundamental and applied aspects. *Prog Cryst Growth Ch* **59**, 1, 2013.
 17. Deville, S. and Bernard-Granger, G. Influence of surface tension, osmotic pressure and pores morphology on the densification of ice-templated ceramics. *J Eur Ceram Soc* **31**, 983, 2011.
 18. Jung, H.-D., Yook, S.-W., Kim, H.-E. and Koh, Y.-H. Fabrication of titanium scaffolds with porosity and pore size gradients by sequential freeze casting. *Mater Lett* **63**, 1545, 2009.
 19. Petrie, T.A., Raynor, J.E., Reyes, C.D., Burns, K.L., Collard, D.M. and García, A.J. The effect of integrin-specific bioactive coatings on tissue healing and implant osseointegration. *Biomaterials* **29**, 2849, 2008.
 20. O'Brien, F.J., Harley, B.A., Yannas, I.V. and Gibson, L.J. The effect of pore size on cell adhesion in collagen-GAG scaffolds. *Biomaterials* **26**, 433, 2005.

21. Whang, K., Healy, K., Elenz, D., Nam, E., Tsai, D., Thomas, C., Nuber, G., Glorieux, F., Travers, R. and Sprague, S. Engineering bone regeneration with bioabsorbable scaffolds with novel microarchitecture. *Tissue Eng* **5**, 35, 1999.
22. Klawitter, J. and Hulbert, S. Application of porous ceramics for the attachment of load bearing internal orthopedic applications. *J Biomed Mater Res* **5**, 161, 1971.
23. Schwartz, I., Robinson, B.P., Hollinger, J.O., Szachowicz, E.H. and Brekke, J. Calvarial bone repair with porous D, L-polylactide. *Otolaryngology--Head and Neck Surgery* **112**, 707, 1995.
24. Palmer, L.C., Newcomb, C.J., Kaltz, S.R., Spoerke, E.D. and Stupp, S.I. Biomimetic Systems for Hydroxyapatite Mineralization Inspired By Bone and Enamel. *Chem Rev* **108**, 4754, 2008.
25. Agrawal, C.M., McKinney, J.S., Lanctot, D. and Athanasiou, K.A. Effects of fluid flow on the *in vitro* degradation kinetics of biodegradable scaffolds for tissue engineering. *Biomaterials* **21**, 2443, 2000.
26. Caliarì, S.R. and Harley, B.A. The effect of anisotropic collagen-GAG scaffolds and growth factor supplementation on tendon cell recruitment, alignment, and metabolic activity. *Biomaterials* **32**, 5330, 2011.
27. Kohles, S.S., Roberts, J.B., Upton, M.L., Wilson, C.G., Bonassar, L.J. and Schlichting, A.L. Direct perfusion measurements of cancellous bone anisotropic permeability. *J Biomech* **34**, 1197, 2001.
28. Li, Y., Thula, T.T., Jee, S., Perkins, S.L., Aparicio, C., Douglas, E.P. and Gower, L.B. Biomimetic Mineralization of Woven Bone-Like Nanocomposites: Role of Collagen Cross-Links. *Biomacromolecules* **13**, 49, 2011.
29. Henkel, J., Woodruff, M.A., Epari, D.R., Steck, R., Glatt, V., Dickinson, I.C., Choong, P.F., Schuetz, M.A. and Hutmacher, D.W. Bone regeneration based on tissue engineering conceptions—a 21st century perspective. *Bone research* **1**, 216, 2013.
30. Tierney, C.M., Haugh, M.G., Liedl, J., Mulcahy, F., Hayes, B. and O'Brien, F.J. The effects of collagen concentration and crosslink density on the biological, structural and mechanical properties of collagen-GAG scaffolds for bone tissue engineering. *J Mech Behav Biomed Mater* **2**, 202, 2009.
31. Haugh, M.G., Murphy, C.M., McKiernan, R.C., Altenbuchner, C. and O'Brien, F.J. Crosslinking and mechanical properties significantly influence cell attachment, proliferation, and migration within collagen glycosaminoglycan scaffolds. *Tissue Engineering Part A* **17**, 1201, 2011.
32. Xu, K., Chen, W., Hu, Y., Shen, X., Xu, G., Ran, Q., Mu, C., Yu, Y. and Cai, K. Influence of strontium ions incorporated nanosheet-pore topographical titanium substrates on osteogenic differentiation of mesenchymal stem cells *in vitro* and osseointegration *in vivo*. *Journal of Materials Chemistry B* 2016.
33. Ramírez-Rodríguez, G.B., Delgado-López, J.M., Iafisco, M., Montesi, M., Sandri, M., Sprio, S. and Tampieri, A. Biomimetic mineralization of recombinant collagen type I derived protein to obtain hybrid matrices for bone regeneration. *J Struct Biol* 2016.
34. Landi, E., Logroscino, G., Proietti, L., Tampieri, A., Sandri, M. and Sprio, S. Biomimetic Mg-substituted hydroxyapatite: From synthesis to *in vivo* behaviour. *J Mater Sci Mater Med* **19**, 239, 2008.
35. Zreiqat, H., Howlett, C., Zannettino, A., Evans, P., Schulze-Tanzil, G., Knabe, C. and Shakibaei, M. Mechanisms of magnesium-stimulated adhesion of

- osteoblastic cells to commonly used orthopaedic implants. *J Biomed Mater Res* **62**, 175, 2002.
36. Yamasaki, Y., Yoshida, Y., Okazaki, M., Shimazu, A., Uchida, T., Kubo, T., Akagawa, Y., Hamada, Y., Takahashi, J. and Matsuura, N. Synthesis of functionally graded MgCO₃ apatite accelerating osteoblast adhesion. *J Biomed Mater Res* **62**, 99, 2002.
 37. Yoshizawa, S., Brown, A., Barchowsky, A. and Sfeir, C. Role of magnesium ions on osteogenic response in bone marrow stromal cells. *Connect Tissue Res* **55**, 155, 2014.
 38. Barradas, A.M., Fernandes, H.A., Groen, N., Chai, Y.C., Schrooten, J., van de Peppel, J., van Leeuwen, J.P., van Blitterswijk, C.A. and de Boer, J. A calcium-induced signaling cascade leading to osteogenic differentiation of human bone marrow-derived mesenchymal stromal cells. *Biomaterials* **33**, 3205, 2012.
 39. Yoshizawa, S., Brown, A., Barchowsky, A. and Sfeir, C. Magnesium ion stimulation of bone marrow stromal cells enhances osteogenic activity, simulating the effect of magnesium alloy degradation. *Acta Biomater* **10**, 2834, 2014.
 40. Sobral, J.M., Caridade, S.G., Sousa, R.A., Mano, J.F. and Reis, R.L. Three-dimensional plotted scaffolds with controlled pore size gradients: Effect of scaffold geometry on mechanical performance and cell seeding efficiency. *Acta Biomater* **7**, 1009, 2011.
 41. Allan, I.U., Tolhurst, B.A., Shevchenko, R.V., Dainiak, M.B., Illsley, M., Ivanov, A., Jungvid, H., Galaev, I.Y., James, S.L., Mikhailovsky, S.V. and James, S.E. An *in vitro* evaluation of fibrinogen and gelatin containing cryogels as dermal regeneration scaffolds. *Biomaterials Science* **4**, 1007, 2016.
 42. Holy, C.E., Shoichet, M.S. and Davies, J.E. Engineering three-dimensional bone tissue *in vitro* using biodegradable scaffolds: investigating initial cell-seeding density and culture period. *J Biomed Mater Res* **51**, 376, 2000.
 43. Granéli, C., Thorfve, A., Ruetschi, U., Brisby, H., Thomsen, P., Lindahl, A. and Karlsson, C. Novel markers of osteogenic and adipogenic differentiation of human bone marrow stromal cells identified using a quantitative proteomics approach. *Stem Cell Res* **12**, 153, 2014.
 44. Aubin, J.E. Regulation of Osteoblast Formation and Function. *Rev Endocr Metab Disord* **2**, 81, 2001.
 45. Ducy, P., Schinke, T. and Karsenty, G. The osteoblast: a sophisticated fibroblast under central surveillance. *Science* **289**, 1501, 2000.
 46. Deng, Z.-L., Sharff, K.A., Tang, N., Song, W.-X., Luo, J., Luo, X., Chen, J., Bennett, E., Reid, R. and Manning, D. Regulation of osteogenic differentiation during skeletal development. *Front Biosci* **13**, 2001, 2008.
 47. Montesi, M., Panseri, S., Iafisco, M., Adamiano, A. and Tampieri, A. Effect of hydroxyapatite nanocrystals functionalized with lactoferrin in osteogenic differentiation of mesenchymal stem cells. *J Biomed Mater Res A*, n/a, 2014.
 48. Holmen, S.L., Zylstra, C.R., Mukherjee, A., Sigler, R.E., Faugere, M.-C., Bouxsein, M.L., Deng, L., Clemens, T.L. and Williams, B.O. Essential role of β -catenin in postnatal bone acquisition. *J Biol Chem* **280**, 21162, 2005.

Chapter 7: Expansion and differentiation of hMSCs on nanocomposite scaffolds in a bioreactor with mechanical stimulus

7.1. Introduction

The loss or injury of organs or tissues is one of the most frequent and costly problems in health care system with dramatic effects on life quality. Conventionally, the damaged organ/tissue has been substituted by transplanted organ from another patient. However, the donor shortages and increasing number of patients triggered to the origin of a new field, tissue engineering (TE). In 1993, Langer and Vacanti¹ defined tissue engineering as an interdisciplinary field that applies the principles of engineering and life sciences toward the development of biological substitutes that restore, maintain, or improve tissue function. The typical procedure of a TE approach consists in isolating cells from patient, expanding and seeding the cells on synthetic bioresorbable 3D matrices and then the cell/scaffold construction is implanted on the defect of the human (Figure 1) where the scaffold will degrade to be replaced by the new tissue.

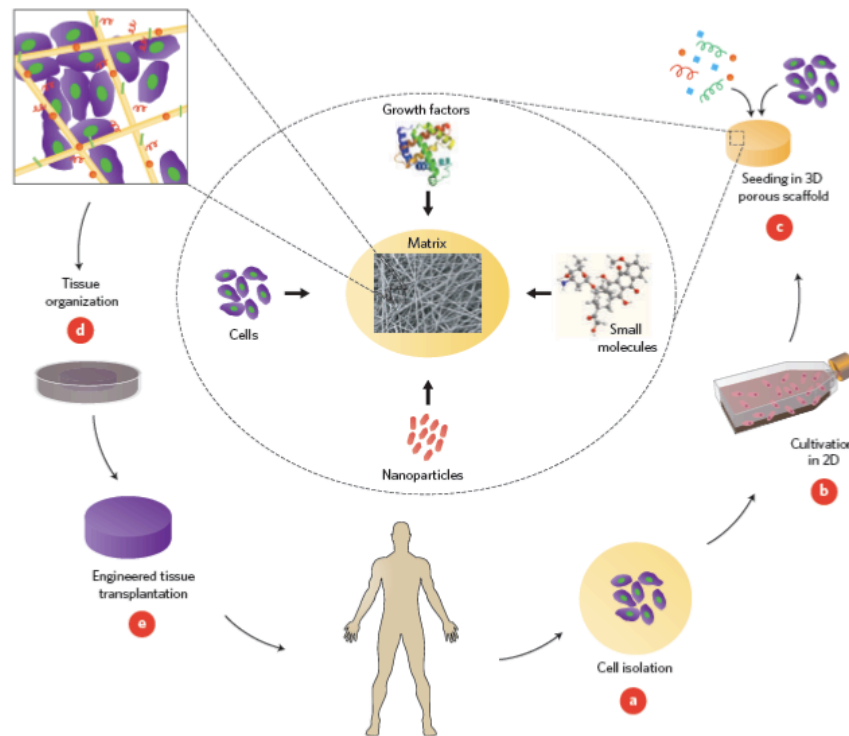


Figure 1. Representative scheme of the tissue-engineering concept. Reprinted from Dvir *et al.*,² Copyright (2011), with permission from Nature Publishing Group: Nature Nanotechnology.

To enhance osteoinductive properties (improve the formation of new tissue), synthetic scaffolds have been incorporated with bone marrow stem cells,^{3,4} drugs and gene delivery,⁵ and different growth factors, such as TGF- β ,⁶ BMP,⁷ and VEGF.^{7,8}

Several studies indicated enhancement of bone formation of synthetic bone substitutes when the material was seeded with cells before implantation.^{9,10} Conventional methods (e.g., static seeding in Petri dishes) have been used for the cell seeding of 3D scaffolds. However, these methodologies yield engineered constructs comprising a thin tissue-like layer at the base of the scaffold, due to gravitational settling of the cells.^{11,12} In addition, static cultures are not optimal due to poor nutrient supply and removal of metabolic waste. In fact, the mass transport occurs only via diffusion, which is not sufficient to support cell survival and proliferation inside the core of large cell/scaffold constructs, resulting in necrosis and poor tissue formation. Furthermore, the cell proliferation and matrix synthesis at the construct periphery over the culture period impede medium diffusion and contribute to the formation of a nutrient gradient that drive cell migration towards the substitute borders.¹³ Static cell culture is far from the *in vivo* conditions, not only for the diffusion inconvenient but also for the lack of mechanical stimulus. Bone cells are sensitive to mechanical stimuli, whose integration and conversion into intracellular signals play an important role in driving bone remodelling throughout lifetime and regeneration during fracture healing.^{14,15}

To overcome the shortcomings of static cell seeding and culture, bioreactors have been proposed for the cultivation of engineered tissues.¹⁶ Among the main advantages, bioreactors can improve initial cell seeding density and homogeneity^{11,17} and at the same time, bioreactor can permit studies of mass transport of oxygen¹⁷⁻¹⁹ and growth factors,^{20,21} hydrodynamic conditions^{22,23} and physical stimuli^{24,25} such as dynamic compression or cyclic stretch. Bioreactors for *in vitro* cell culture can be classified in several categories: rotating wall vessels, spinner flasks, perfusion bioreactors and compression systems.²⁶ The perfusion bioreactors representing the optimal systems to support cell viability, increase construct cellularity and deposition of bone matrix, and guide maturation of functional tissue.

Our previous studies of cell seeding and culture of 3D recombinant peptide scaffolds in static conditions in a well plate showed several drawbacks such as poor cell migration inside of the scaffolds (Chapter 6). Herein, we aimed to demonstrate the suitability of 3D mineralized recombinant peptide scaffolds for the cell seeding and culture of human mesenchymal stem cells (hMSCs) under dynamic conditions in a direct perfusion

bioreactor. Our main goal is to evaluate the osteogenic potential of mineralized scaffolds in presence of magnesium (MgAp/RCP) respect to non-mineralized ones in a real 3D environment. Furthermore, since bioreactor has the possibility to apply a mechanical stimulus during cell culture, and as a first attempt, mechanical stimulus was applied to MgAp/RCP scaffolds loaded with hMSCs, evaluating their influence on hMSC osteogenic differentiation.

7.2. Methods

7.2.1. Flow perfusion bioreactor

The bioreactor system has been developed at Fraunhofer Institute for Interfacial Engineering and Biotechnology (Germany). It is composed of a reservoir flask, the bioreactor cartridge and a peristaltic pump to deliver the cell culture medium from the reservoir flask to the bioreactor cartridge (Figure 2). The scaffolds were sealed with silicone tube with an inner diameter 10 mm and this construct was mounted on the bioreactor cartridge. This set-up ensures the homogeneous conditions inside the scaffold by pressing a silicone tube to the scaffold avoiding the flow of cell culture medium outside of the scaffold, through the walls of the silicone tube.

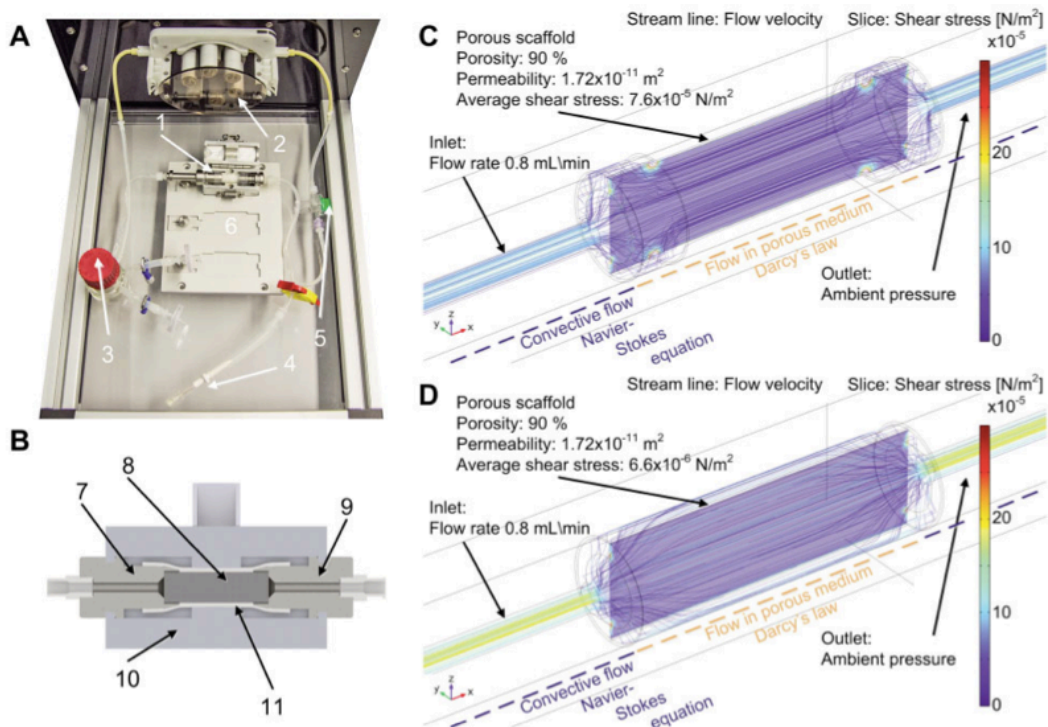


Figure 2. Bioreactor set-up and computational modelling of shear stress due to flow of cell medium through a P[LLA-co-CL] scaffold. (A) Bioreactor set-up composed of: bioreactor cartridge (1), computer-controlled pump (2), a reservoir flask including air

filters (3), a septum for cell seeding (4), an adapter to attach a pressure sensor (5) and a rack system that allows easy handling (6). B) A cross section shows the concept of the bioreactor cartridge. From an inlet (7), cell culture medium is guided through the cylindrical scaffold (8) to an outlet (9). The bioreactor housing (10) pressed a silicone tube (11) to the cylinder jacket surface of the scaffold to ensure homogeneous flow conditions in the scaffold. Computational modelling depicts the fluid mechanical conditions in the bioreactor for sealed (C) and unsealed (D) scaffolds. Reprinted from Kleinhans *et al.*,²⁷ Copyright (2015) with permission of Wiley-VCH Verlag GmbH & Co.

7.2.2. Cell seeding of 3D scaffolds

Human mesenchymal stem cells (hMSCs) extracted from different patient donors (P57 and P58) were kindly supplied by Davide Confalonieri (researcher at University Hospital of Würzburg and member of Bio-inspired project). The hMSCs were expanded in growth medium composed of MSCGM-CD media (Lonza), 2% fetal calf serum (FCS, Lonza), and 1% Pen/Strep at 37 °C in a humidified atmosphere of 5% CO₂. Culture medium was replaced 3 times a week. Cells were detached from culture flasks by trypsinization, centrifuged and resuspended. Cell number and viability were assessed with the trypan-blue dye exclusion test. hMSCs passage 4 were used for the experiments. Before cell seeding, sterilized scaffolds by autoclave (diameter=10 mm and height=10 mm) were pre-incubated overnight with standard cell culture medium (1.5 mL). Then, the scaffolds were seeded under static and dynamic conditions inside bioreactor in order to evaluate the most suitable cell seeding methodology:

- **Static cell seeding (St):** Scaffolds were replaced in a 24-well plate and each one was seeded by carefully dropping 100 µL of cell suspension containing 2.0×10^6 cells onto the upper surface, allowing cell attachment for 90 min at 37 °C with 5% CO₂. Then, hMSCs were incubated in osteogenic medium (1.5 mL) consisting in DMEM High glucose supplemented with 10% (v/v) FCS, 1% (v/v) Pen/Strep, 10 mM β-glicerofosfato, 50 µg/ml L-ascorbic acid and 100 nM dexamethasone under static conditions (37 °C, 5% CO₂) for 1 day.
- **Dynamic cell seeding:** Scaffolds were placed in the custom-fit notch of the bioreactor. 750 µL of cell suspension containing 2.0×10^6 (D2) or 5.0×10^6 (D5) cells were transferred to a 2 mL syringe and was injected air-bubble free through the sterile sampling port manually, in a backward-forward cycles to get homogeneous distribution of the cells through the whole scaffold. Then,

cell/scaffold construction was maintained for 90 min at 37 °C with 5% CO₂ to allow cell attachment before connecting to pump system for dynamic cell culture.

To evaluate the three cell seeding methodologies, after one day of cell culture, cell viability was determined by MTT assay. It allows evaluating cell distribution in the scaffold since the metabolically active cells react with the tetrazolium salt in the MTT reagent producing a formazan dye. Then, formazan crystals can be dissolved with DMSO and measured the absorbance (at 570 nm) that is directly proportional to the number of metabolically active cells (protocol described in Chapter 2).

7.2.3. Dynamic cell culture

For dynamic cell culture, 30 mL of osteogenic cell medium was added to the reservoir flask and the seeded scaffolds were perfused in the bioreactor for 5 min at 1 mL/min each 15 min at 37 °C and 5% CO₂. Dynamic cell culture was carried out initially during one day in order to evaluate best cell seeding methodology and for 15 days (previous cell seeding through D5 methodology) changing cell medium every three days. All the cell-handling procedures were performed in a sterile laminar flow hood.

7.2.4. Mechanical stimulus

For dynamic cell culture with mechanical stimulus, 30 mL of cell culture medium was added to the reservoir flask and the seeded scaffolds (D5 methodology) were perfused in the bioreactor for 5 min at 1 mL/min each 15 min for a period of 7 days at 37 °C and 5% CO₂. After one day of cell culture, mechanical stimulus was applied to cell/scaffold construction with amplitude 2% and frequency 1 Hz during one hour once per day. Culture medium was changed in the middle of the experiment.

7.3. Results

7.3.1. Cell seeding of 3D scaffolds

Before starting dynamic cell culture in bioreactor, two different cell seeding methodologies (static *vs* dynamic) and two cell densities were evaluated. In the static seeding method, the cell suspension (containing 2.0×10^6 cells) was seeded at the top of RCP and MgAp/RCP scaffolds and after one day of cell culture, most of the cells remained at the top of the scaffold, penetrating few microns, as we can observe in scaffold images after MTT assay in Figure 3. The static cell seeding also promoted the

formation of cellular capsule around the edges of the scaffold (arrows Figure 3). On the other hand, scaffolds seeded under dynamic conditions showed a homogeneous cell distribution as indicated the purple colour through the whole scaffolds, for both scaffold compositions (RCP and MgAp/RCP) and both cell suspension concentrations (2 and 5×10^6 cells). RCP and MgAp/RCP scaffolds seeded with 2×10^6 cells showed areas with light colour at the interior of the scaffold whereas scaffolds seeded with 5×10^6 cells were completely in purple colour both inside and outside. The absorbance value indicated higher cell viability for scaffolds seeded under dynamic conditions with 5×10^6 cells respect to 2×10^6 cells ($p < 0.001$). For cell seeding with 2×10^6 cells, scaffolds seeded under static conditions showed higher cell viability than dynamic one ($p < 0.001$). Conversely, for static cell seeding, most cells were outside of the scaffolds.

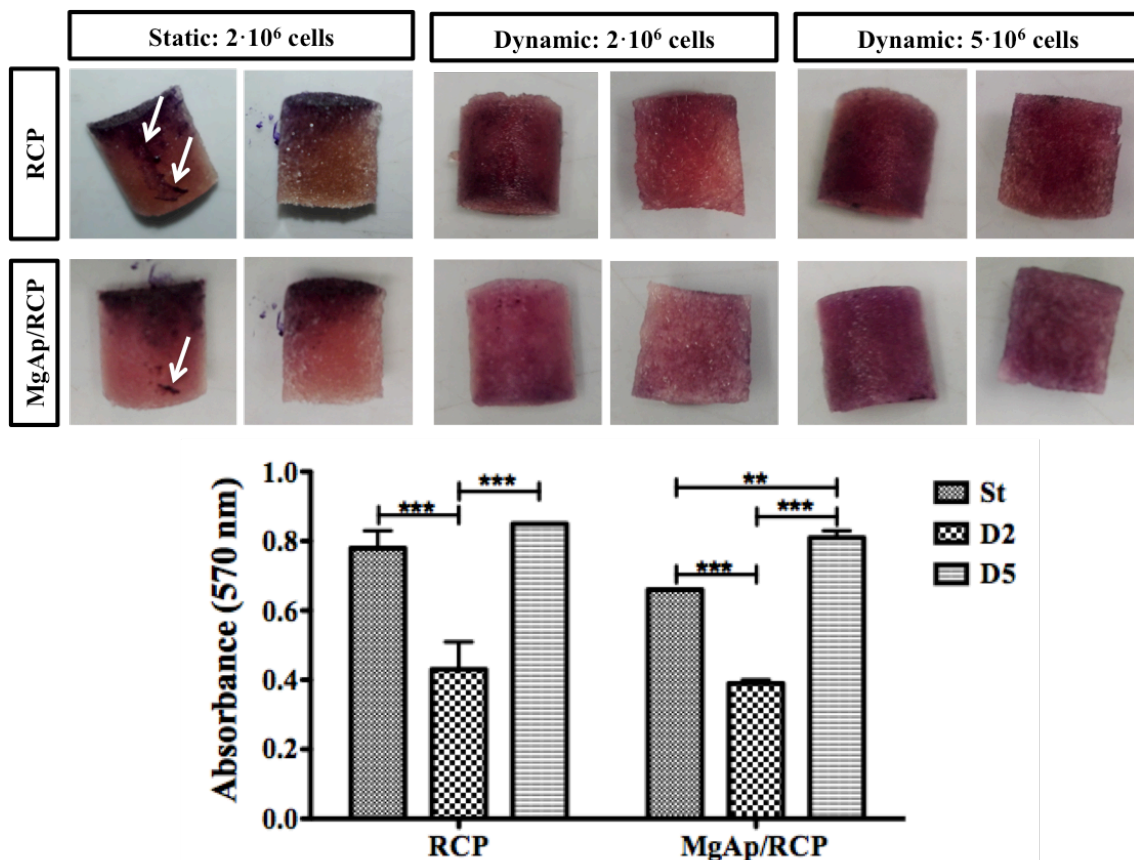


Figure 3. Cell viability evaluated by MTT assay after 1 day of cell culture on RCP and MgAp/RCP scaffolds seeded by three different methodologies: 2×10^6 hMSCs seeded in static conditions (St), 2×10^6 hMSCs seeded in dynamic conditions (D2) and 5×10^6 hMSCs seeded in dynamic conditions (D5). Graph displays absorbance at 570 nm that is proportional to metabolic cell activity. Data are expressed as mean \pm SEM ($n=3$, technical replicates). ** $p < 0.01$ and *** $p < 0.001$.

7.3.2. Dynamic cell culture of hybrid recombinant collagen peptide scaffolds

RCP and MgAp/RCP scaffolds seeded with 5×10^6 hMSCs were cultured under dynamic conditions for 15 days. Then, the experiment was stopped and cell viability as well as osteogenic gene expression was evaluated. The colour of the scaffolds after MTT analysis indicated a higher hMSCs proliferation on MgAp/RCP scaffolds (Figure 4b) compared to RCP scaffolds (Figure 4a). Nevertheless, no statistical difference of absorbance value was found (Figure 4c). The figures 4 d and e show representative images of the inner area of RCP and MgAp/RCP scaffolds, respectively, where cell nuclei appeared stained in blue colour with DAPI. Both scaffolds showed a good cell distribution in the inner areas after 15 days of dynamic cell culture.

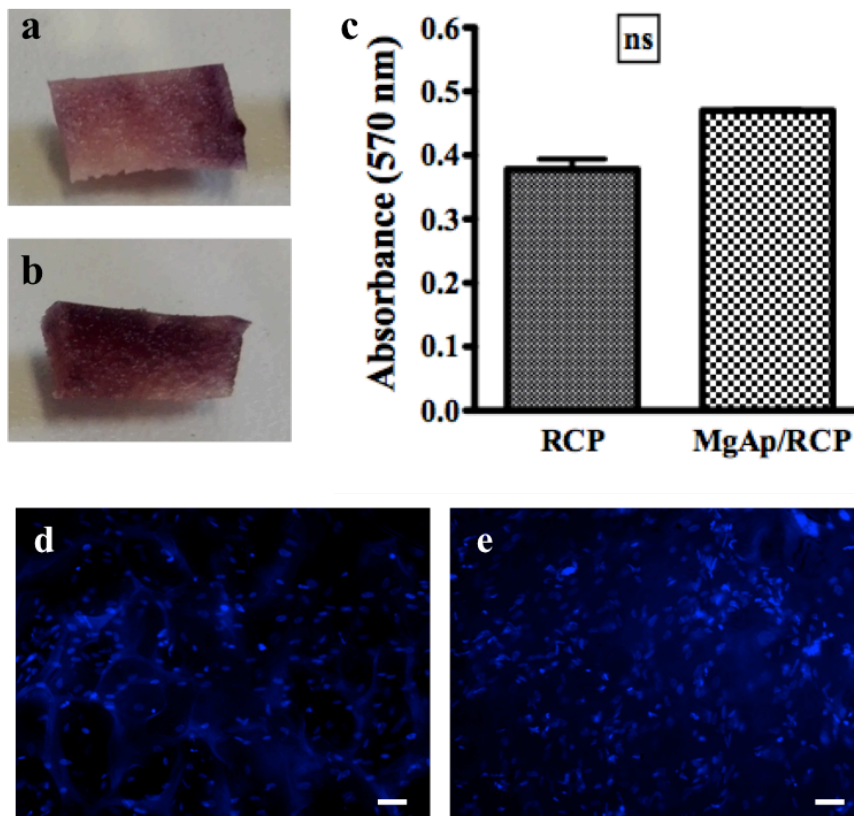


Figure 4. Cell viability evaluated by MTT analysis after 15 days cell culture under dynamic conditions. Images of a piece of RCP (a) and MgAp/RCP (b) scaffolds after 2 hours of addition of MTT reagent. The graph (c) displays the absorbance value at 570 nm after treatment of both cell/scaffold constructions in DMSO. Data are expressed as mean \pm SEM (n=2 cell patient donors). Microscopic images of the inner areas of RCP (d) and MgAp/RCP (e) scaffolds after 15 days of cell culture under dynamic conditions. Blue: Cell nuclei. Scale bar 50 μ m.

After 15 days of cell culture under dynamic conditions, we analysed the expression of osteogenic markers: alkaline phosphatase (ALP), collagen (Col1a1), osterix (OSX), runt-related transcription factor 2 (RUNX2) and bone sialoprotein (BSP) (Figure 5). The results indicated that all the evaluated genes were up regulated for hMSCs grown in MgAp/RCP scaffolds when compared to the hMSCs grown in the control scaffolds (RCP). Col1a1 mRNA level of cells cultured on MgAp/RCP scaffolds was statistically significant respect to RCP ($p < 0.001$).

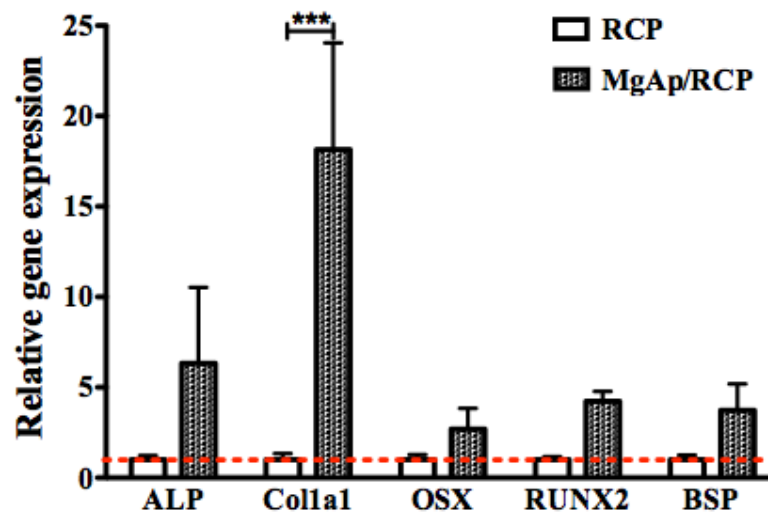


Figure 5. Relative quantification of gene expression of ALP, Col1, OSX, RUNX-2 and BSP respect to housekeeping gene (GAPDH) after 15 days of cell culture under dynamic conditions. Data are expressed as mean \pm SEM (n=2 cell patient donors). *** $p < 0.001$.

7.3.3. Dynamic cell culture of hMSCs in MgAp/RCP with mechanical stimulus

The second aim is to evaluate the role of mechanical stimulus on osteogenic differentiation of hMSCs cultured on MgAp/RCP scaffolds under dynamic conditions. 5.0×10^6 hMSCs (only from one cell patient donor, preliminary study) were cultured under dynamic conditions without (Control) and with mechanical stimulus (Mechanical) up to 7 days.

The influence of mechanical stimulus on matrix production (mineralization) was evaluated by alizarin red staining (Figure 6). However, the main drawback of this technique is that MgAp/RCP scaffolds contain calcium and that their calcium content might be affected after dynamic perfusion of cell medium (also containing calcium) without cells. Therefore, to roughly evaluate the *in vitro* mineralization, MgAp/RCP

scaffolds without cells (NC) were cultured for 7 days under dynamic conditions to quantify the calcium content of the scaffolds (alone, without cells) after this period. The calcium content of cell-loaded scaffolds cultured under dynamic conditions with mechanical stimulus (Mechanical) was compared respect to the calcium of cell-loaded scaffolds cultured in the same conditions without mechanical stimulus (Control). The results indicated a significant increase ($p < 0.01$) of mineralization due to mechanical stimulus (Figure 6). Cell-loaded scaffolds cultured with and without mechanical stimulus exhibited higher calcium content than scaffolds without cells ($p < 0.001$) that could indicate that *in vitro* mineralization took place in both conditions.

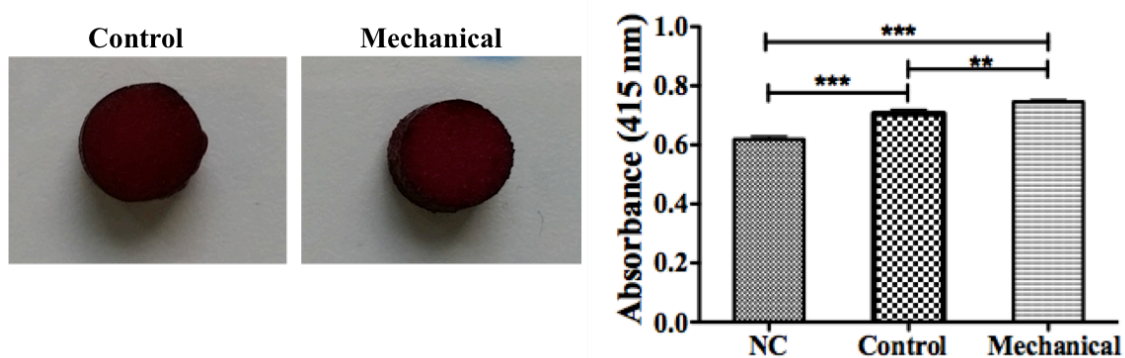


Figure 6. Scaffold mineralization after 7 days of cell culture under dynamic conditions without (Control) and with mechanical stimulus analysed by Alizarin red staining. Graph displays the calcium content measured quantitatively by dissolving alizarin red. NC represents calcium content of MgAp/RCP scaffolds after 7 days under dynamic flux of cell medium but without cells. Data are expressed as mean \pm SEM ($n=3$ technical replicates). ** $p < 0.01$ and *** $p < 0.001$.

To investigate the influence of mechanical stimulus on osteogenic lineage commitment, we evaluated the expression of osteogenic gene markers as well as genes related to angiogenesis by qPCR (Figure 7). The genes under study were: secreted protein acidic and rich in cysteine (SPARC) known as osteonectin, bone gamma-carboxyglutamic acid-containing protein (BGLAP) known as osteocalcin, runt-related transcription factor 2 (RUNX2), alkaline phosphatase (ALP), collagen (Col1), vascular endothelial growth factor (VEGF), transforming growth factor (TGF- β) and bone morphogenetic protein (BMP-2). All the genes were up regulated for scaffolds subjected to mechanical stimulus respect to the control, except from SPARC and BGLAP expression.

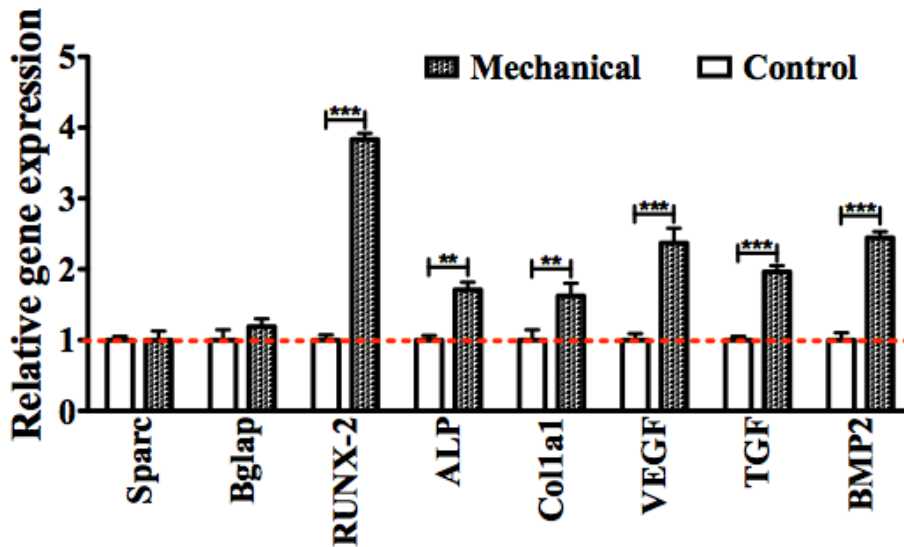


Figure 7. Relative quantification of gene expression respect to housekeeping gene (GAPDH) of hMSCs cultured on MgAp/RCP scaffolds after 7 days of dynamic cell culture without (Control) and with mechanical stimulus (Mechanical). Data are expressed as mean \pm SEM (n=3 technical replicates).

7.4. Discussion

Hybrid recombinant collagen peptide scaffolds are proposed for bone tissue engineering as a matrix to support hMSCs differentiation and the further formation of new bone. However, our previous *in vitro* studies in static conditions (Chapter 6) showed several drawbacks such as poor cell migration to the inner areas of the scaffolds. To overcome these shortcomings, herein we proposed to improve 3D cell culture system by working in a bioreactor of direct perfusion. The bioreactor technology allows the generation of cell-loaded bone substitutes for treatment of critical size bone defects by overcoming limitations of nutrients supply when cells are culture in static conditions in a porous 3D scaffold.²⁸ Three main issues were explored along this chapter: cell seeding, cell culture under dynamic conditions to demonstrate the potential of mineralization of recombinant collagen peptide scaffolds on enhancing hMSCs osteogenic differentiation and the evaluation of the influence of mechanical stimulus on osteogenic commitment of hMSCs cultured on 3D hybrid scaffolds.

The cell seeding of scaffolds is the first step in establishing a 3D culture, and might play a crucial role in determining the progression of tissue formation.²⁹ In fact, seeding cells into 3D scaffolds at high densities has been associated with enhanced tissue formation in 3D constructs, including higher rates of cartilage matrix production,³⁰ increased bone mineralization³¹ and enhanced cardiac tissue structure.³² Moreover, the initial

distribution of cells within the scaffold after seeding has been related to the distribution of tissue subsequently formed within engineered constructs,^{31,33-35} suggesting that uniform cell seeding could establish the basis for uniform tissue generation. Some of the previous works on 3D cell culture under dynamic conditions have carried out the cell seeding in static conditions and later the cell/scaffold construction has been moved to a bioreactor to evaluate the cell response respect to different parameters of dynamic cell culture.^{13,36,37} In fact, static cell seeding onto a 3D scaffold is by far the most commonly used seeding method. However, several studies reported low seeding efficiencies and non-uniform cell distributions within scaffolds.^{31,33,38-40} Other authors have carried out cell seeding and cell culture, both, under dynamic conditions.^{27,41,42} Herein, we carried out cell seeding in static and dynamic conditions. The results indicated a more uniform cell distribution, even in the inner areas of the scaffolds, for cell seeding under dynamic conditions. It fits with previous studies that indicated higher seeding efficiencies and more-uniform cell distributions for 3D-scaffolds seeded by direct perfusion in automated bioreactor when compared with either static seeding or the stirred-flask bioreactor.^{13,39,43} Unlike cell culture in static conditions (Chapter 6), the dynamic conditions provided a real 3D cell culture environment to evaluate the influence of scaffold mineralization in the presence of magnesium (MgAp/RCP scaffolds) in the osteogenic differentiation of hMSCs. After 15 days of cell culture under dynamic conditions, RCP and MgAp/RCP scaffolds did not show significant difference on cell proliferation and distribution. Conversely, hMSCs cultured on MgAp/RCP scaffolds showed up-regulation of several markers of osteogenic differentiation *in vitro*: ALP, which is responsible for the mineralization of the ECM,⁴⁴ Col1 since the mineral nucleation begins at the junction between two collagen fibre bundles, OSX which is an osteoblast-specific transcription factor which activates a repertoire of genes during differentiation of preosteoblasts into mature osteoblasts and osteocytes,⁴⁵ RUNX2 which is often referred to as the master switch of osteogenic differentiation^{46,47} and BSP that binds to Ca²⁺ via free hydroxyl groups and promotes nucleation of mineral.⁴⁸ The results highlighted the greatest potential of MgAp/RCP scaffolds inducing MSCs osteogenic differentiation *in vitro*, both in static (Chapter 6) and dynamic conditions. A preliminary test to evaluate the influence of mechanical stimulus on hMSCs cultured on hybrid-mineralized scaffolds (MgAp/RCP) was carried out up to 7 days of cell culture. The mechanical stimulus promoted the hMSCs osteogenic differentiation (up-regulation of osteogenic markers) and ECM production (collagen and calcium

production) when compared with cell/scaffold construction perfused in the bioreactors in the same conditions but without mechanical stimulus. The mechanical stimulus also promoted the expression of VEGF and TGF- β that play relevant roles in angiogenesis.⁴⁹ Mauney *et al.*⁵⁰ demonstrated that the mechanical stimulation enhanced alkaline phosphatase activity, bone-specific protein transcript levels (alkaline phosphatase and osteopontin) and mineralized matrix production of human bone marrow stromal cells (BMSCs). The first demonstration that strain alone can induce osteogenic differentiation without the addition of osteogenic supplements was reported by Sumanasinghe *et al.*⁵¹ There are increasing evidence suggesting that mechanical forces, which are known to be important modulators of cell physiology, might increase the activity of cells cultured in synthetic substitutes and, thus, possibly improve or accelerate tissue regeneration *in vitro*.⁵²

7.5. Conclusions

In this chapter, static and dynamic cell seeding methodologies were evaluated. Dynamic cell seeding of recombinant collagen peptide scaffolds (RCP and MgAp/RCP) showed uniform cell distribution along the inner areas of tested scaffolds. Furthermore, hMSCs cultured on MgAp/RCP scaffolds under dynamic conditions in the bioreactor of direct perfusion showed up-regulation of osteogenic genes when compared to hMSCs cultured on RCP scaffolds under the same conditions. Hence, the mechanical stimulus on cells seeded on MgAp/RCP scaffold promoted an enhancement of mineralization as well as higher up-regulation of osteogenic genes. To the best of our knowledge, this work represents the first study that evaluate the influence of the biomimetic mineralization of a recombinant collagen peptide scaffold on the hMSCs behaviour in a bioreactor of flow perfusion. Herein, the possibility to enhance osteogenic differentiation thanks to mechanical stimulus was also evaluated.

References

1. Langer, R. and Vacanti, J.P. Tissue engineering. *Science* **260**, 920, 1993.
2. Dvir, T., Timko, B.P., Kohane, D.S. and Langer, R. Nanotechnological strategies for engineering complex tissues. *Nat Nanotechnol* **6**, 13, 2011.
3. Yoon, I.-S., Chung, C.W., Sung, J.-H., Cho, H.-J., Kim, J.S., Shim, W.-S., Shim, C.-K., Chung, S.-J. and Kim, D.-D. Proliferation and chondrogenic differentiation of human adipose-derived mesenchymal stem cells in porous hyaluronic acid scaffold. *J Biosci Bioeng* **112**, 402, 2011.

4. Kon, E., Delcogliano, M., Filardo, G., Fini, M., Giavaresi, G., Francioli, S., Martin, I., Pressato, D., Arcangeli, E., Quarto, R., Sandri, M. and Marcacci, M. Orderly osteochondral regeneration in a sheep model using a novel nano-composite multilayered biomaterial. *J Orth Res* **28**, 116, 2010.
5. Castaño, I.M., Curtin, C.M., Shaw, G., Murphy, J.M., Duffy, G.P. and O'Brien, F.J. A novel collagen-nanohydroxyapatite microRNA-activated scaffold for tissue engineering applications capable of efficient delivery of both miR-mimics and antagomiRs to human mesenchymal stem cells. *J Control Release* **200**, 42, 2015.
6. DeFail, A.J., Chu, C.R., Izzo, N. and Marra, K.G. Controlled release of bioactive TGF- β 1 from microspheres embedded within biodegradable hydrogels. *Biomaterials* **27**, 1579, 2006.
7. Hernández, A., Reyes, R., Sanchez, E., Rodríguez - Évora, M., Delgado, A. and Evora, C. In vivo osteogenic response to different ratios of BMP - 2 and VEGF released from a biodegradable porous system. *J Biomed Mater Res A* **100**, 2382, 2012.
8. Kempen, D.H., Lu, L., Heijink, A., Hefferan, T.E., Creemers, L.B., Maran, A., Yaszemski, M.J. and Dhert, W.J. Effect of local sequential VEGF and BMP-2 delivery on ectopic and orthotopic bone regeneration. *Biomaterials* **30**, 2816, 2009.
9. Hesse, E., Kluge, G., Atfi, A., Correa, D., Haasper, C., Berding, G., Shin, H.-o., Viering, J., Länger, F. and Vogt, P.M. Repair of a segmental long bone defect in human by implantation of a novel multiple disc graft. *Bone* **46**, 1457, 2010.
10. Viateau, V., Guillemain, G., Bousson, V., Oudina, K., Hannouche, D., Sedel, L., Logeart - Avramoglou, D. and Petite, H. Long - bone critical - size defects treated with tissue - engineered grafts: A study on sheep. *J Orth Res* **25**, 741, 2007.
11. Pei, M., Solchaga, L.A., Seidel, J., Zeng, L., Vunjak-Novakovic, G., Caplan, A.I. and Freed, L.E. Bioreactors mediate the effectiveness of tissue engineering scaffolds. *The FASEB Journal* **16**, 1691, 2002.
12. Freed, L., Marquis, J., Langer, R., Vunjak - Novakovic, G. and Emmanuel, J. Composition of cell - polymer cartilage implants. *Biotechnol Bioeng* **43**, 605, 1994.
13. Goldstein, A.S., Juarez, T.M., Helmke, C.D., Gustin, M.C. and Mikos, A.G. Effect of convection on osteoblastic cell growth and function in biodegradable polymer foam scaffolds. *Biomaterials* **22**, 1279, 2001.
14. Huang, C. and Ogawa, R. Mechanotransduction in bone repair and regeneration. *The FASEB Journal* **24**, 3625, 2010.
15. Klein-Nulend, J., Bacabac, R. and Mullender, M. Mechanobiology of bone tissue. *Pathol Biol* **53**, 576, 2005.
16. Freed, L.E., Guilak, F., Guo, X.E., Gray, M.L., Tranquillo, R., Holmes, J.W., Radisic, M., Sefton, M.V., Kaplan, D. and Vunjak-Novakovic, G. Advanced tools for tissue engineering: scaffolds, bioreactors, and signaling. *Tissue Eng* **12**, 3285, 2006.
17. Radisic, M., Euloth, M., Yang, L., Langer, R., Freed, L.E. and Vunjak - Novakovic, G. High - density seeding of myocyte cells for cardiac tissue engineering. *Biotechnol Bioeng* **82**, 403, 2003.

18. Obradovic, B., Carrier, R.L., Vunjak-Novakovic, G. and Freed, L.E. Gas exchange is essential for bioreactor cultivation of tissue engineered cartilage. *Biotechnol Bioeng* **63**, 197, 1999.
19. Radisic, M., Yang, L., Boublik, J., Cohen, R.J., Langer, R., Freed, L.E. and Vunjak-Novakovic, G. Medium perfusion enables engineering of compact and contractile cardiac tissue. *American Journal of Physiology-Heart and Circulatory Physiology* **55**, H507, 2004.
20. Pei, M., Seidel, J., Vunjak-Novakovic, G. and Freed, L. Growth factors for sequential cellular de-and re-differentiation in tissue engineering. *Biochem Biophys Res Commun* **294**, 149, 2002.
21. Gooch, K.J., Blunk, T., Courter, D., Sieminski, A., Bursac, P.M., Vunjak-Novakovic, G. and Freed, L.E. IGF-I and mechanical environment interact to modulate engineered cartilage development. *Biochem Biophys Res Commun* **286**, 909, 2001.
22. Papadaki, M., Bursac, N., Langer, R., Merok, J., Vunjak-Novakovic, G. and Freed, L. Tissue engineering of functional cardiac muscle: molecular, structural, and electrophysiological studies. *American Journal of Physiology-Heart and Circulatory Physiology* **280**, H168, 2001.
23. Vunjak - Novakovic, G., Martin, I., Obradovic, B., Treppo, S., Grodzinsky, A., Langer, R. and Freed, L. Bioreactor cultivation conditions modulate the composition and mechanical properties of tissue - engineered cartilage. *J Orth Res* **17**, 130, 1999.
24. Seidel, J., Pei, M., Gray, M., Langer, R., Freed, L. and Vunjak - Novakovic, G. Long - term culture of tissue engineered cartilage in a perfused chamber with mechanical stimulation. *Biorheology* **41**, 445, 2004.
25. Akhyari, P., Fedak, P.W., Weisel, R.D., Lee, T.-Y.J., Verma, S., Mickle, D.A. and Li, R.-K. Mechanical stretch regimen enhances the formation of bioengineered autologous cardiac muscle grafts. *Circulation* **106**, I, 2002.
26. Sladkova, M. and de Peppo, G.M. Bioreactor systems for human bone tissue engineering. *Processes* **2**, 494, 2014.
27. Kleinhans, C., Mohan, R.R., Vacun, G., Schwarz, T., Haller, B., Sun, Y., Kahlig, A., Kluger, P., Finne - Wistrand, A. and Walles, H. A perfusion bioreactor system efficiently generates cell - loaded bone substitute materials for addressing critical size bone defects. *Biotechnol J* **10**, 1727, 2015.
28. Martin, I., Wendt, D. and Heberer, M. The role of bioreactors in tissue engineering. *Trends Biotechnol* **22**, 80, 2004.
29. Vunjak Novakovic, G., Obradovic, B., Martin, I., Bursac, P.M., Langer, R. and Freed, L.E. Dynamic cell seeding of polymer scaffolds for cartilage tissue engineering. *Biotechnol Prog* **14**, 193, 1998.
30. Freed, L.E., Langer, R., Martin, I., Pellis, N.R. and Vunjak-Novakovic, G. Tissue engineering of cartilage in space. *Proc Natl Acad Sci USA* **94**, 13885, 1997.
31. Holy, C.E., Shoichet, M.S. and Davies, J.E. Engineering three-dimensional bone tissue in vitro using biodegradable scaffolds: investigating initial cell-seeding density and culture period. *J Biomed Mater Res* **51**, 376, 2000.
32. Carrier, R.L., Papadaki, M., Rupnick, M., Schoen, F.J., Bursac, N., Langer, R., Freed, L.E. and Vunjak-Novakovic, G. Cardiac tissue engineering: cell seeding, cultivation parameters, and tissue construct characterization. *Biotechnol Bioeng* **64**, 580, 1999.

33. Kim, B.-S., Putnam, A.J., Kulik, T.J. and Mooney, D.J. Optimizing seeding and culture methods to engineer smooth muscle tissue on biodegradable polymer matrices. 1998.
34. Ishaug-Riley, S.L., Crane-Kruger, G.M., Yaszemski, M.J. and Mikos, A.G. Three-dimensional culture of rat calvarial osteoblasts in porous biodegradable polymers. *Biomaterials* **19**, 1405, 1998.
35. Freed, L., Hollander, A., Martin, I., Barry, J., Langer, R. and Vunjak-Novakovic, G. Chondrogenesis in a cell-polymer-bioreactor system. *Exp Cell Res* **240**, 58, 1998.
36. Liu, L., Guo, Y., Chen, X., Li, R., Li, Z., Wang, L., Wan, Z., Li, J., Hao, Q. and Li, H. Three-dimensional dynamic culture of pre-osteoblasts seeded in HA-CS/Col/nHAP composite scaffolds and treated with α -ZAL. *Acta Biochim Biophys* **44**, 669, 2012.
37. Poh, P.S., Hutmacher, D.W., Holzapfel, B.M., Solanki, A.K., Stevens, M.M. and Woodruff, M.A. In vitro and in vivo bone formation potential of surface calcium phosphate-coated polycaprolactone and polycaprolactone/bioactive glass composite scaffolds. *Acta Biomater* **30**, 319, 2016.
38. Li, Y., Ma, T., Kniss, D.A., Lasky, L.C. and Yang, S.T. Effects of filtration seeding on cell density, spatial distribution, and proliferation in nonwoven fibrous matrices. *Biotechnol Prog* **17**, 935, 2001.
39. Wendt, D., Marsano, A., Jakob, M., Heberer, M. and Martin, I. Oscillating perfusion of cell suspensions through three - dimensional scaffolds enhances cell seeding efficiency and uniformity. *Biotechnol Bioeng* **84**, 205, 2003.
40. Riesle, J. and Van Blitterswijk, C. Static and dynamic fibroblast seeding and cultivation in porous PEO/PBT scaffolds. *J Mater Sci Mater Med* **10**, 773, 1999.
41. Janssen, F.W., Oostra, J., van Oorschot, A. and van Blitterswijk, C.A. A perfusion bioreactor system capable of producing clinically relevant volumes of tissue-engineered bone: in vivo bone formation showing proof of concept. *Biomaterials* **27**, 315, 2006.
42. Egger, D., Krammer, M., Hansmann, J., Walles, H. and Kasper, C. Dynamic cultivation of human stem cells under physiological conditions. presented at the" BMC Proc, Year.
43. Yu, X., Botchwey, E.A., Levine, E.M., Pollack, S.R. and Laurencin, C.T. Bioreactor-based bone tissue engineering: the influence of dynamic flow on osteoblast phenotypic expression and matrix mineralization. *Proc Natl Acad Sci USA* **101**, 11203, 2004.
44. Granéli, C., Thorfve, A., Ruetschi, U., Brisby, H., Thomsen, P., Lindahl, A. and Karlsson, C. Novel markers of osteogenic and adipogenic differentiation of human bone marrow stromal cells identified using a quantitative proteomics approach. *Stem Cell Res* **12**, 153, 2014.
45. Sinha, K.M. and Zhou, X. Genetic and molecular control of osterix in skeletal formation. *J Cell Biochem* **114**, 975, 2013.
46. Ducy, P., Schinke, T. and Karsenty, G. The osteoblast: a sophisticated fibroblast under central surveillance. *Science* **289**, 1501, 2000.
47. Deng, Z.-L., Sharff, K.A., Tang, N., Song, W.-X., Luo, J., Luo, X., Chen, J., Bennett, E., Reid, R. and Manning, D. Regulation of osteogenic differentiation during skeletal development. *Front Biosci* **13**, 2001, 2008.
48. Roach, H. Why does bone matrix contain non-collagenous proteins? The possible roles of osteocalcin, osteonectin, osteopontin and bone sialoprotein in bone mineralisation and resorption. *Cell Biol Int* **18**, 617, 1994.

49. Ferrari, G., Cook, B.D., Terushkin, V., Pintucci, G. and Mignatti, P. Transforming growth factor - beta 1 (TGF - β 1) induces angiogenesis through vascular endothelial growth factor (VEGF) - mediated apoptosis. *J Cell Physiol* **219**, 449, 2009.
50. Mauney, J., Sjostorm, S., Blumberg, J., Horan, R., O'leary, J., Vunjak-Novakovic, G., Volloch, V. and Kaplan, D. Mechanical stimulation promotes osteogenic differentiation of human bone marrow stromal cells on 3-D partially demineralized bone scaffolds in vitro. *Calcif Tissue Int* **74**, 458, 2004.
51. Sumanasinghe, R.D., Bernacki, S.H. and Lobo, E.G. Osteogenic differentiation of human mesenchymal stem cells in collagen matrices: effect of uniaxial cyclic tensile strain on bone morphogenetic protein (BMP-2) mRNA expression. *Tissue Eng* **12**, 3459, 2006.
52. Butler, D.L., Goldstein, S.A. and Guilak, F. Functional tissue engineering: the role of biomechanics. *Ann Arbor* **1001**, 77, 2000.

Chapter 8: Concluding remarks

The need of synthetic bone grafts that recreate from macro to nanoscale level the biochemical and biophysical cues of bone extracellular matrix (ECM) has been a major driving force for the development of new generation of biomaterials. In this PhD thesis, new synthetic bone substitutes have been synthesized *via* biomimetic mineralization of a recombinant collagen type I derived peptide (RCP) enriched in tri-amino acid sequence arginine-glycine-aspartate (RGD) and a further freeze-drying. This approach synergistically combines the biofunctionality provided by cell binding sites (RGD sequences) incorporated in RCP sequence with the bioactivity conferred by incorporation of biomimetic mineral phase imitating bone-apatite feature (e.g., composition and crystallinity).

Biomimetic protocol previously applied for mineralization of natural collagen has been successfully adapted for RCP mineralization. Magnesium was introduced during mineralization to closer mimic bone apatite ionic composition. The first step was the investigation of the role of RCP and Mg on mineralization mechanism and final physico-chemical feature of synthesized apatites (Ap). Poor crystalline Ap nanocrystals were obtained in all conditions, together with a certain extent of amorphous calcium phosphate (ACP). The thorough characterization of powdered samples indicated the simultaneous effect of the RCP and Mg on stabilizing ACP as well as hindering crystal growth along *c*-axis.

The next step was to develop prototype 3D hybrid scaffolds with increasing mineral content in order to determine the maximum amount of mineral phase that can be integrated homogeneously into the organic matrix through the biomimetic RCP mineralization. Since RCP does not self-assemble into large microfibers and has lower density of charged amino acids groups than natural collagen, lower mineral integration than natural bone might be expected. In fact, powdered samples or brittle and heterogeneous scaffolds were obtained for higher mineral contents (50-70 wt.%). On the other hand, prototype scaffolds with homogeneous composition were synthesized for 60 wt.% of organic phase and 40 wt.% of mineral phase. For this composition, mineralized matrices were developed in the presence and in the absence of magnesium. The presence of Mg during RCP mineralization provided hybrid matrices with homogeneous mineral distribution at nanoscopic level and mean surface roughness similar to that found in bone.

Since RCP is water soluble, two crosslinking techniques (genipin and dehydrothermal crosslinking, DHT) were investigated to ensure scaffold stability under physiological condition. The chemical crosslinking with genipin was set-up by immersion of the RCP scaffolds in genipin in aqueous-ethanol solution and the genipin concentration was selected considering the crosslinking degree and the water uptake capacity of RCP scaffolds. Then, the two crosslinking methodologies were applied to the three scaffold compositions under study: non-mineralized (RCP) and mineralized in the absence (Ap/RCP) and in the presence of Mg (MgAp/RCP). Crosslinked scaffolds either by genipin or DHT showed a good stability under physiological conditions up to 28 days. The results indicated that the presence of the mineral phase might hinder the crosslinking reaction (lower crosslinking extent for mineralized scaffolds). While the highest extent of crosslinked was achieved for scaffolds crosslinked with genipin (independently of the scaffold composition), the scaffolds crosslinked by DHT were endowed with a higher enzymatic resistance and therefore, they were selected for the further *in vitro* tests.

The next goal was to tailor and design 3D isotropic porous scaffold by freeze-drying through the investigation of several freezing parameters such as solid content, mould and freezing temperature. Isotropic porous structures with pore size suitable for cell proliferation were obtained by freezing mineralized slurry in a well plate at -20 °C. The three scaffold compositions (RCP, Ap/RCP and MgAp/RCP) showed similar porous structure with mean pore size 250 µm, porosity close to 90% and great permeability. Then, mouse mesenchymal stem cells (MSCs) were cultured on the 3D isotropic scaffolds in static conditions to investigate the cytocompatibility and osteogenic potential of designed scaffolds. Mineralized scaffolds showed a better cell migration in the inner areas of the scaffold compared to non-mineralized scaffolds as well as displayed excellent potential for improving the expression of osteogenic markers of MSCs. Magnesium incorporation during mineralization protocol (MgAp/RCP) actually heightened the cell migration and osteogenic potential of designed scaffolds.

Finally, RCP and MgAp/RCP scaffolds were tested *in vitro* under dynamic conditions in a bioreactor of direct perfusion (developed at Fraunhofer Institute) in order to ensure a real 3D culture state. Dynamic cell seeding of RCP and MgAp/RCP scaffolds showed uniform cell distribution along the inner areas of the tested scaffolds after one day of cell culture. Human mesenchymal stem cells (hMSCs) cultured on MgAp/RCP scaffolds under dynamic conditions up to 15 days showed up-regulation of osteogenic

markers when compared to hMSCs cultured on RCP scaffolds in the same conditions. Furthermore, a preliminary test consisting in applying mechanical stimulus to hMSCs seeded on MgAp/RCP scaffolds indicated that mechanical stimulus might promote an enhancement of mineralization as well as higher up-regulation of osteogenic genes.

The results obtained and reported herein indicate that biomimetic mineralization of recombinant collagen peptide in the presence of magnesium is a promising approach for the development of high quality bone grafts with smart interfaces that promote cell-material interaction and osteogenic differentiation of mesenchymal stem cells.

Work in progress based on this thesis

Ramírez-Rodríguez G.B., Montesi M., Panseri S., Sprio S., Tampieri A., Sandri S. *Biomaterialized recombinant collagen-based scaffold mimicking native bone enhances mesenchymal stem cell interaction and differentiation*. Tissue Engineering Under review

Ramírez-Rodríguez G.B., Ramani Mohan R., Sprio S., Tampieri A., Sandri S., Walles H., and Hansmann J. *Expansion and differentiation of hMSCs on hybrid recombinant peptide scaffolds in a bioreactor with mechanical stimulus*. To be submitted in 2017

Peer-reviewed publication based on this thesis

Ramírez-Rodríguez GB, Delgado-López JM, Iafisco M, Montesi M, Sandri M, Sprio S, et al. *Biomimetic mineralization of recombinant collagen type I derived protein to obtain hybrid matrices for bone regeneration*. J Struct Biol. 2016. 1047-8477

Conference presentation based on this thesis

Ramírez-Rodríguez G.B., Montesi M., Panseri S., Sandri M., Sprio S. and Tampieri A. *Magnesium incorporation into 3D mineralized recombinant collagen scaffolds enhances osteogenic differentiation in vitro*. Materils.it 2016, Catania (Italy). **Oral communication**

Ramírez-Rodríguez G.B., Delgado-Lopez J.M., Montesi M., Panseri S., Sandri M., Sprio S. and Tampieri A. *Biomimetic mineralization of synthetic collagen-like peptide: a bottom-up approach to design advanced nanocomposite scaffolds for tissue engineering*. 10th World Biomaterial Congress, 2016, Montreal (Canada). **Oral communication and travel award**. Frontiers; doi:10.3389/conf.FBIOE.2016.01.02747

Ramírez-Rodríguez G.B., Delgado-Lopez J.M., Montesi M., Panseri S., Sandri M., Sprio S. and Tampieri A. *Nanoscale design of bone scaffolds through biomaterialization process modulating cell behavior*. 4th Termis World Congress, 2015, Boston (USA) Poster communication. Tissue Engineering Part A. September 2015, 21(S1): S-1-S-413

Ramírez-Rodríguez G.B., Delgado-Lopez J.M., Iafisco M., Sandri M., Sprio S. and Tampieri A. *Biomaterialization of apatite in the presence of collagen-like peptide as a versatile route for obtaining bone-like scaffolds*. Biomin XIII, 2015, Granada (Spain). **Oral Communication**

Other peer-reviewed publication

Campodoni E., Heggset B.E., Elsbahy R.S.M., Ramírez-Rodríguez G.B., et al. *Polymeric nano-composite reinforced by cellulose nanofibrils to create 3D scaffolds for tissue regeneration*. To be submitted

Miragoli M., Ceriotti P., Iafisco M., Vacchiano M., Salvarani N., Alogna A., Carullo P., Ramirez-Rodríguez G.B., *et al.* *Inhalation of peptide-loaded nanoparticles improves heart failure*. Submitted in Nature Nanotechnology.

Iafisco M., Ramirez Rodríguez G.B., Degli Esposti L., Remondini M., Gomez Morales J., Tampieri A. and Delgado López J.M. *Citrate stabilized amorphous calcium phosphate doped with fluoride ions: a promising material for enamel remineralization*. To be submitted.

Iafisco M, Di Mauro V, Salvarani N, Ramírez-Rodríguez GB, Patricio T, Miragoli M, et al. Bio-inspired negatively-charged calcium phosphate nanocarriers for cardiac delivery of therapeutic molecules. *Nanomedicine*. 2016; 11:891-906

Iafisco M, Ramírez-Rodríguez GB, Sakhno Y, Tampieri A, Martra G, Gómez-Morales J, et al. The growth mechanism of apatite nanocrystals assisted by citrate: relevance to bone biomineralization. *CrystEngComm*. 2015;17:507-511.

Ramírez-Rodríguez G, Iafisco M, Tampieri A, Gómez-Morales J, Delgado-López J. pH-responsive collagen fibrillogenesis in confined droplets induced by vapour diffusion. *J Mater Sci Mater Med*. 2014:1-8.